Dissertation
submitted to the
Combined Faculties for the Natural Sciences and for Mathematics
of the Ruperto-Carola University of Heidelberg, Germany
for the degree of
Doctor of Natural Sciences

presented by
Dipl. Physicist Sanja Damjanović
Belgrade, Yugoslavia

Oral examination: 17 July, 2002

# Electron-Pair Production in Pb-Au Collisions at 40 AGeV

Referees: Prof. Dr. Hans J. Specht
Prof. Dr. Dirk Schwalm

**Produktion von Elektron-Positron Paaren in Pb-Au Kollisionen bei 40 AGeV**

Die vorliegende Arbeit enthaelt die ersten experimentellen Resultate zur Elektronenpaar-Produktion aus dem CERES/NA45 Experiment am CERN SPS seit der zusaetzlichen Installation einer TPC. Die Daten stammen aus einer Strahlzeit im Jahr 1999 mit einem Pb-Strahl von 40 AGeV. Aus insgesamt 8 Millionen Ereignissen mit einer Zentralitaets-Selektion von 30% wurden $e^+e^-$ Paare mit folgender Statistik rekonstruiert: 249±28 im Massenbereich ≤0.2 GeV/c$^2$ mit einem S/B-Verhaeltnis von 1/1, und 185±48 im Massenbereich > 0.2 GeV/c$^2$ mit einem S/B-Verhaeltnis von 1/6. Die Ausbeute im Bereich niedriger Massen stimmt mit der Erwartung aus hadronischen Zerfaellen ueberein. Die Ausbeute bei hoeheren Massen liegt um einen Faktor 5.1 ± 1.3(stat) ± 1.0(syst) ueber dieser Erwartung, erheblich mehr als die Werte um 2.5-3, die zuvor bei der hoeheren Strahlenergie von 160 AGeV beobachtet wurden.

Theoretisch wird der Ueberschuss von Elektronenpaaren als direkte Strahlung aus dem Feuerball interpretiert, die im wesentlichen durch die Annihilation von Pionenpaaren mit einem modifizierten $\rho$-Propagator entsteht. Nach gegenwaertigem Verstaendnis ist fuer diese Modifikation eher die hohe Baryonendichte als die hohe Temperatur des Feuerballs verantwortlich. Das hier berichtete Resultat einer hoeheren (relativen) Ausbeute bei der niedrigeren Strahlenergie (bei der die Baryonendichte hoeher ist) untermauert dies. Etwas verallgemeinert koennen die Resultate als weiterer Hinweis auf die (partielle) Wiederherstellung der chiralen Symmmetrie angesehen werden.

**Electron-Pair production in Pb-Au Collisions at 40 AGeV**

This thesis contains the first experimental results on electron-pair production from the CERES/NA45 experiment at the CERN SPS after the upgrade with a Time Projection Chamber (TPC). The data were taken in late 1999 with a Pb-beam on a Au-target at a beam energy of 40 AGeV. Out of about 8 Million events with a 30% centrality selection, 249±28 $e^+e^-$ pairs for masses ≤0.2 GeV/c$^2$ with a S/B ratio of 1/1, and 185±48 $e^+e^-$ pairs for masses >0.2 GeV/c$^2$ with a S/B ratio of 1/6 were reconstructed. The low-mass sample agrees with the expectation from hadronic decays. The high-mass sample shows an excess of a factor of 5.1±1.3(stat)±1.0(syst) above that expectation, considerably more than the values around 2.5-3.5 observed before at the higher beam energy of 160 AGeV. The excess yield is dominantly associated with pair transverse momenta <0.5 GeV/c, consistent with the findings at 160 AGeV.

The theoretical relevance of the results is discussed in some detail. The dilepton excess is basically interpreted as direct radiation from the fireball, dominated by pion annihilation with a modified $\rho$-propagator. Theoretically, the modifications are driven by high baryon density more than by high temperature. The experimental results on a larger enhancement factor at a lower beam energy, associated itself with a larger baryon density, confirm this conjecture. Quite generally, the results may signal (partial) chiral symmetry restoration.

Recent major discoveries in fundamental physics:

$J/\psi$ observed in $e^+e^-$

$Y$ observed in $\mu^+\mu^-$

$\tau$ observed in $e\mu^-$+missing energy

$Z_0$ observed in $e^+e^-$

If you want to make a major discovery

build a dilepton detector

Sam Ting

# Contents

# List of Figures

# List of Tables

# Chapter 1

# Introduction

## 1.1 General Remarks

The critical behaviour of strongly interacting matter belongs to the central topics of present-day QCD research in the nonperturbative regime. The appropriate tool to study this field in the laboratory is the use of high-energy nucleus-nucleus collisions. A number of major experiments have been built and operated at the CERN SPS and other machines, devoted to this program. The CERES/NA45 electron-pair spectrometer, the "home experiment" of this doctoral thesis, is one of them. It was built up in the years 1989-1991 and had its first successful production run in 1992 with a 200 AGeV S-beam, followed by a comparison run with 450 GeV/c protons in 1993 and two more production runs with 160 AGeV Pb-beams in 1995 and 1996. The central result, common to all nucleus-nucleus collisions investigated so far is a strong excess of lepton pairs above the level expected for the known electromagnetic decays of the hadrons produced in the interaction. This excess has been interpreted as evidence for chiral symmetry restoration and has therefore met broad interest, triggering an enormous amount of theoretical activity.

The success of a number of theoretical approaches in quantitatively describing the dilepton excess at the full SPS energy of 160 AGeV called for a systematic variation of the essential variables, temperature and baryon density, to confirm the correctness of the interpretation. This has been the driving motivation for this thesis. It focusses on the first experimental results obtained for Pb-Au collisions at the lower beam energy of 40 AGeV, based on data taken during the running period 1999. The results are also the first on electron-pair production after completing the upgrade of CERES with a Time Projection Chamber (TPC) and the installation of a new magnet during 1998/99. Much pioneering work in the analysis has therefore been required to cope with the major changes in the set-up compared to the preceding 1995/96 data analysis.

The thesis is structured as follows. In the introductory chapter 1, an overview is given on the motivation for measuring electron pairs, covering deconfinement and chirality, the virtues of electromagnetic probes, previous results from CERES, a theoretical description of previous CERES results and a more detailed motivation for this thesis. Chapter 2 is devoted to a description of the hardware, including the general CERES set-up and details on the target region, the Si drift chambers, the Ring-Image

Cherenkov detectors, the new TPC and the trigger- and data acquisition system. Chapter 3 contains the details of the data analysis, subdivided into sections on general strategy and data production, on charged particle multiplicity determination in the Si detectors, on electron track reconstruction including all electron identification steps, on pairing of single tracks and, finally, on the absolutely decisive minimization of the combinatorial background from unrecognized low-mass conversion and Dalitz pairs. The Monte Carlo simulations of the experiment, mostly done in a mode of overlaying electron pairs of known characteristics onto real data events, follow in chapter 4. Beyond the simulations of the individual detectors, they concentrate on the overall pair reconstruction efficiency to allow for an absolute normalization of the data. Chapter 5 presents the basic results together with a thorough discussion of the systematical errors. Since new physics can only be derived from the data after a firm assessment of the contributions from known physics, chapter 6 gives an overview and a quantitative description of all hadronic decay sources, subject to the same treatment and the same cuts as applied to the data. Chapter 7 contains the final results. In a first part, they are presented in a comparison to the hadronic decays to bear out the anomalies and new features. In a second part, a rather extensive overview on the different theoretical approaches is given, comparing then the new results from this thesis to the respective pre-(or post)dictions. Chapter 8 finishes with some very general remarks on the comparison between data and theory and on what can be concluded from this thesis.

## 1.2 Theoretical Motivation

### 1.2.1 Deconfinement and Chirality

Quantum Chromodynamics (QCD) is the theory of quarks and gluons, analogous to QED which is the theory of electrons and photons. Both are renormalizabile quantum field theories, where the vacuum is a medium which can screen charge, and where the coupling "constant" is not a constant but depends on the scale. However, a decisive difference arises from the fact that QCD is a non-Abelian theory [1]. This leads to the experimental fact that in the world around us, quarks and gluons occur only in colorless packages: protons, neutrons, pions, kaons,... These hadrons are the quasiparticles of the QCD vacuum. They make up everything from nuclei to neutron stars. More than 20 years ago, the suggestion was made to look at high density or high temperature and to investigate whether other phases exist whose quasiparticles look more like the quarks and gluons of the QCD Lagrangian $\mathcal{L}_{\mathcal{QCD}}$. Indeed, finite temperature lattice QCD predicts that strongly interacting matter will, at sufficiently high energy densities, undergo a phase transition from a state of hadronic constituents to quark matter, a plasma of deconfined quarks and gluons [2]. It is believed that chiral symmetry restoration, associated with the vanishing of the chiral condensate $\langle\overline{q}q\rangle$, takes place at about the same temperature $T_c$. Great interest therefore exists to clarify the role of confinement and chiral symmetry breaking of the QCD phase transition, to confirm the existence of quark matter and to explore its properties.

High energy nucleus-nucleus collisions have been used since about 15 years at the

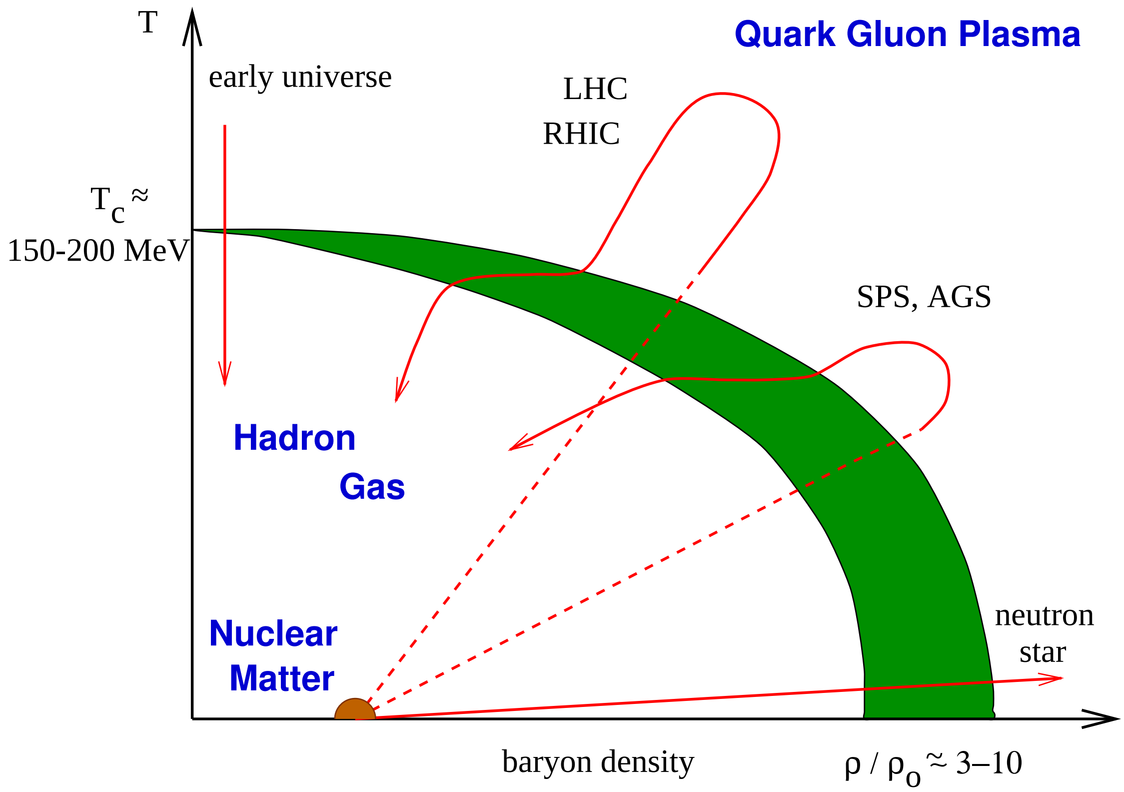


Figure 1.1: *The phase diagram of strongly interacting matter with the border line in the T-$\rho$ plane separating hadronic matter from quark matter. The lines show the dynamical trajectories followed in supernovae explosions (along the horizontal axis), in the Big Bang evolution (along the vertical axis), and in heavy ion collisions (in the whole T-$\rho$ plane).*

BNL AGS and the CERN SPS to experimentally investigate quark matter formation in the laboratory. The experimental conditions can be varied through the collision energy, the nuclear mass and the impact parameter. However, any signature for the QGP is folded with the time evolution of the fireball created in such collisions. Furthermore, this evolution continues after the phase transition, and any information is thus mixed with signals from the hadronic phase. It is an extremely challenging task to obtain a quantitative understanding of the QCD equation of state, to determine critical parameters such as the critical temperature and critical energy density, and to describe the modification of basic hadron properties (masses, decay widths) with temperature and density.

Theoretically, everything is controlled by global symmetries of the QCD Lagrangian $\mathcal{L}_{\mathcal{QCD}}$. However, global symmetry only exists in the limit of either infinite or vanishing quark masses. Starting from a theory which involves only gluons and glueball states without dynamical quarks, mesons and baryons, the confining property of QCD manifests itself in the large distance behaviour of the heavy quark potential. At zero temperature, the potential rises linearly at large distances

$$V_{\bar{q}q} \sim \sigma r \tag{1.1}$$

($\sigma$ is the string tension) and forces quarks and gluons to be confined to hadronic bags. On the other hand, at high temperature where the system is a weakly interacting plasma of gluons, the potential reflects Debye-screening of the color charges

$$V_{\overline{q}q} \sim \frac{g^2(T)}{r} e^{-m_D r} \tag{1.2}$$

($m_D \sim gT$ is the Debye mass), and confinement does not any longer exist [3]. There should be some point $T_d$ (a critical temperature) where the large $r$ asymptotics of the potential changes and a phase transition from the confinement phase to the Debye screening phase occurs. The correlator of two Polyakov loops plays the role of the order parameter for this deconfinement phase transition. In the limit of $r \to \infty$, the correlator $C_T = \langle L(x)L^*(0)\rangle_T$ changes from 0 (confined phase) in the low temperature region to some constant value (deconfined phase) at large temperature. L(x) is the Polyakov loop, defined as the trace of the Wilson loop [4]

$$L(x) = \frac{1}{N_c} Tr(exp(ig\beta A_0^a(\vec{x})t^a)) \tag{1.3}$$

If the theory involves, besides gluons, also quarks with finite mass, a phase transition from a confined to a deconfined phase can still occur. In addition, another phase transition can now occur, associated with the restoration of chiral symmetry which is spontaneously broken at T=0. Chiral symmetry breaking leads to a non-vanishing $\langle\overline{q}q\rangle$ condensate in the vacuum. The critical temperature $T_\chi$ is here the temperature above which chiral symmetry is restored and the fermion condensate $\langle\overline{q}q\rangle_T$ is zero (symmetric phase), while below $T_\chi$ $\langle\overline{q}q\rangle_T$ has a nonzero value (symmetry-broken phase) of about $\langle\overline{q}q\rangle_T \approx -(230MeV)^3$ or $\langle\overline{q}q\rangle_T \approx -1.6fm^{-3}$. Although the two phase transitions at $T_d$ and at $T_\chi$ could be different, present day lattice results [5] suggest that there is only one transition at a critical temperature $T_c$=$T_d$=$T_\chi$. It is highly non-trivial and still unsolved to determine the nature of the transition from a low-temperature weakly interacting pion gas to a high-temperature weakly interacting quark-gluon plasma, i.e. to find out whether a true phase transition of first or second order occurs or just a sharp crossover in the temperature range where the free energy density drastically increases.

In summary, the order parameter for deconfinement in the limit of infinite quark masses is the correlator of Polyakov loops $C_T$ related to the static potential between heavy colored sources. In the limit of vanishing quark masses, the proper order parameter is the quark condensate $\langle\overline{q}q\rangle_T$, and the phase transition is associated with the restoration of chiral symmetry. Instead of looking at the order parameters, one can also use the corresponding susceptibilities, the Polyakov loop susceptibility ($\chi_L$) and the chiral susceptibility ($\chi_m$) defined as:

$$\chi_L = N_\sigma^3 \left(\langle L^2\rangle - \langle L\rangle^2\right), \tag{1.4}$$

$$\chi_m = \frac{\partial}{\partial m_q}\langle\overline{q}q\rangle \tag{1.5}$$

The behaviour of these variables is shown in Fig 1.2 for $n_f$=2. Calculations have been performed for a wide range of quark masses and a varying number of flavours,

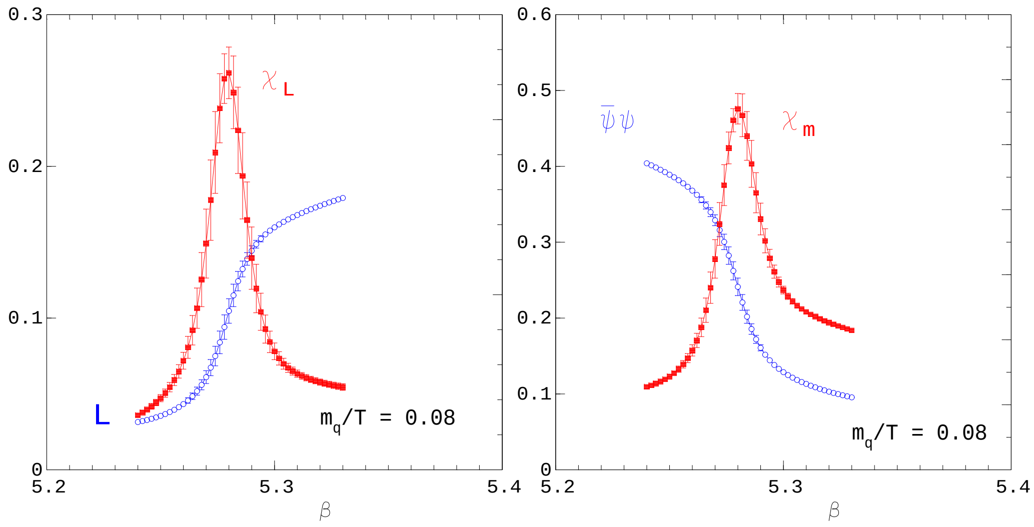


Figure 1.2: *Temperature dependence of the Polyakov loop and associated susceptibility (left side) and of the chiral condensate and associated susceptibility (right side). Both results are obtained in two-flavour QCD [5].*

confirming that the location of the maxima in both susceptibilities is strongly correlated [5]. Both susceptibilities show a very sharp peak at the same location, connected with the most rapid change of $\langle L \rangle$ and $\langle \overline{q}q \rangle$ at that location. Only the height of the maxima is found to strongly depend on the quark masses, but the position of the maxima remains stable. The two phenomena deconfinement and chiral symmetry restoration thus coincide in finite temperature QCD at the same transition temperature.

The basic thermodynamic characteristic of a finite temperature system is its free energy (equilibrium thermodynamics). All thermodynamic observables like pressure (p), energy density ($\epsilon$), entropy density (s) can be determined from the free energy which is defined to lowest order as

$$F_0 = -T ln Z = -T \cdot ln[\prod_{\vec{p}}(\sum_{n=0}^{\infty} e^{-\beta n E_p})^{(N_f^2-1)}] \tag{1.6}$$

where $N_f^2 - 1$ is the number of degrees of freedom of the pseudo-Goldstone fields [6]. The deconfinement phase transition manifests itself in a drastic change of the degrees of freedom, from those of the three light pions in the confined hadronic phase to the much larger number of the liberated quarks and gluons in the QGP phase. The thermodynamic observables like pressure, energy density, etc. which are proportional to the number of degrees of freedom directly reflect the phase transition by a drastic increase when approaching the critical point.

The order parameter of spontaneously broken chiral symmetry, the quark condensate, decreases with increasing temperature. The temperature-dependent condensate $\Sigma(T)$ is defined as the logarithmic derivative of the free energy with respect to the quark mass:

$$\Sigma(T) = \frac{1}{N_f}\frac{1}{V}\frac{\partial F(T)}{\partial m} \tag{1.7}$$

$$\Sigma(T) = \Sigma(0)[1 - \frac{N_f^2 - 1}{12N_f}\frac{T^2}{f_\pi^2} - O(T^4/f_\pi^4)] \tag{1.8}$$

($f_\pi$=93 MeV is the pion decay constant). The expected chiral behaviour can be derived from the singular part of the free energy density.

Similar phenomena are known in condensed matter physics where at finite temperature, spontaneous magnetization of a ferromagnet starts to fluctuate and its average value decreases with increasing temperature. The fluctuations are described by massless magnons which appear due to spontaneous breaking of rotational symmetry in a ferromagnet, analogous to the Goldstone bosons (pions etc.) which appear due to spontaneous breaking of chiral symmetry in QCD. Spontaneously broken chiral symmetry is restored under heating; likewise, spontaneously broken rotational symmetry in a ferromagnet is restored above the Curie point.

The changes of the chiral condensate below $T_c$ and chiral symmetry restoration at $T_c$ will have a strong influence on the light hadron spectrum. For the light mesons spontaneous chiral symmetry breaking manifests itself in the following way (Fig. 1.3):

- the appearance of $n_f^2 - 1$ nearly massless Goldstone bosons (pions,kaons,eta) carrying the quantum numbers of the generators of the broken $SU_A(n_f)$ symmetry (Goldstone theorem).

- the appearance of a gap $\Delta \sim m_\rho \sim$ 1GeV in the low-energy hadron spectrum where almost all hadron states have masses $> \Delta$, while the octet of pseudoscalar mesons ($\pi$, $K$ and $\eta$) is located inside the gap [7].

- the absence of parity doublets, i.e. the splitting of scalar and pseudoscalar as well as of vector and axial vector mesons.

- a non vanishing axial current matrix element between the vacuum and the Goldstone bosons: $\langle 0|j^\mu_{A,a}|\pi_b(p)\rangle = ip^\mu\delta_{ab}f_\pi e^{-ipx}$, where $a = 1...3$, $\pi_a$ is the pion field.

If chiral symmetry would not be broken, degenerate hadronic isospin multiplets of opposite parity would exist. Instead, comparing the scalar meson octet with the pseudoscalar octet or the axial vector octet with the vector octet, there are indeed mass differences. An example is the vector meson $\rho$ whose chiral partner, the axial vector meson $a_1$, is nearly twice as heavy. The mass splitting between parity partners will decrease when the symmetry breaking reduces, and finally the partners will become degenerate as symmetry is restored.

For temperatures $T{>}T_c$, the pions are no longer Goldstone bosons. In the plasma phase, massive quasi-particle excitations exist in the pseudo-scalar quantum number channel. Below $T_c$, spontaneous breaking of chiral-flavour symmetry $SU_L(n_f) \times SU_R(n_f)$ leads to the splitting of scalar ($f_0$) and pseudo-scalar ($\pi$) particle masses, while the $U_A(1)$ symmetry breaking is visible in the splitting of the $\pi$ and the scalar $a_0$ meson [8].

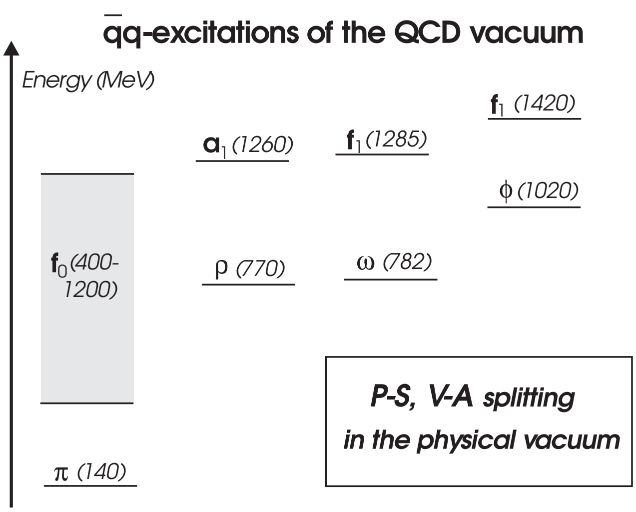


Figure 1.3: *Experimentally observed spectrum of low-mass mesons.*

The lattice results show that the thermal correlation function $G(\tau)$ and the reconstructed spectral function $\sigma(\omega)$ are different at low and at high T. The mesonic correlation function $G_H(\tau, \vec{r}) = \langle H(0, \vec{0})H^+(\tau, \vec{r})\rangle$ (where $H$ is scalar $\overline{q_i}q_j$, pseudoscalar $\overline{q_i}\gamma_5 q_j$, vector $\overline{q_i}\gamma_\mu q_j$ or axialvector $\overline{q_i}\gamma_5\gamma_\mu q_j$), is related to the spectral function

$$G(\tau, T) = \int_0^\infty d\omega\sigma(\omega)\frac{cosh(\omega(\tau - 1/2T))}{sinh(\omega/2T)} \tag{1.9}$$

For small temperatures (T→0), the spectral function has a sharp peak at $m_H$, i.e. the pole dominates. The spectral and correlation functions are then given by the formulae

$$\sigma_H(\omega) = \lambda\delta\left(\omega^2 - m_H^2\right) \tag{1.10}$$

$$G_H(\tau) \sim \frac{\lambda}{m_H}ch(m_H(\tau - \frac{\beta}{2})) \tag{1.11}$$

At sufficiently high temperatures (T→ $\infty$), instead of the sharp ground state peaks broad bumps and continuum-like structures are expected to dominate, approaching the correlation function for freely propagating $q\overline{q}$ pairs with thermal masses. The spectral and correlation functions are then defined as [8, 9]:

$$\sigma(\omega) = \theta(\omega - 2m)\frac{N_c}{4\pi^2}\omega^2\sqrt{1 - 4\frac{m}{\omega}^2}th\frac{\omega}{4\pi}\theta\left(\omega - 2m\right)\frac{N_c}{4\pi^2}\omega^2\sqrt{1 - 4\left(\frac{m}{\omega}\right)^2}th\frac{\omega}{4T} \tag{1.12}$$

$$G_f(\tau) = 2\pi N_c\left(1 - \frac{2\tau}{\beta}\right)\frac{1 + cos^2\left(\frac{2\pi\tau}{\beta}\right)}{sin^3\left(\frac{2\pi\tau}{\beta}\right)} + 4N_c\frac{cos\frac{2\pi\tau}{\beta}}{sin^2\frac{2\pi\tau}{\beta}} \tag{1.13}$$

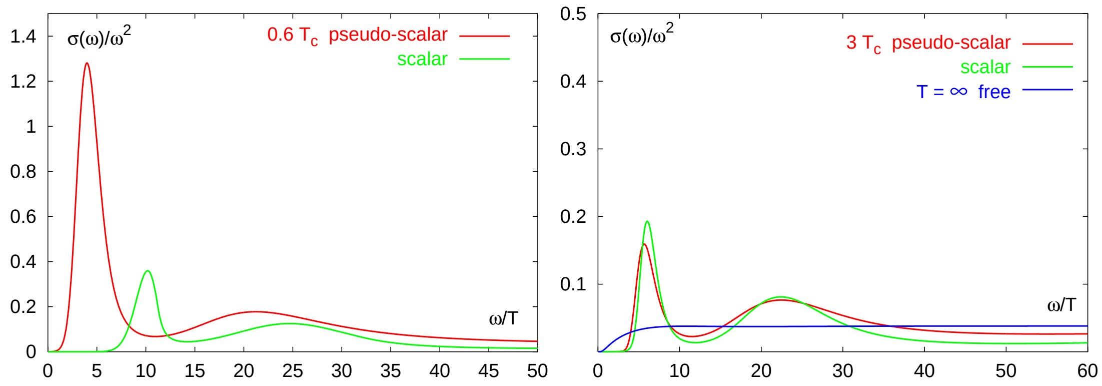


Figure 1.4: *Scalar and pseudoscalar spectral functions at $T = 0.6T_c$ and at $3T_c$ reconstructed from the correlation function. It is visible that a drastic change occurs in the pseudo-scalar channel above $T_c$. The large peak corresponding to the Goldstone pole below $T_c$ is reduced above the critical temperature, scalar and pseudo-scalar correlation functions coincide and the pion pole disappears [10].*

At high T>$T_c$, pseudoscalar and scalar spectral functions are identical, the pseudoscalar peak disappears and moves to the scalar sector. This means that the $U_1(A)$ symmetry is restored at high temperature. The vector and axialvector correlators are also expected to become identical. The vector channel also shows a pole at low temperatures and a continuum distribution at high temperatures, propagating like a free q-propagator at T>$T_c$ (Fig. 1.4) [10].

The observation of parity mixing would be a unique signal for chiral restoration. In heavy-ion collisions it is very difficult to measure the scalar and the pseudoscalar correlator, because pions interact strongly. The best probe is then the vector correlator which couples to photons or dileptons which only interact electromagnetically, i.e. weakly.

The present lattice calculations can only explore systems at finite temperature, but not at finite baryon chemical potential. For that reason only the temperature dependence of strongly interacting matter has been discussed. However, the results are not directly applicable to present heavy ion experiments, where systems are created at finite baryon density. With the ultimate goal to describe the behaviour of matter at high temperature *and* high density, any experimental signatures for the occurrence of phase transitions in heavy ion collisions are very important to also clarify the relative role of "dense" and "hot" conditions over a wide range of parameters.

### 1.2.2 Electromagnetic Probes of Nuclear Collisions

The hot system created in the collision of heavy nuclei at high energies rapidly expands and cools down, emitting dominantly pions and other hadrons. It is now known that these hadrons resemble apparent chemical and thermal equilibrium at freeze-out in terms of particle composition and transverse momentum distributions, carrying little if any information on the primordial history of the fireball evolution. In contrast to hadrons, dileptons (and photons) directly probe the earlier stages; the instantaneous emission after creation and the absence of any final state interaction conserves the primary information within the limits imposed by the space-time folding over the emission period.

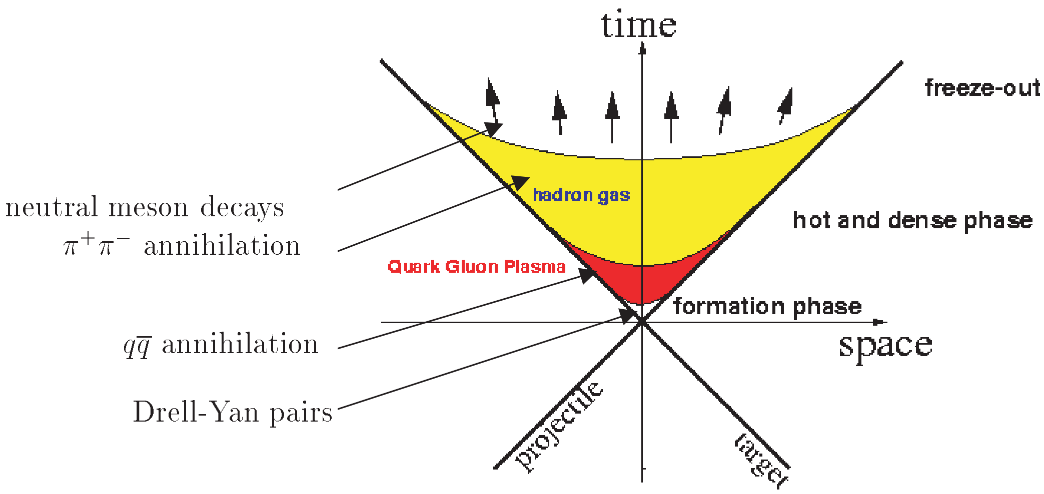


Figure 1.5: *Emission of dileptons from various stages of the fireball evolution, starting at the pre-equilibrium phase. The experimental spectra are always a superposition of the different sources, folded over the full space-time history.*

The finally measured dilepton spectra can be chronologically ordered into several emission phases (see Fig 1.5) [11]:

- 1) Before the nuclear surfaces actually touch, dileptons are produced through coherent Bremsstrahlung. This part populates very low transverse momenta and has so far not been experimentally investigated.
- 2) Within the first 1 fm/c of the nuclear overlap, the excited hadronic system is far from thermal equilibrium. The 'pre-equilibrium' dilepton radiation emitted at this stage mostly consists of hard processes such as Drell-Yan annihilation, leaving its trace mainly at large invariant masses >3 GeV/c$^2$.
- 3) Following deconfinement and rapid thermalisation, dileptons are produced in the partonic phase via $q\bar{q}$ annihilation with characteristic parameters reflecting the early temperature history of the system.

- 4) After cooling and confinement of the partons to a hot hadron gas, dileptons are created in pion and kaon annihilation processes. This annihilation is dominated by the intermediate formation of the light vector mesons $\rho, \omega, \phi$ which directly couple to $l^+l^-$ pairs. The invariant mass of these dileptons directly reflects the spectral functions of the vector mesons at the moment of decay.

- 5) Finally, beyond the freeze-out stage, the remaining sources are hadronic resonance and Dalitz decays (mostly from $\pi^0$, $\eta$ and $\omega$ mesons), all falling into the low mass region with M<1 GeV/c$^2$.

The third and the fourth stage are relevant for deconfinement and chiral symmetry restoration. The strong modification of the thermal environment that occurs during the transition from the quark-gluon to the hadronic phase influences the properties of hadrons. The change of the hadron dispersive properties, i.e. of their masses and widths in a thermal bath is connected to chiral symmetry restoration. The life time of the pions is at least six orders of magnitude larger than the lifetime of the fireball produced in the collision of heavy nuclei. Pions therefore decay in flight in vacuum, and their mass and width would be the same as in any other experiment. The situation is much more favorable for vector mesons. Most frequently, vector mesons decay into hadrons. However, with a small branching ratio (typically $\sim 10^{-4}$), vector mesons also decay into $e^+e^-$ or $\mu^+\mu^-$ pairs. If the decay occurs inside the interaction region, the leptons convey undistorted information on the in-medium mass and width of the vector meson. The $\rho$ is of particular interest. Due to its small vacuum lifetime (1.3 fm/c), all $\rho$'s produced in the collision decay inside the fireball. These modifications are directly related to thermal dilepton production, and measuring the spectra of $e^+e^-$ or $\mu^+\mu^-$ pairs thus provides information about the properties of the $\rho$ in the hot hadronic medium. The situation is not as clear-cut with $\omega$ and $\phi$ mesons. Their life-time, 23 and 44 fm/c, resp., is 2-4 times larger then the life time of the fireball, implying that most of the decay occurs in vacuum, largely masking the (smaller) medium-connected part.

To summarize: In the low mass region, the thermal radiation is dominated by the decays of the light vector mesons $\rho, \omega,$ and $\phi$. The $\rho$, as mentioned before, plays a special role, due to its short lifetime of 1.3 fm/c and its direct link to chiral symmetry; its in-medium behaviour around the critical temperature $T_c$ should therefore reflect the associated restoration of chiral symmetry [12]. In the higher mass region, between the $\phi$ and $J/\psi$, the thermal radiation is expected to be continuum-like and dominated by $q\overline{q}$ annihilation, a direct signal for quark matter formation as first proposed by Shuryak in connection with $pp$ collisions [13]. Dileptons originating from $\pi^+\pi^-$ annihilation have a threshold at $2m_\pi$ and a broad peak around the mass of the $\rho$ meson, while $q\overline{q}$ annihilation yields an exponential shape.

### 1.2.3 Previous Results from CERES

Experimentally, low mass dileptons are very much the domain of NA45/CERES, the only electron pair spectrometer at the SPS, while higher mass dileptons are the domain of NA38/NA50, a muon pair spectrometer at the SPS. During the S-beam era, another muon pair spectrometer, NA34/HELIOS-3, has also been in operation. Both muon

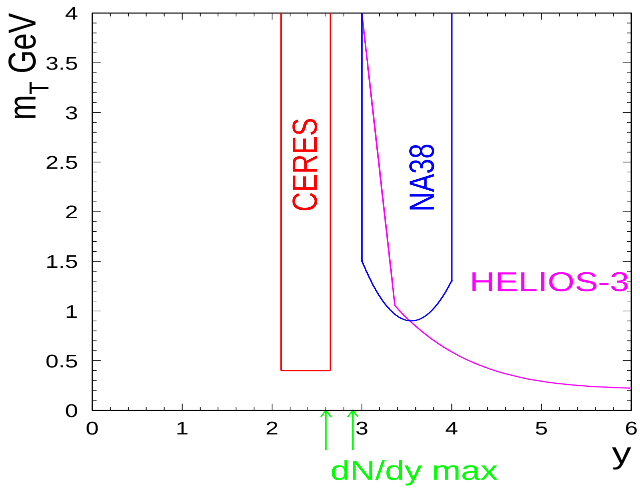


Figure 1.6: *Kinematical regions covered by the three experiments that have measured dilepton spectra.*

pair experiments have had some sensitivity to low-mass pairs as well. The kinematical regions covered by the three experiments are shown in Fig 1.6.

The CERES experiment is in many ways different from the other two. Among its advantages is its acceptance close to mid-rapidity, while the HELIOS-3 experiment and NA38/50 cover more forward rapidities. A very important issue for the measurement of low mass dilepton spectra is the absence of a low-$p_t$ cut-off which makes CERES/NA45 really unique. All results on low-mass dileptons observed so far show the medium modifications of the dilepton producing processes to be very much localized at low $p_t$ (see below).

The history of the CERES experiment and a list of the essential physics results is contained in Table 1.1. The results can be summarized as follows. In proton induced reactions like p-Be and p-Au, the measured pair rate agrees, within errors, with the expectation from hadronic decays like $\pi_0$ Dalitz, $\eta$ Dalitz...(see Fig. 1.7) [14, 15]. For nuclear projectiles, however, the situation is drastically different. In the first measurements at the CERN-SPS with a 200 AGeV S beam, CERES found an excess of measured pairs over the expectation from hadronic decays by a factor of 5.0 $\pm$0.7(stat)$\pm$2.0(syst), integrated over the mass range 0.2-1.5 GeV, in central collisions of S+Au [16, 17]. The 1995,96 runs with 158 AGeV Pb projectiles confirmed the S results. Here, the (averaged) enhancement was found to be 2.8$\pm$0.3(stat)$\pm$1.0(syst.) compared to the hadronic decay sources (for the upper 30-35$\%$ of the geometrical cross section). As already seen in S+Au, the enhancement is mostly localized between 0.2 and 0.7 GeV/c$^2$ (see Fig. 1.8) [18, 19, 20, 21, 22, 23].

CERES has also looked at other features of data, in particular the pair-$p_t$, the total momentum of the dilepton pair perpendicular to the beam axis of the colliding nuclei. The transverse momentum spectra in several invariant mass bins (see Fig 1.9) have similar statistical and systematical errors as the invariant mass spectra. The results show reasonable agreement with the expectation from hadronic decays except for the mass bin of 0.2 GeV/c$^2$ $<$ m $<$ 0.6 GeV/c$^2$ where the excess is localized; here the pt-

| | |
|---|---|
| 1988 | submission of proposal |
| 1989 | approval by CERN as NA45 |
| 1990 | first test run; detectors complete, electronics 10% |
| 1991 | spark problem solved; first test run with S |
| 1992 | 200 AGeV S-Au production run, 8 Mill events<br>445±65 $e^+e^-$ pairs with S/B=1/4.5 |
| 1993 | 450 GeV p-Be production run, 30 Mill(2 Bill) events<br>5760±180 $e^+e^-$ pairs with S/B=1/2 |
| 1993 | 450 GeV p-Au production run, 8Mill(0.3Bill) events<br>1130±100 $e^+e^-$ pairs with S/B=1/4.5 |
| 1994 | first test run with Pb |
| 1995 | 160 AGeV Pb-Au production run, 8.5 Mill events<br>648±105 $e^+e^-$ pairs with S/B=1/8 |
| 1996 | 160 AGeV Pb-Au production run, 42 Mill events<br>2018±237 $e^+e^-$ pairs with S/B=1/13 |
| 1996 | submission of TPC upgrade proposal |
| 1998 | first test run of TPC with Pb |
| 1999 | 40 AGeV Pb-Au production run, 8 Mill events |
| 2000 | 160 AGeV Pb-Au production run, 33 Mill events |

Table 1.1: *Summary of the dilepton program of CERES at the CERN-SPS over the last 14 years.*

spectra are dominantly concentrated at very low transverse momenta $p_t < 0.5$ GeV/c. The other projection of the data, namely mass spectra for two distinct regions of transverse pair momentum ($p_t$<0.5 GeV and $p_t$>0.5 GeV) show, of course, the same features: the major part of the low-mass enhancement is localized in the low-momentum region, while in the high momentum region the mass spectrum is mostly consistent with the decay cocktail.

From these results it is clear that the cut-off in transverse mass at about $m_t$=1GeV in NA38/50 and $m_t$=0.5GeV in NA35/HELIOS-3 creates severe problems for the measurement of low-mass pairs. The strong $p_t$-dependence of the observed enhancement makes CERES/NA45 indeed unique for low-mass dilepton measurements.

### 1.2.4 Theoretical Description of Previous CERES Results

The production cross section of lepton pairs is proportional to the thermally averaged isovector current-current correlation function $\langle\langle j^V_\mu(x) j^V_\nu(0)\rangle\rangle$, the conserved current ($\partial^\mu j^V_\mu = 0$) of $SU_R(n_f) \times SU_L(n_f)$ chiral symmetry. The dilepton spectrum may therefore contain information on the existence of a phase of restored chiral symmetry, created in heavy ion collisions [26, 27]. The nature of the chiral phase transition is strongly influenced by the non-vanishing current quark masses, leading to a continuous variation of the quark condensate with density and temperature. Conceivably, this would be observable e.g. in the dilepton mass spectrum as a change of the hadron

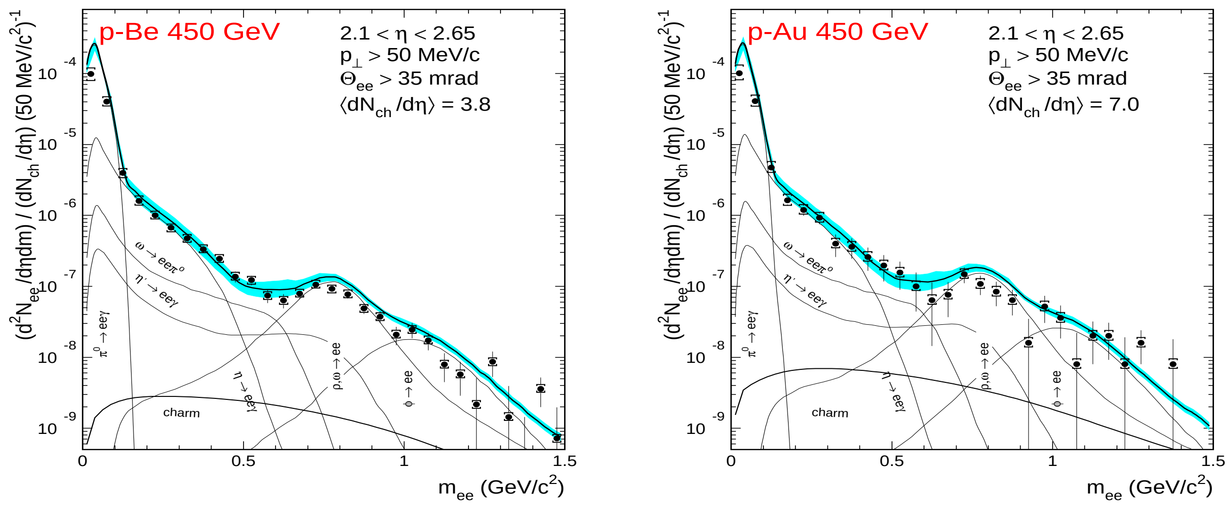


Figure 1.7: *Normalized invariant mass spectra of dileptons as measured in 450 GeV proton-induced collisions on Be (left panel) and Au targets (right panel). The data are compared to expectations from various hadron decay channels (labelled explicitly), based on measured branching ratios of all relevant decays and knowledge of the total cross section of neutral mesons measured in pp collisions. The bands indicate the systematic uncertainties in the cocktail [14, 15].*

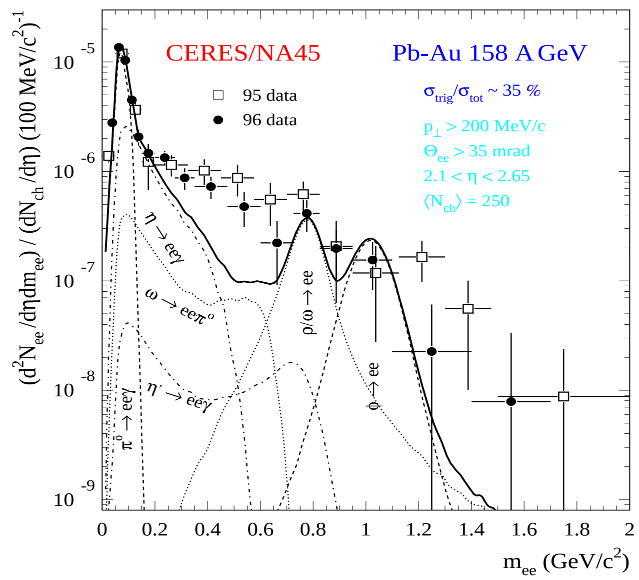


Figure 1.8: *Normalized invariant mass spectra of $e^+e^-$ pairs for the two data sets of 1995 and 1996 in comparison to the known hadronic decay sources, showing the individual contributions [18, 19, 20, 21, 22, 23]. The total cross section of the neutral mesons relative to pions is taken here from the statistical model applied to Pb-Au collisions [24, 25]. The mass resolution is improved to ∼5.5% compared to Fig. 1.7.*

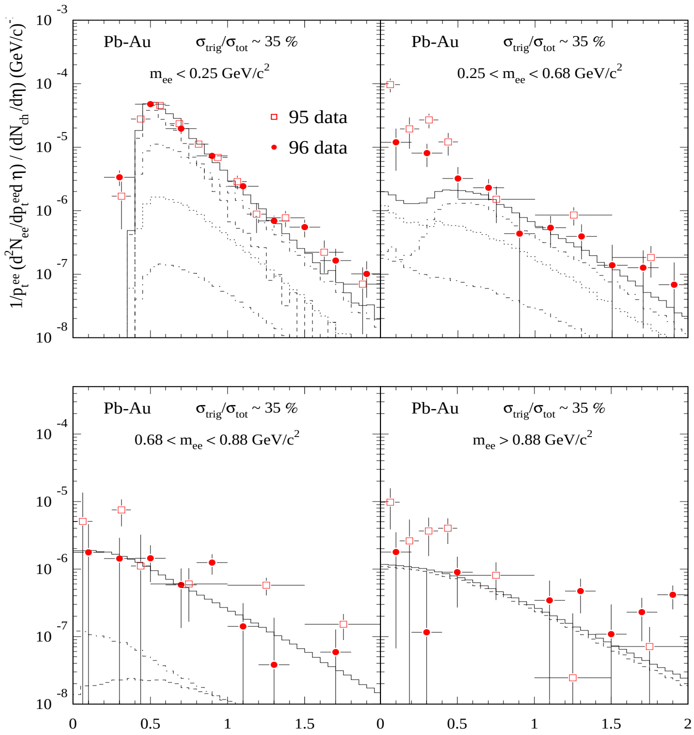


Figure 1.9: *Pair transverse momentum spectra in four invariant mass bins for the two data sets of 1995 and 1996 for 158 AGeV Pb-Au collisions. The data are compared to the hadronic decay sources, showing the individual contributions (see Fig. 1.8).*

properties (masses, widths). Although at full SPS energy, 160 AGeV, the phase space in the final state is dominated by mesons (mostly pions) with a meson/baryon ratio of about 10, the influence of the baryons cannot at all be ignored. Much theoretical effort has been devoted in the last few years to understand the nature of chiral symmetry restoration and the associated change of hadron properties (in particular, of the vector mesons) at finite T *and* finite baryochemical potential. Only the summary of the basic ideas will be given in this section; a much more detailed discussion will be presented in chapter 7 below.

Consistent with the apparent onset of the excess in the electron pair mass spectrum around 2m$_\pi$, the pion-pion annihilation channel $\pi^+\pi^- \rightarrow \rho^* \rightarrow e^+e^-$ with an intermediate $\rho^*$, in the spirit of "vector-dominance", has received the greatest attention. The in-medium effects associated with the intermediate $\rho^*$ can be subdivided into two major scenarios:

- 1) In-medium "dropping" $\rho$-mass m$^*_\rho$

  This approach, based on effective mean-field theory and essentially of "partonic" nature, has been pursued by Brown, Rho et al. [29]. It links a temperature- and baryon-density dependent reduction of the $\rho$-mass directly to the corresponding medium-induced change of the chiral condensate according to Brown/Rho

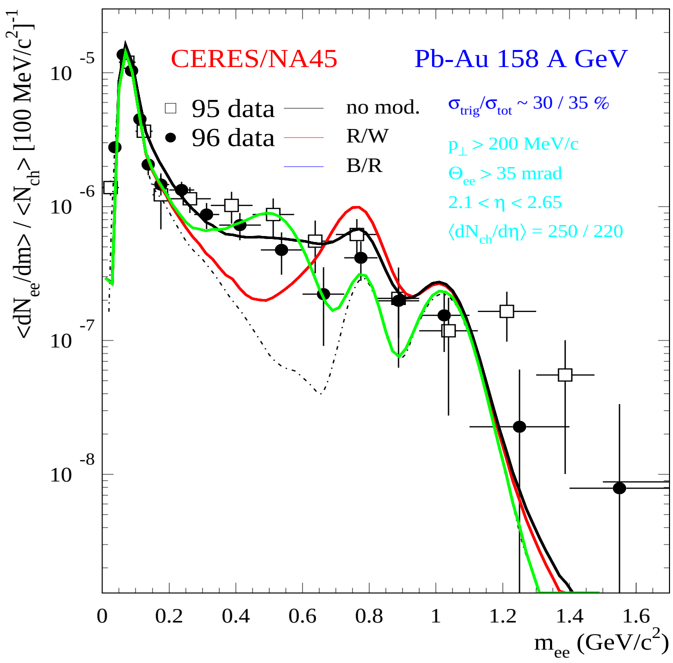


Figure 1.10: *Normalized invariant mass spectra of $e^+e^-$ pairs at 160 AGeV for the two data sets 1995 and 1996 in comparison to model calculations [28], based on $\pi^+\pi^-$ annihilation with an unmodified $\rho$ (red thick solid), an in-medium dropping $\rho$ mass (green thick solid) and an in-medium spreaded $\rho$ (black thick solid); the sum of the hadronic decay sources, but without the $\rho$, is shown separately (thin dashed-dotted line), but is of course contained in the model calculations.*

scaling $m_\rho^*/m_\rho^0 = \langle\overline{q}q\rangle^*/\langle\overline{q}q\rangle^0$ [30, 31]. The pion propagation remains unchanged, creating a sharp threshold at 2m$_\pi$.

- 2) In-medium "spreaded" $\rho$-mass m$_\rho^*$

  This approach, using a "hadronic" base, has been pioneered by Rapp, Wambach et al. [11, 32]. They consider in-medium modifications of the current-current correlator, the imaginary part of which is directly related to the dilepton production rate. Both the $\pi$ and the $\rho$ properties are modified due to the interactions with the surrounding hadrons, in particular baryons, in the hot and dense hadronic medium. All resulting effects are expressed in terms of an in-medium "$\rho$-spectral function" which extends, due to the change in the pion dispersion relation and to the incorporation of $1\pi$ processes, well below the 2m$_\pi$ threshold.

It is remarkable that, in both scenarios, (baryonic) density seems to play a more important role than temperature. Although the predictions are quite model-dependent, the data are described reasonably well (see Fig. 1.10), with some preference (even within present errors) for the spreaded-$\rho$ scenario. An unmodified $\rho$, i.e. a vacuum spectral function, is clearly ruled out.

### 1.2.5 Motivation for this Thesis

This thesis focuses on the first results from CERES obtained at a lower SPS beam energy. The results are based on data taken for Pb-Au collisions at 40 AGeV during the running period 1999. After the observation of a strong enhancement of low-mass dilepton production as compared to proton-nucleus collisions at full SPS energy, the theoretical efforts to describe the enhancement and to establish the correctness of the interpretation called for a systematic variation of the essential variables, temperature and baryon density.

A comparison between different beam energies (160 vs. 40 AGeV) is *the* way to vary and thus elucidate the relative importance of temperature and baryon density. Fig. 1.11 shows a three-dimensional plot of the dependence of the quark condensate $\langle \overline{q}q \rangle$ on the two variables. Close to the vacuum value, the functional dependences on temperature and density can be described by equations 1.14 and 1.15 [33]:

$$\langle \overline{q}q \rangle_T / \langle \overline{q}q \rangle_0 \approx 1 - (T/f_\pi)^2/8 + O(T^4) \tag{1.14}$$

$$\langle \overline{q}q \rangle_\rho / \langle \overline{q}q \rangle_0 \approx 1 - 0.33\rho/\rho_0 \tag{1.15}$$

Outside the validity of the approximations used for these equations, the monotonic decrease of $\langle \overline{q}q \rangle$ is qualitatively continued down to the level of zero, corresponding to complete restoration of chiral symmetry. Two dynamical trajectories for nuclear colli-

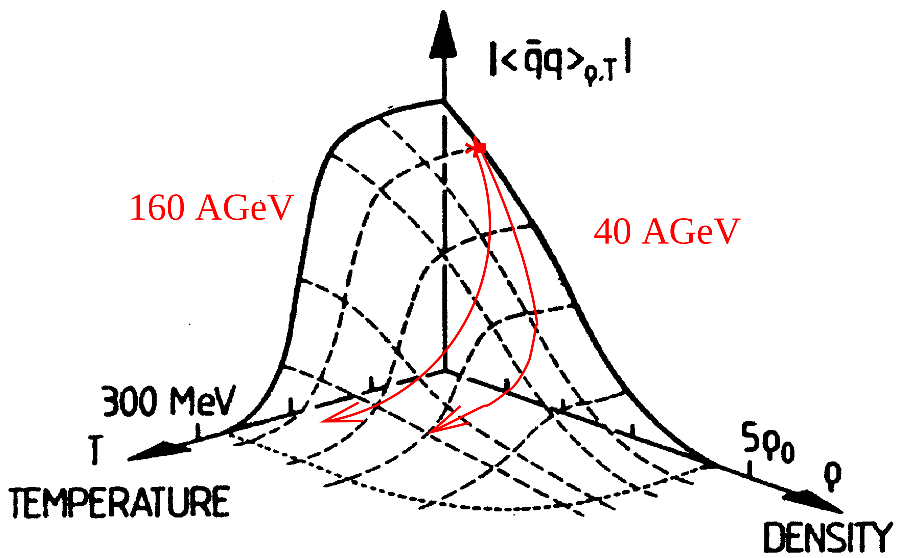


Figure 1.11: *The quark condensate as a function of temperature and nuclear matter density from the Nambu and Jona-Lasino model [33, 34].*

sions, one for the full and the other for a much lower SPS energy, are also contained in Fig. 1.11. They qualitatively illustrate the expected behaviour: a higher temperature and lower baryon density for the higher beam energy, and a lower temperature and higher baryon density for the lower beam energy. This is true for each path element of the trajectories, including the final freeze-out region. Experimentally, the meson/baryon ratio for central rapidities decreases from about 10 at 160 AGeV to about 5 at 40 AGeV, decreasing still further towards AGS energies. As mentioned already in the previous section, the main theoretical scenarios for the in-medium changes of the intermediate $\rho^*$ find baryon density to be more important than temperature. Consequently, stronger in-medium effects would have to be expected for the lower beam energy of 40 AGeV than for the full SPS energy of 160 AGeV. In more general terms, temperature and baryon density influence dilepton production significantly and in different ways. Comparing the results for different beam energies should therefore help to better understand the change of the hadronic properties in a dense and hot nuclear environment, to clarify the connection to chiral symmetry restoration and to provide additional constraints for the model calculations.

# Chapter 2

# The CERES Experiment

## 2.1 Experimental Setup

CERES/NA45 has so far been the only electron-pair experiment in the field of ultrarelativistic nuclear collisions. Its basic design has been optimized for the measurement of pairs in the low-mass region, i.e. for masses $<$1 GeV/c$^2$. As mentioned before, the principal advantages compared to muon pair experiments are the acceptance close to mid-rapidity and the absence of a low-$p_t$ cut-off. Inevitably coupled to this are the disadvantages compared to muon pair experiments, a smaller acceptance and a limited rate capability, excluding any reasonable sensitivity for masses $>$ 1.5 GeV/c$^2$.

Beyond the mass region dominated by $\pi^0$-Dalitz decays, the physics signal of interest consists of electron-positron pairs in the invariant mass range 0.2<m<1 GeV/c$^2$. The abundance of these pairs is only of order $10^{-5}$ relative to (i) hadrons and (ii) photons. The experimental challenges are therefore extremely high. They are dealt with in the following way:

i) Hadron-electron separation on the level required is assured by the use of Ring Imaging Cherenkov detectors, supplemented in 1999/2000 by $dE/dx$ information from a TPC.

ii) Very-low-mass electron pairs from photon conversions ( creating, if not recognized, a huge combinatorial higher-mass background, see 3.5) are suppressed as much as possible by minimizing the total material in the experiment to about 1$\%$ of a radiation length. To aid the rejection of the remaining part, the opening angle information is consistently kept.

A schematic view of the CERES spectrometer is shown in Fig. 2.1. The left side contains the original CERES setup as used up to 1996 [35]. Two silicon drift chambers (SIDC1/2), located 10 cm and 13.8 cm behind a segmented Au target, provide a precise angle measurement of the charged particles and precise vertex reconstruction, resolving the target segments. The discrimination between the rare electrons and the abundant hadrons is done with two Ring Imaging Cherenkov detectors (RICH1/2), operated at a high threshold $\gamma_{th}$=32 which rejects 95$\%$ of all charged hadrons. For the running period 1999/2000, the spectrometer was upgraded with a radial drift Time Projection Chamber (TPC) [36] for tracking and momentum measurement, replacing

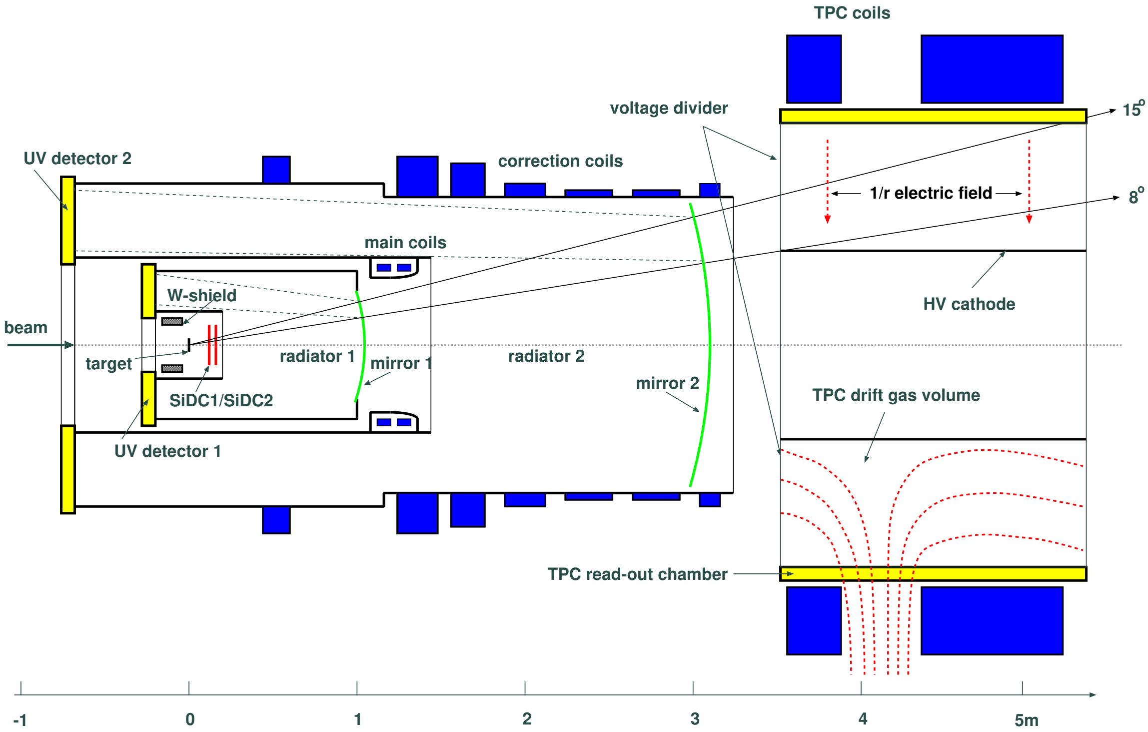


Figure 2.1: *Schematic view of the upgraded CERES spectrometer at the CERN SPS.*

the original pad chamber behind mirror 2, and a new magnetic field configuration, replacing the original B-field between the two RICH's. The results of these changes are the following:

- Better mass resolution: With an active length of 2 $m$, an outer diameter of 2.6 $m$, up to 20 space points for each track and a maximal radial field component of 0.5 T, the mass resolution is improved from the 1995/96 value of 5.5$\%$ to a level of $\sim$2$\%$ in the region of the $\rho/\omega$; only $\sim 4\%$ was, however, reached for the 1999 data set (the experiment was not quite ready yet).

- Better RICH efficiency: Since the original magnetic field is switched off, the two RICH detectors are now used as an integral unit, resulting in improved efficiency (0.94 instead of 0.81·0.86 = 0.70 in 1995/96) and improved rejection power.

In the following, the different components of the experiment are described in more detail.

## 2.2 The Target

The target region consists of the target itself and two radial silicon drift detectors, all concentrated in a limited volume of $\sim$12 $cm$ length and $\sim$14 $cm$ diameter as shown in

Fig. 2.2. Target and detectors are held mechanically in a common structure provided by a double wall carbon fibre tube, independent of the rest of the spectrometer. The beam enters via an evacuated, removable Al tube that reaches until a few $mm$ short of the target assembly [23, 35]. The tube is surrounded by a cooling system needed to isolate the silicon wafers from the rest of the spectrometer which is heated to $50^o$ C. The target

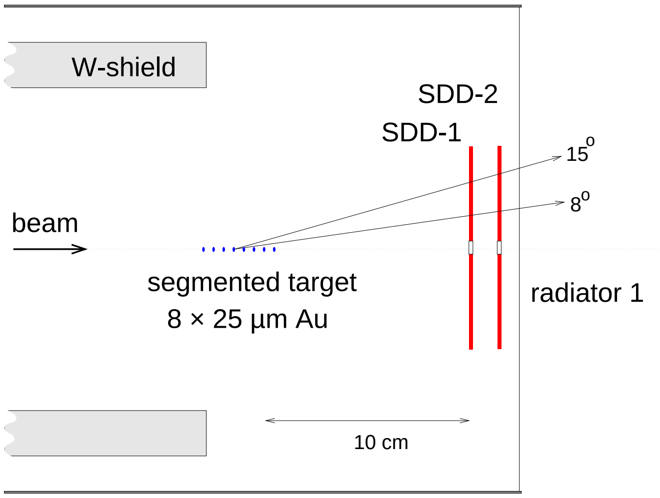


Figure 2.2: *Target area with the two SDD detectors.*

itself is segmented in order to minimize its effective radiation length, i.e. the number of conversion pairs produced by the secondary photons from the interaction. The target used in 1999 was segmented into 8 individual Au-disks with a diameter of 600 $\mu m$ each. The spacing between the disks of 2.8 $mm$ assures complete isolation of the interaction, i.e. on average only half a disk (0.37 $\%$ of a radiation length) contributes to photon conversions within the acceptance of the spectrometer. The total target thickness of 200 $\mu m$ Au is equivalent to an interaction length of $\lambda/\lambda_I$~0.83 $\%$.

## 2.3 The SIDC Detectors

The two radial silicon drift detectors with 4$''$ diameter cover a rapidity acceptance of 1.95<$\eta$<3.21 with full azimuthal symmetry. Within the overall concept of the experiment, they have the following functions:

- Measurement of the charged particle rapidity density dN$_{ch}$/d$\eta$ and thereby characterisation of the event.

- Very precise vertex reconstruction without the need of additional information from other detectors. Given the high radial resolution of potentially 30 $\mu m$, even the small spacing of 38 $mm$ between them is completely sufficient to resolve the individual target disks (see 3.3.2).

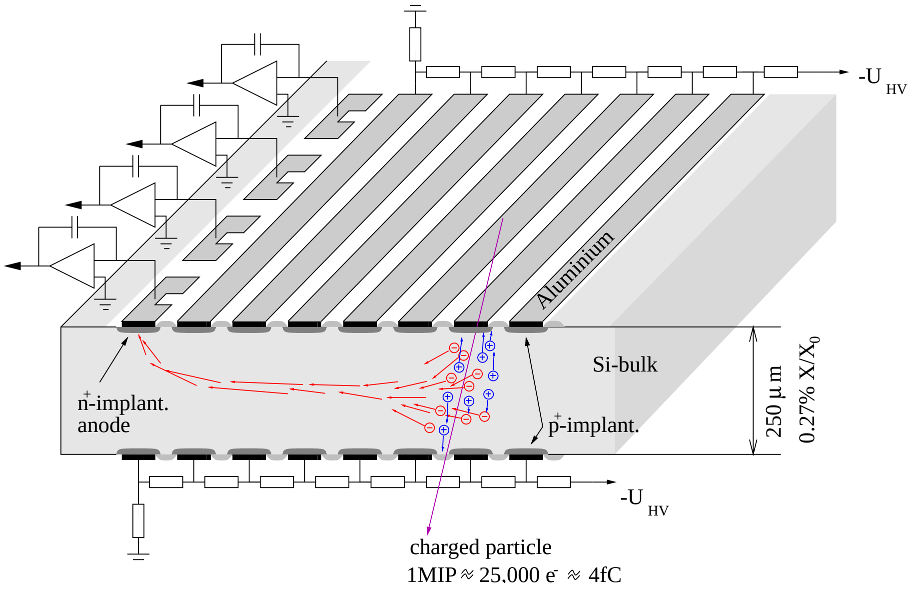


Figure 2.3: *Working principle of the Si-drift detector.*

- Tracking of electrons within the spectrometer, reducing the fake-ring problem in the RICH detectors by predicting the center of candidate rings.

- Efficient identification and thereby efficient rejection of close pairs from photon conversions and $\pi^0$-Dalitz decays by the measurement of ionisation for each track as well as by the recognition of close hits. This is one of the most important tools for reducing the combinatorial background (see 3.5).

- Independent physics studies like elliptic flow and two particle correlations.

The working principle of the Si-detectors is schematically illustrated in Fig. 2.3. The electron-hole pairs ($\sim$ 25000) created by a traversing charged particle in 250 $\mu m$ of Si are separated by an applied electric field, and the electrons then drift radially outwards towards the anodes. The drift field is generated via ring-shaped implanted voltage dividers from the total voltage $U_{HV}$. Knowing the drift velocity, the particle coordinates can then be reconstructed from the hit anode(s) and the drift time. The number of anodes around the circumference, 360, determines the azimuthal resolution; diffusion and signal-to-noise together with the granularity of the time measurement, 50 MHz, determine the radial resolution.

An example of a SIDC event display is shown in Fig. 2.4. An occupancy on the level of hundreds of charged particles can easily be accepted, corresponding to pile-up losses of only a few $\%$ (see 3.3.3).

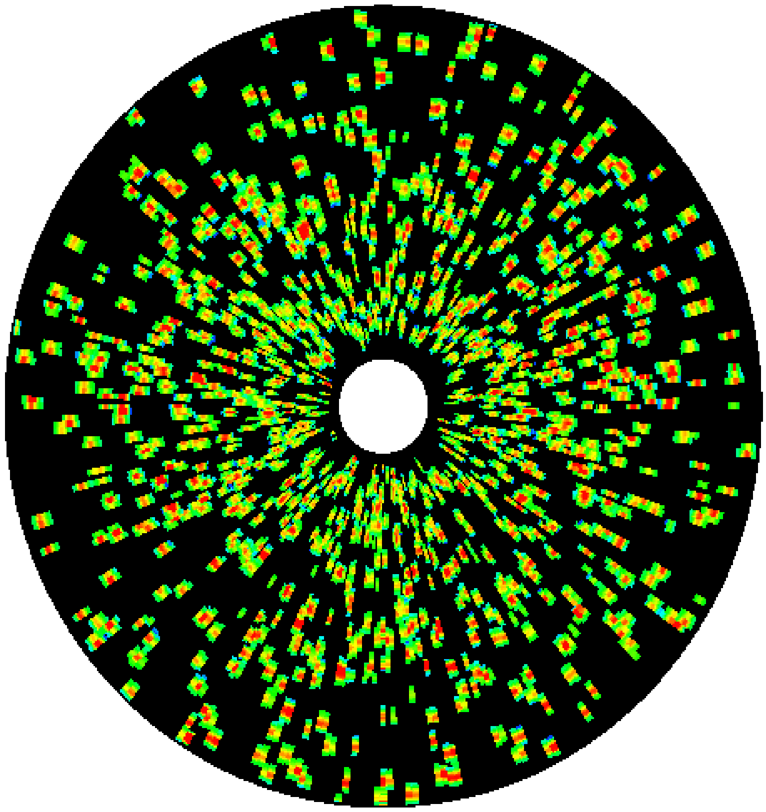

Figure 2.4: *Event display of the SIDC1 detector.*

## 2.4 The RICH Detectors

The RICH detectors are the heart of the electron spectrometer. Their rapidity acceptance is 2.0< $\eta$ <2.65, close to the central region, and has full azimuthal symmetry for optimal geometrical efficiency. The basic concept of a RICH detector is the following: When a charged particle with sufficient velocity (see below) traverses a radiator medium, the Cherenkov photons produced are focused by a spherical mirror onto a UV-sensitive detector, creating a ring-like image. In the CERES case, the UV-detectors are placed upstream of the target and are therefore not subject to the large flux of forward-going charged particles (see Fig. 2.1). In order to minimize the number of $e^+e^-$ pairs from conversions, the amount of material within the acceptance is made as small as possible. For this reason, the mirror of RICH1 is based on carbon fiber with only 1 mm thickness, while the second mirror is a conventional 6 mm glass mirror. All in all, the total radiation length is kept to about 0.4 $\%$ and 1.6 $\%$ of $X_0$ up to the first and the second mirror, respectively, excluding the target.

The UV-sensitive gas detectors have three amplification stages, two Parallel-Plate Avalanche Chambers (PPAC) and one Multi-Wire Proportional Counter (MWPC). The gas mixture is 94% Helium/6% Methan, and incoming UV-photons are converted into electrons via photoionisation of TMAE as a photosensitive agent. To increase the partial pressure of TMAE to a level required for a sufficiently small mean free path for photon absorption (6.6 mm), the TMAE is heated to $40^{o}C$. The detectors are operated at atmospheric pressure and are kept, together with the radiators, at a temperature of $50^0\ C$ in order to prevent TMAE condensation. The information of the detectors is read out via two-dimensional arrays of about 50000 pads each, allowing reconstruction of the single-photon hits. The fast pad readout together with the possibility to operate on subsets of the pad information has made ring recognition possible at the trigger level.

The radiators are filled with $CH_4$ at atmospheric pressure. The $CH_4$ index of refraction $n$ is such that the threshold for Cerenkov radiation is reached at a Lorentz factor of $\gamma_{th}$=32. This means that electrons produce coherent Cherenkov light with an asymptotic emission angle of

$$\theta_\infty = (\frac{1}{\gamma_{th}}) = 31.5mrad. \tag{2.1}$$

Except for pions with a momentum of more that 4.5 GeV/c (whose velocity satisfies the condition $\beta > 1/n$), 95% of all hadrons produce no signal, i.e. the RICH is "hadron blind". The ring image in the focal plane has a radius

$$R = R_\infty \left[1 - \left(\frac{\gamma_{th}}{\gamma}\right)^2\right]^{\frac{1}{2}} \tag{2.2}$$

where $R_\infty = f \cdot \theta_\infty$ is the asymptotic radius of particles with $\gamma >> \gamma_{th}$ ($f$ focal length of the mirror). Geometrically, $R_\infty$ corresponds to ~16 pad units. RICH detectors measure only angles of trajectories, meaning that particles travelling at identical angles will produce ring images at the same place in the UV detector. The number of emitted photons on the rings is given by

$$N = N_\infty \left[1 - \left(\frac{\gamma_{th}}{\gamma}\right)^2\right] \tag{2.3}$$

where $N_\infty$ is the asymptotic number of reconstructed photons for $\gamma >> \gamma_{th}$. Typical values are ~11 for RICH1 and 9-10 for RICH2 (see subsection 3.4.2).

## 2.5 The TPC

As mentioned before, the main purpose of the new radial Time Projection Chamber (TPC) added to the CERES spectrometer is to improve the momentum- and thereby mass resolution, allowing to more clearly resolve the vector meson resonances $\rho$, $\omega$, and $\phi$ than has been possible in the 1995/96 set-up. A cross section of the cylindrical TPC is shown in Fig. 2.5. The acceptance of the TPC covers the polar angular range $8^0 < \theta < 15^0$ with full coverage in azimuth, implying that the acceptance of the original spectrometer remains unchanged by the addition of the TPC (with the compromise of

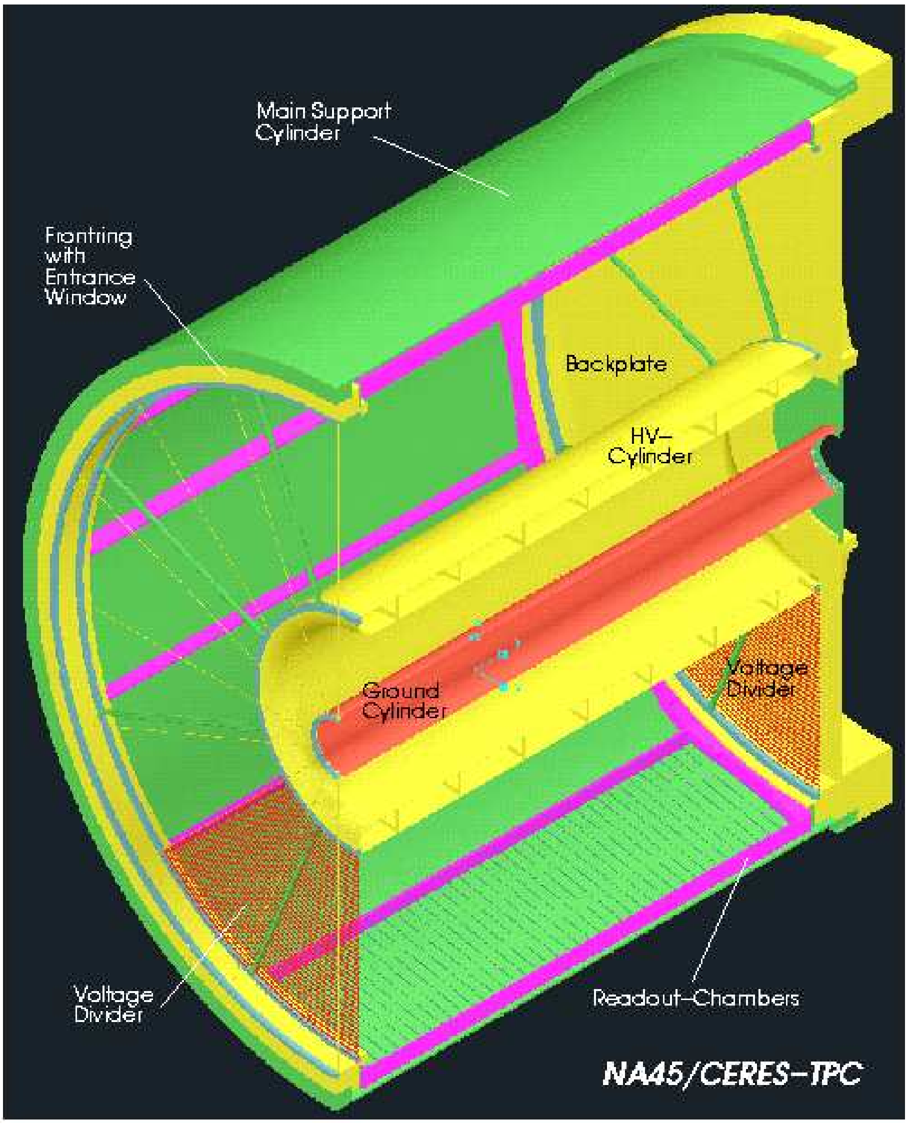


Figure 2.5: *Cross section through the CERES TPC.*

shortened tracks for large $\theta$). The active volume extends from 3.7-5.7 $m$ downstream of the target. The TPC has an active length of 2 $m$, an inner radius of 48.6 $cm$ and an outer radius of 132 $cm$. The magnetic field is generated by two warm coils with currents running in opposite directions. This results in a radial field with maximum strength in the region between the two coils, deflecting the particles in azimuthal direction. The bending power is 0.18 Tm at $8^0$ and 0.38 Tm at $15^0$. Precise measurement of the $\phi$ deflection in the TPC determines the momentum of the particles. However, the track measurement in the $\phi$ direction is influenced by the Lorentz angle of the drifting cloud which has to be sufficiently well known.

The charged particles traversing the counter gas volume of the TPC produce electron-ion-pairs along their trajectory. The electrons drift in radial direction along the lines of the electric field and reach one of the sixteen readout chambers at the outer side. The readout chambers (see Fig. 2.6) are conventional multi-wire proportional chambers with cathode pad-readout and have a size of $2 \cdot 0.5\ m^2$ each. There are 20 pad rows in beam (z) direction with 16·48 pads in azimuthal direction, each sampling the radial (drift) direction. Three wire planes are running in azimuthal direction. The avalanche

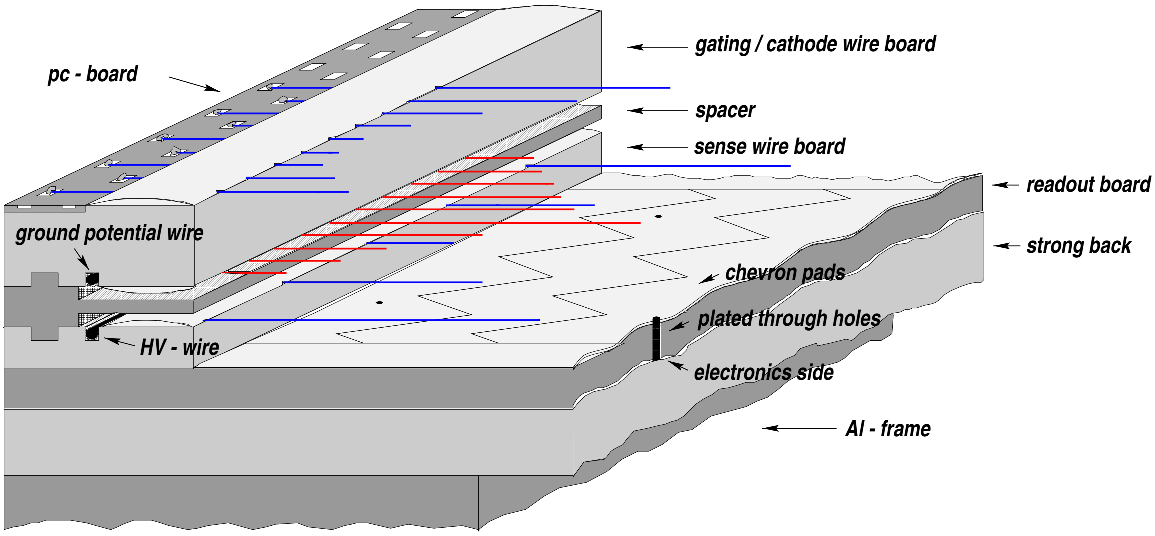


Figure 2.6: *Cross section through one side of the readout chambers.*

produced close to the anode wires induces a signal in the chevron-type cathode pads. The chevron pad shape was selected because of its efficient charge sharing in azimuthal direction and was optimized to minimize the differential non-linearity. The charge is mainly distributed over three pads with size of $6 \cdot 10.3$ mm$^2$. In the case that a charge cloud arrives exactly in the middle of a pad, the central pad will contain 80% of the charge. The expected resolution is 250-350 $\mu$m in azimuthal and 400-500 $\mu$m in radial direction, depending on the polar angle. The analog signals from each pad are sampled in 256 time bins. Altogether, the TPC has $48 \cdot 16 \cdot 20$=15360 readout channels and gives a measurement of up to 20 space points per particle track. The total volume is 9 $m^3$ and is filled with a Ne(80%)/$CO_2$(20%) gas mixture. This particular choice reflects an optimization in terms of many different aspects: small diffusion, small Lorentz angle, large ionization, fast drift velocity and small radiation length .

## 2.6 The Trigger and DAQ

### The Trigger

The data were taken with a central trigger based on three small Cherenkov beam counters and the SIDC1 detector. The detector readout is triggered, if a beam-particle reaches the target, but does not enter the spectrometer. This is done in the following way:

1) A minimum bias trigger is defined using three $CO_2$ filled Cherenkov counters BC1, BC2, and BC3, placed in the beam. BC1 is located about 60 m upstream of the spectrometer, while BC2 and BC3 are placed directly before and after the target, respectively. BC1 is used for monitoring of the incident beam particles, BC2 for detecting ions passing through the spectrometer, while BC3 is used to record each Pb ion escaping from the target in order to prohibit non-interactions with high efficiency. The minimum bias trigger requires a signal in the first two and no signal in the third BC counter:

$$\mathrm{MINB} = \mathrm{BC1} \cdot \mathrm{BC2} \cdot \overline{\mathrm{BC3}}. \tag{2.4}$$

2) In 1996 for the beam energy of 160 AGeV, the centrality selection has been done by using a multiplicity detector (MD). However, in 1999 for the beam energy of 40 AGeV, the multiplicity detector (MD) could not be used because of the wrong rapidity coverage, shifted away from mid-rapidity. For that reason central events were selected in 1999 by placing a lower limit on the integrated signal of the SIDC1 detector, the signal being proportional to the number of charged particles hitting the detector. This information was available only after 4 $\mu s$, corresponding to the maximum drift time of the detector, and thus the centrality requirement was implemented as a second-level trigger [37, 38]. The centrality threshold was set to correspond to about 30 $\%$ of the geometrical cross-section $\sigma_{geo}$.

### The Data Acquisition System DAQ

After the CERES experiment was upgraded by adding the TPC, a new data acquisition system was needed in order to cope with the increased event size [37]. Events are triggered by beam particles with an intensity of $10^6$ ions per burst, entering the target area. A typical central Pb-Au event, after zero suppression, has a size of 0.4-0.5 MByte. During the SPS burst, i.e. during the five seconds of beam interactions onto the target, typically 200-600 multiplicity-triggered collisions can be recorded. In the 15 seconds interval between two bursts, the collected data are sent to an event-builder PC in the CERN Central Data Recording facility (CDR), and the saved data are then copied from disk to tape.

# Chapter 3

# Data Analysis

## 3.1 Data Sample

The data analyzed in this thesis were taken in the fall of 1999 with a 40 AGeV Pb beam on a Au target. The centrality selection was $\sigma/\sigma_{geo}$ ~30% as mentioned before. The data taking period was originally planned to extend over 5 weeks. However, this was the first production run in which the new TPC was used. Due to problems with the new readout, the effective running time was very much reduced (to about 10 days), resulting in a final sample size of only 8 Million events. The same problems also caused the TPC readout to be only partially operative, reducing the efficiency and therefore the statistics even further. The final electron pair sample to be analyzed was therefore a factor of 10-20 smaller compared to what could have been achieved under ideal circumstances (see chapter 4).

## 3.2 Analysis Strategy and Production Steps

The data analysis is divided into several stages. The main stages are the following:

(i) Event reconstruction

(ii) Electron-track identification

(iii) Pairing of electron tracks; only storage of events with at least one pair

(iv) Rejection of low-mass pairs on the track- and the pair level

Electron production was done in a very elegant and efficient way, with a lot of advantages compared to the hadron production preceding it [39]. Everything possible was done to minimize the dead time and to ease the production process; the data staging and the analysis were done in parallel, the processor was constantly operating until the very last file was analysed. The final output was stored in the form of ROOT files.

With the main goal to reduce the raw data volume as far as possible for effective final analysis, the electron production was divided into three steps of reduction and pre-analysis:

- Production

  In the "production" stage, the reduction was done by applying loose ring quality cuts, accepting only RICH tracks with (truncated) ring analog amplitude smaller than 3000, removing clusters of four and more rings in the small area of 50 mrad, matching SIDC and RICH tracks within a 5 mrad circular window, and finally requiring at least two "global tracks" (matched SIDC-RICH tracks) in each event. In the output, the reduced raw data were then saved for all events fulfilling these conditions. In this first stage of data reduction, the TPC was not used at all. The output data were first written to disk and then copied and stored on 26 tapes. These tapes were input to the next stage, the postproduction. Altogether, a reduction from 3.7 Tb to 940 Gb of raw data was achieved, i.e. a factor of $\sim$4.

- Postproduction

  In the second stage of "postproduction", the raw data were analysed, staged from tape to disk, and the produced ROOT files were written only to disk. SIDC hits, global tracks, RICH rings, TPC tracks and the event information were stored in ROOT files. The full tracking reconstruction procedure of the TPC was, however, restricted to TPC tracks in the vicinity of global tracks, i.e. of matched SIDC-RICH candidate tracks, allowing for a maximal distance of $\pm$100 mrad in the $\phi$ direction between TPC and global tracks. No additional cuts were applied. After completing the postproduction, the data volume decreased from about 940 Gb of raw data to 70 Gb of ROOT files, i.e. by a factor of nearly 14.

- Postpostproduction

  In the third and last stage of "postpostproduction", the main goal was to minimize the amount of data needed for subsequent electron analysis. Global tracks were now matched to selected TPC electron tracks, defined by applying an appropriate $dE/dx$ cut in the TPC. A further reduction of the data was obtained by saving only SIDC hits with a spacing of 20 mrad around the global track. Finally, only events with at least two fully reconstructed electron tracks with $p_t$>100 MeV/c were kept and stored in a few ROOT files. To run postpostproduction and to analyse the ROOT trees, the complete COOL library was not needed. The only requirements were ROOT and the CERES RCOOLprod libary, compiled with an option to exclude all COOL related functions. The output of the third stage of pre-analysis had a drastic data volume reduction from 70 Gb to 485 Mb, i.e. by a factor of 140. A data sample of only 167000 events was left from the original 8 Million for final analysis.

- Final analysis

  The reduction of the data after three stages of pre-analysis to a volume of only 485 Mb with 167000 events with at least one pair had remarkable consequences. It allowed to perform a final analysis cycle within the extremely short time of 10 min. with as many spectra and different cuts (used as functional parameters) as desired. The main steps of the final analysis were the following:

(i) All possible pairs are created in each event

(ii) A "cut-mask" is defined. With a cut-mask restriction on the full set of pairs, only a subset of pairs is left. A cut mask is defined by requiring each track of a pair to be in the acceptance and to be subject to a number of cuts: minimum number (4) of fitted TPC hits, transverse momentum $p_t>200$ MeV/c, SIDC $dE/dx$ selection, no close electron tracks, Dalitz removal from pairing , and a pair opening angle selection.

(iii) A pair type is defined: $++$, $--$, $+-$ (like-sign, unlike-sign pairs)

(iv) A physics signal is defined: $S = N_{+-} - 2\sqrt{(N_{++} \cdot N_{--})}$

(v) Invariant mass spectra and pair $p_t$ spectra are created.

All these steps will be illustrated in section 3.5 further below.

## 3.3 SIDC Track Reconstruction and Event Multiplicity

### 3.3.1 SIDC Hit Finding

The highly compressed raw data of all detectors stored by the DAQ have to be unpacked. The raw data of the SIDC detectors consist of 6-bit non-linear amplitudes, assigned to the individual *cells* of a two-dimensional matrix of 360 anode readout channels (connected to the azimuthal angle $\phi$) and 256 time samples of the FADC (connected to the radial drift time, i.e. the polar angle $\theta$). The amplitudes are linearized and the pedestals subtracted. Connected regions of cells with non-zero amplitude are grouped into *clusters*. All cells within a cluster of a fixed anode form a *pulse*. An isolated signal of a minimum-ionizing particle typically has pulses of up to 8 time bins and is spread over 1-5 anodes. Pulses of less than 3 cells above threshold are discarded. The centers-of-gravity of the pulses are obtained from Gaussian regression resp. Gaussian fits taking the known widths from a table. Pulses on neighboring anodes connected to the same cluster are merged into a *hit* if their centers-of-gravity differ by less that 1 time bin. The hit coordinate in azimuthal direction is calculated as the center-of-gravity of the contributing pulses.

The SIDC event display (see Fig. 2.4) typically shows an occupancy of several hundred hits. The most prominent quality criterion is the single-hit resolution in $r$ and in $\phi$. This will be discussed in the next section (3.3.2). Beyond that, a good double-hit resolution is also of interest. It limits the level of pile-up in determining the $N_{ch}$-distribution and is also of importance for the rejection of close conversion and Dalitz pairs. The problematics of close double hits will be discussed in the remaining part of this section.

In the 1995/1996 analysis, overlapping double hits were not resolved at all in anode direction, but only in time-bin direction, looking for the minimum between pulses connected to clusters. There was no way to separate pulses so close that only one maximum was found. In the 1999 analysis, a new method was used [40]. One of the criteria to distinguish between one or two and more pulses is the width of the pulses. Based on the width, a decision is made to use a single-Gaussian or double-Gaussian

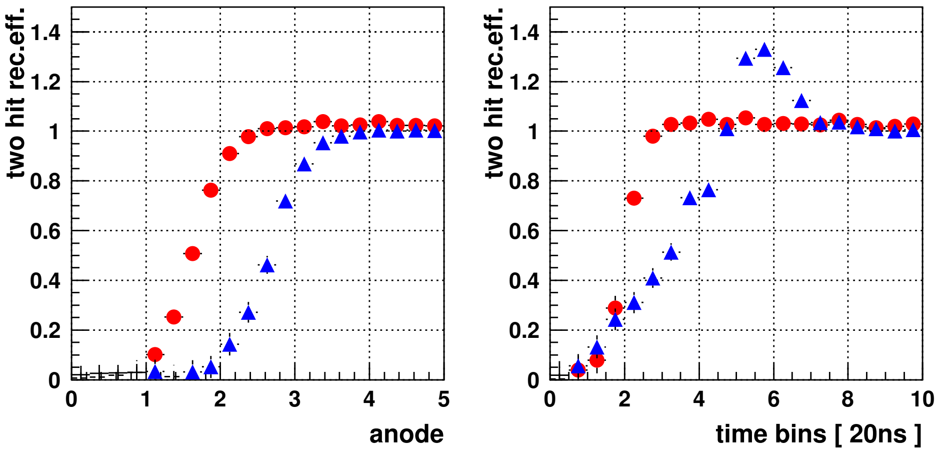


Figure 3.1: *Monte Carlo studies of the SIDC double-hit resolution for the anode- (left side) and the time direction (right side). Circles represent the new and triangles the old hit reconstruction software. Hit reconstruction efficiencies >1 reflect artifical hit splitting of single hits.*

pulse fit method, splitting hits in time-bin and anode direction (see [40] for more about this). A comparison of the two-hit resolution in the old and new software is shown in Fig. 3.1, using Monte-Carlo studies [41]. The principal improvements are obvious, reaching a level of ~300 $\mu m$ (~2.5 mrad) in the $r$- and ~30 mrad in the anode direction.

Unfortunately, the improvements could not fully be explored. Due to certain problems with the FADC readout of the SIDC detectors during the 1999 run, a large number

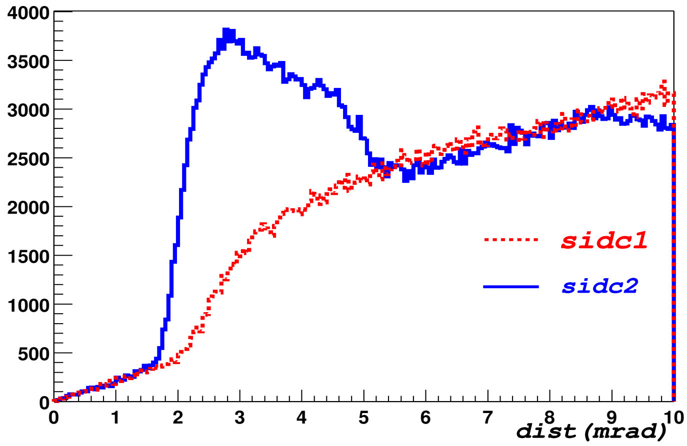


Figure 3.2: *Experimental data on the distance distribution between neighboring hits in SIDC1/2. The distance is determined as $(d\theta^2 + sin^2\theta \cdot d\phi^2)^{1/2}$. SIDC2 shows a large enhancement due to artifical hit splitting of single pulses.*

of pulses (in particular in SIDC2) had non-standard pulse shapes with missing time bins etc. [42], creating much more artifical hit splitting than seen in the Monte Carlo simulations. This is illustrated by data in Fig. 3.2, showing a large number of additional hits for distances of a few mrad.

The amplitude of a hit is determined as the sum of all cell amplitudes connected to the hit. This is an extremely useful quantity, directly connected to the $dE/dx$ of a traversing particle. The pulse height distribution of the hits in the two SIDC detectors is shown in Fig. 3.3. The tail at very low values of $dE/dx$ again reflects the effects of artifical hit splitting.

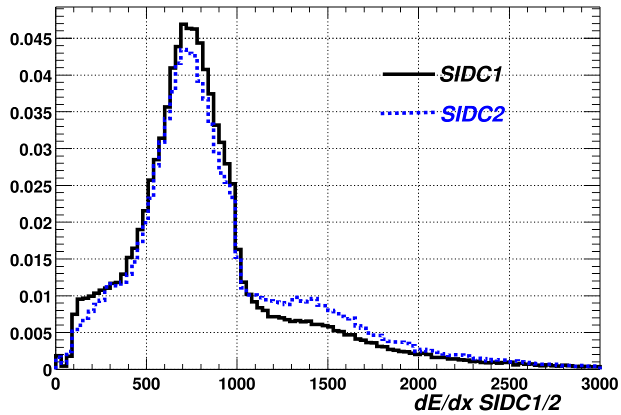


Figure 3.3: *Pulse height distribution of hits in SIDC1 and SIDC2. The excess on the low tail is due to hit splitting, the excess an the high tail to double-$dE/dx$ from close low-mass electron pairs.*

As detailed in subsection 3.5.2 below, the main use of the $dE/dx$ information from the two SIDC detectors in the electron analysis is the identification and then rejection of close conversion and Dalitz pairs, using either two resolved close hits with single $dE/dx$ each or one unresolved hit with double $dE/dx$. Unfortunately, the artifical hit splitting problem, visible already in the Monte Carlo studies and much more so in real data, essentially prohibits the use of resolved double hits up to at least 5 mrad. Instead, as was already done in the 1995/1996 analysis, all hits within a circular window around a given track are summed, thereby automatically resumming the pulses of split hits. In the present analysis, the window was opened from 5 mrad (in 1995/96) to 10 mrad to obtain a particularly high efficiency for rejection. Genuine close tracks up to an opening angle of 10 mrad appear than as double $dE/dx$ information, free from the problem of hit splitting. If this is done for both SIDC detectors in a correlated way (compare Fig. 3.37 in subsection 3.5.2), the rejection quality becomes far superior to anything which could be obtained from two resolved close hits.

### 3.3.2 Track and Vertex Reconstruction

For the event-by-event reconstruction, all hits within the combined acceptance of the two SIDC detectors are used. When the hits are found and their positions have been transformed into three-dimensional laboratory coordinates, the next step is to combine them into tracks and then use all the tracks of the event to find the interaction vertex position. The event vertex is the point from which almost all particles produced in the nuclear collision originate. For the vertex reconstruction, the "Robust Vertex Fit Procedure" was used [43]. The hits are combined into straight track segments, and the weighted sum of all their projected distances to an assumed vertex position is calculated. In an iteration, this center-of-gravity becomes the new vertex and each segment gets a new weight, acording to the deviation from the mean value in the step before. Five iterations are sufficient for convergence. The resulting distribution of vertex positions along the $z$-axis is shown in Fig. 3.4. The individual target disks are resolved with an $rms$ resolution of ~560 $\mu m$.

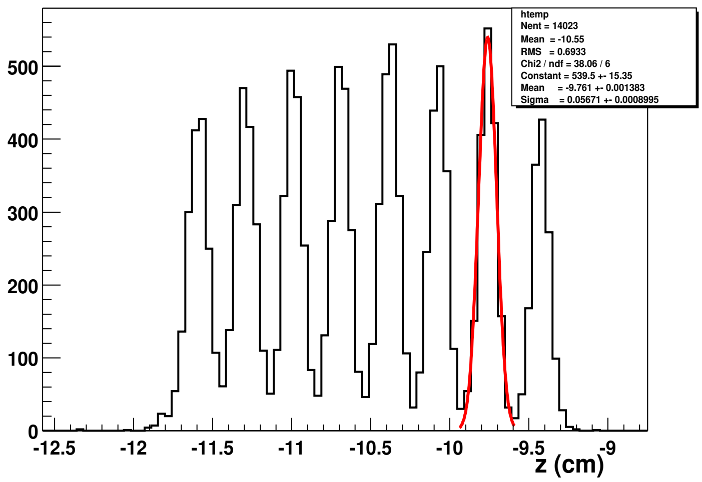


Figure 3.4: *Reconstructed vertex positions along the beam axis. The peaks determine the positions of the 8 $Au$-target disks with a resolution of $\sigma_z$~560 $\mu m$.*

The target region is free of a magnetic field and therefore the SIDC tracks are straight lines. SIDC tracks for each event are reconstructed in two steps:

- Candidate track segments are created by connecting all SIDC2 hits to the vertex point.
- The expected positions in SIDC1 are calculated by the 1996 algorithm searching for the closest hit in SIDC1 for each track. If a hit is found in a window of $\pm 3\sigma_{match}$ both in the $r$- and the $\phi$ direction, the SIDC track segment is accepted and defines, together with the hit from SIDC1, a SIDC track. The final tracks are then constructed in polar coordinates $\theta$ and $\phi$, using the average of the two hits.

The matching distributions of the SIDC1/2 detectors from the vertex point are shown in Fig. 3.5. They are wider in 1999 compared to 1995/96 due to the SIDC defects mentioned before. The $rms$ value in the $r$ direction is 115 $\mu m$; a matching window of $\pm$300 $\mu m$ was used. In the $\phi$ direction, two components exist, one with an $rms$ value of 4 mrad connected to multi-anode hits, and a wider one connected to single-anode hits; therefore, a matching window of ±20 mrad had to be used. The matching width

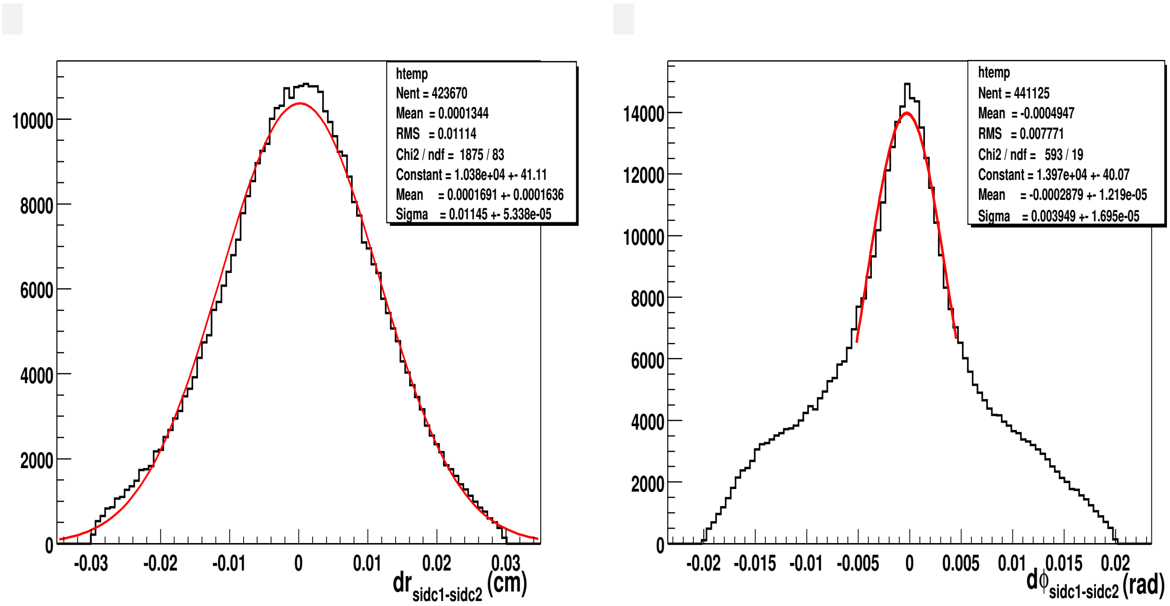


Figure 3.5: *Matching distributions of SIDC1 and SIDC2 in 1999, with radial and azimuthal resolution values of $\sigma_r$=115 $\mu m$ and $\sigma_\phi$=4 mrad as obtained from a fit (red line). The tails in the azimuthal distribution are due to single anode hits, increasing $\sigma_\phi$ to >4 mrad.*

in the $r$ direction corresponds to a value of 81 $\mu m$ for a single detector (instead of the expected ∼30 $\mu m$), and to a value of 57 $\mu m$ for the track resolution, resulting from the averaging of the SIDC1/2 coordinates; this is equivalent to about 0.5 mrad in the $\theta$ direction.

### 3.3.3 Event Multiplicity

The centrality of the collision is a fundamental parameter in the study of heavy-ion reactions. It determines, for a given beam energy, the participant volume and the energy density of the fireball. The quantities which are used for estimation of the centrality are charged particle multiplicity ($N_{ch}$), transverse energy ($E_T$), missing forward energy etc. In the CERES experiment, the centrality is estimated by determining the charged particle multiplicity with the SIDC detectors over one unit of pseudorapidity in the range $2<\eta<3$. The measured multiplicity needs a number of corrections. Different from 1995/96, where the corrections were determined by Monte Carlo simulations, the procedure used in 1999 is based on data as much as possible to increase the reliability. Corrections are required for the following items:

- detector efficiencies including matching losses,
- ghost tracks from artifical hit splitting of single hits,
- pile-up losses within the double-track resolution,

- contributions from $\delta$ electrons.

The starting situation is the raw multiplicity distribution $N_{ch}$ of the charged tracks measured over the full SIDC acceptance of 1.95<$\eta$<3.21, i.e. over an interval $\Delta\eta$=1.26 (FWHM). A representative example of such raw data is shown in Fig. 3.6. Following a cut 2.0<$\eta$<3.0 in rapidity space, the 4 classes of corrections are applied as follows:

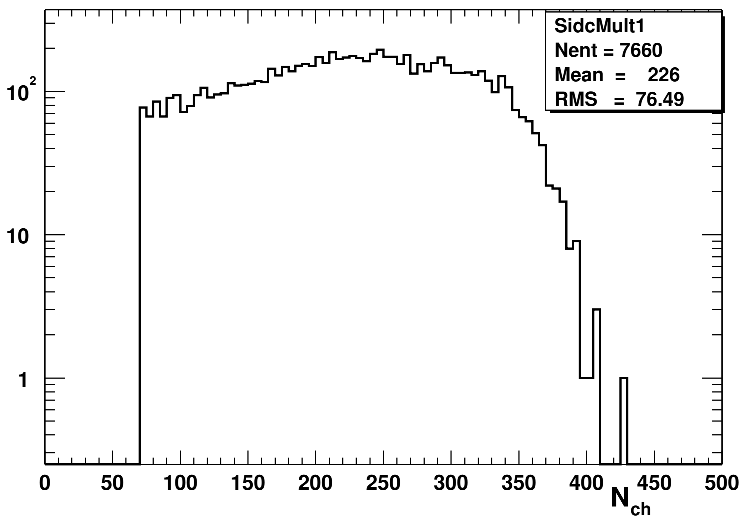


Figure 3.6: *Raw multiplicity distribution of SIDC tracks in the rapidity interval 1.95<$\eta$<3.21.*

(i) An upward correction of 1/0.76 for efficiency: The efficiency of SIDC tracks was studied using high-$p_t$ tracks from a high-efficiency part of the TPC (a particular azimuthal sector with $\sim$ 90%). The TPC tracks were matched to the vertex, and the SIDC track efficiency associated with this sector was determined as the probability that these tracks were also found in the SIDC system. The efficiency was then extrapolated to the full azimuth by correcting for the known defects of the SIDC system around the azimuthal direction. The final efficiency value obtained is only 76% [44]. The number can roughly be understood as due to three sources of losses: 95% from dead anodes, 94% from asymmetrical matching between SIDC1/2 in $r$ direction (a SIDC detector intercalibration change required for the electron analysis shifted the center of the matching distribution shown in Fig. 3.5 away from 0), and the rest probably from matching losses in the non-Gaussian tails of the matching distribution (invisible in Fig. 3.5 because of the cuts).

(ii) A downward correction of 1/1.11 for ghost tracks: As mentioned before, the SIDC software has the unfortunate property to split single hits. To determine the probability for ghost tracks due to hit splitting, the angular distance distribution between a fixed track and any other one in a circular window was investigated. Fig. 3.7 shows the results for data tracks. In the small distance region below 3 mrad, the ghost tracks appear as a pronounced narrow peak. The probability of tracks associated with the

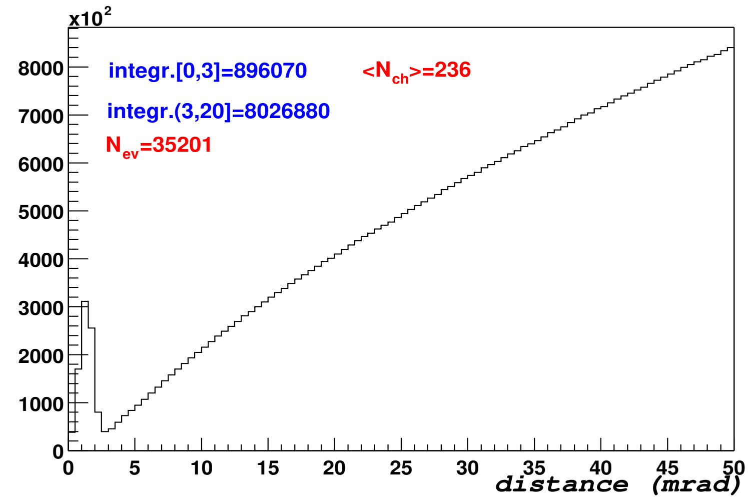


Figure 3.7: *Experimental data on the distance distribution between neighboring tracks in the SIDC1/2 detectors.*

peak can be calculated from

$$P = \frac{\int_0^3 (\frac{dN}{d\theta})_{peak} d\theta}{N_{ev} \cdot \langle N_{ch} \rangle} \tag{3.1}$$

One finds a value of $\sim$11$\%$ as an average over the whole multiplicity distribution. Subdividing the distribution into several bins, the number is, not surprisingly, found to be independent of $dN_{ch}/d\eta$ to within $1\%$. Conversely, using Monte Carlo tracks, the

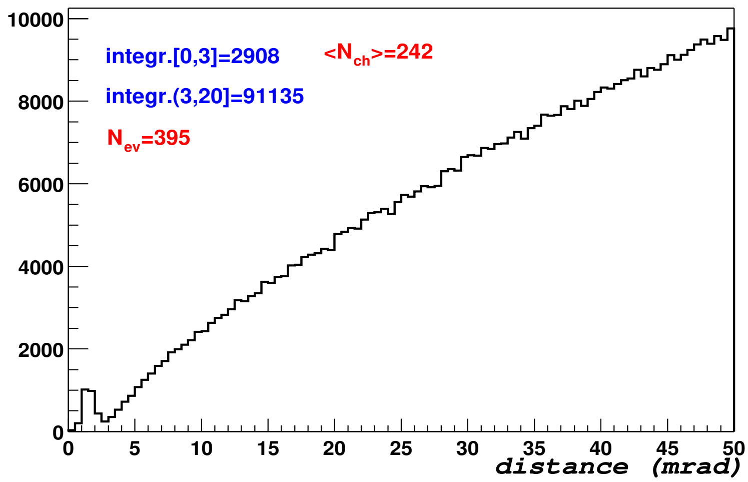


Figure 3.8: *Monte Carlo simulations of the distance distribution between neighboring tracks in the SIDC1/2 detectors.*

probability for ghost tracks is much smaller, only 2.9 $\%$ (Fig. 3.8), consistent with much smaller artificial hit splitting for the idealized SIDC pulses (see section 3.31)

(iii) An upward correction of 1/0.97 for pile-up losses: Two tracks overlapping within the matching window of the SIDC1/2 system (which is somewhat wider than the double track resolution, compare sections 3.31 and 3.32) are reconstructed as only one track. Corrections for these "pile-up" losses were studied using Monte Carlo simulations with pion tracks. In regions of high hit density, i.e. at small polar angles or at high multiplicities, one expects higher probabilities for pile up, and therefore smaller track efficiencies. The results of the simulations vs. $dN_{ch}/d\eta$ are shown in Fig. 3.9 with a normalization such that the relative efficiency is set to 100% at 0 multiplicity. The effect is rather weak, corresponding to only ∼3.5% for the averaged distribution. A similar value can be obtained from a simple estimate based on the SIDC occupancy and the size of the matching window, without resorting to any MC code.

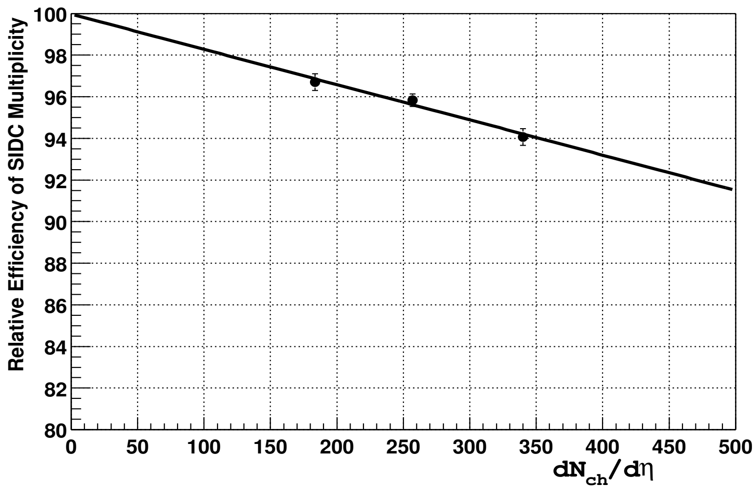


Figure 3.9: *Monte Carlo results on the relative SIDC1/2 track efficiency vs. charged particle multiplicity density.*

(iv) A downward correction by 3 tracks for $\delta$-electrons: Beam particles traversing the target disks create $\delta$-electrons in all disks preceding the one where the nuclear interaction takes place. The information on the total number of $\delta$-electron tracks seen by the SIDC1/2 system could, in principle, be obtained by measuring the expected increase of the charged multiplicity as a function of the target disk number (in the direction upstream to downstream), selecting always the same rapidity window. Unfortunately, the effect is too small to be observable within the systematical errors of the procedure (the angular region to be selected varies from disk to disk); all attempts in this direction have failed so far, including this work. Instead, a Monte Carlo sample of $\delta$-electrons was tracked through the SIDC system. The results are shown in Fig. 3.10. A number of hits, about 24, are created in the two detectors, but most of them do not align to tracks within the matching window together with the interaction vertex, due to geometrical mismatch and multiple scattering ($\delta$-electrons are very soft). Only about 3 tracks are reconstructed (by definition independent of $dN_{ch}/d\eta$) which have to be subtracted from the multiplicity distribution.

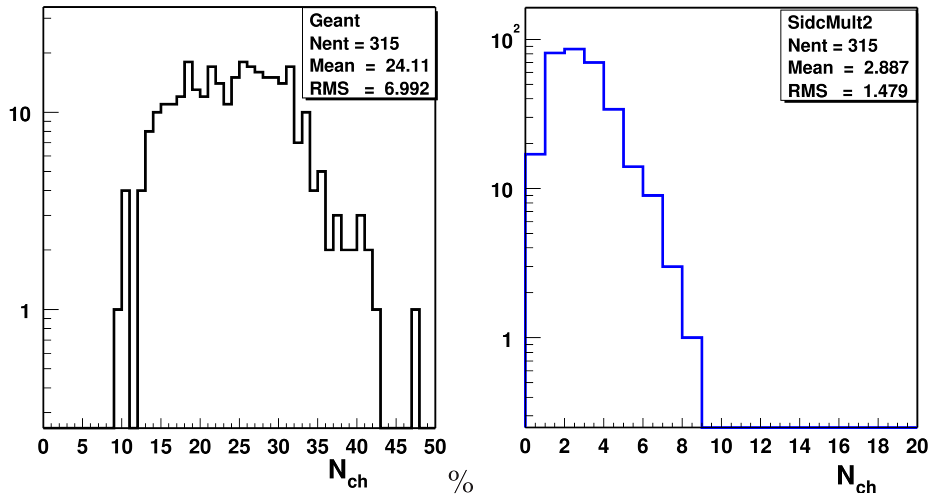


Figure 3.10: *MC simulations of $\delta$-electron hits (left side) and of SIDC tracks reconstructed from these hits (right side). Since $\delta$-electrons do not point to the interaction vertex, they are efficiently suppressed to a level of $\sim$ 3 tracks per event.*

The final distribution of the charged multiplicity density, including all corrections, is shown in Fig. 3.11. The shape looks rather unusual, due to a gliding cut at low multi-

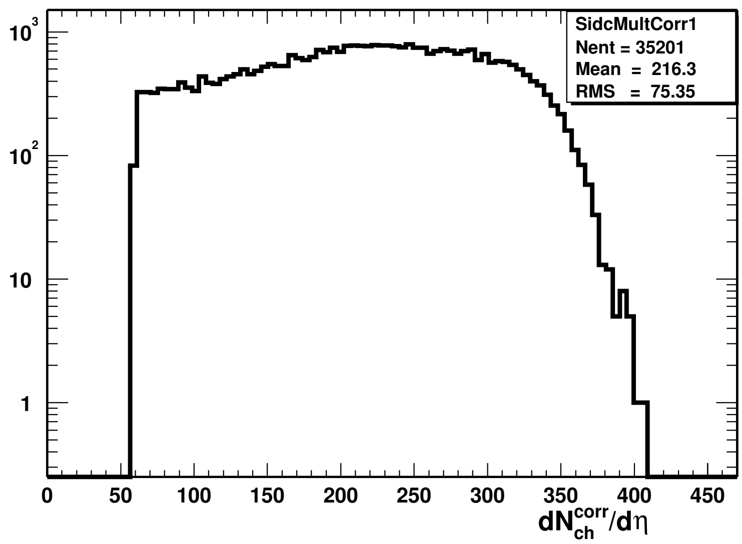


Figure 3.11: *Final corrected distribution of the charged particle multiplicity density in the SIDC system.*

plicities in the trigger selecting 30 % of the geometrical cross section. The mean number of the $dN_{ch}^{corr}/d\eta$ distribution, $\langle dN_{ch}/d\eta\rangle$=216, is therefore larger then one would expect for 40 compared to 160 AGeV ($\sim$250). To confirm consistence of the results with other experiments, it is more appropriate to compare the upper tails of the distributions, corresponding to a well defined central-collision selection. This has been done for the upper 7% fraction within the CERES acceptance 2.1<$\eta$<2.6, comparing to the results from NA49. The multiplicity density for identified hadrons from NA49 for this selection is shown in table 3.1 [45, 46], summing up to a total number of 292. The CERES value derived from Fig. 3.11 is 313, which has to be downward corrected for the con-

| | |
|---|---|
| $\pi^+ + \pi^-$ | 107 + 107 |
| $K^+ + K^-$ | 20 + 8 |
| $p + \overline{p}$ | 48 + ~2 |
| Total sum | 292 |

Table 3.1: *Central rapidity densities of identified hadrons from NA49 for Pb+Pb at 40 AGeV [45, 46] for the upper 7% of the geometrical cross section.*

tribution from 1.7 conversion tracks and 2.6 Dalitz tracks to $dN^{corr}_{had}/d\eta$=309. The two experiments agree to within 6%, i.e. well within the systematic uncertainties of 5% each.

The mean number of $\langle dN_{ch}/d\eta \rangle$=216 will be required in chapter 5 for normalization of the electron pair data and comparison to the hadronic decay generator.

## 3.4 Electron Track Reconstruction

### 3.4.1 RICH Clean-up and Hit Finding

The raw data of the two RICH detectors consist of induced-signal amplitudes assigned to the individual pads (~ 50000 each) of the checkerboard-like two-dimensional pad arrays. In the first step, all adjacent pads with one identical coordinate and with amplitudes above a readout threshold are connected to *clusters* (edge-to-edge connections alone are insufficient). In the such created list of clusters, background from different sources is removed by a procedure named "clean-up" to minimize the number of fake ring candidates. Although there is an unavoidable loss of efficiency due to removing also some real UV-photon hits, the clean-up procedure has been very carefully tuned to find the best compromise [47]. Clusters with the following features are removed:

1) large clusters of pads originating from highly ionizing particles traversing the detector plane which
   - are very big (> 200 pads)
   - look like an ionization track (long and thin, mostly at an oblique angle)
   - have many saturated pads in the cluster (>6)
2) crater-like circular clusters
3) small-amplitude clusters over extended regions from electronic noise or pedestal fluctuations
4) small clusters with <3 pads, mostly from electronic noise.

The remarkable improvements which can be obtained by the clean-up procedure are illustrated by a sample event in Fig. 3.12.

In the next and last step, hits are searched for by determining local maxima in a cluster. If more than one local maximum is found, the cluster is split. Each local maximum and the surrounding pads are identified as a UV-photon *hit* in the RICH's. Hit centers are calculated as the centers-of-gravity of the associated pads.

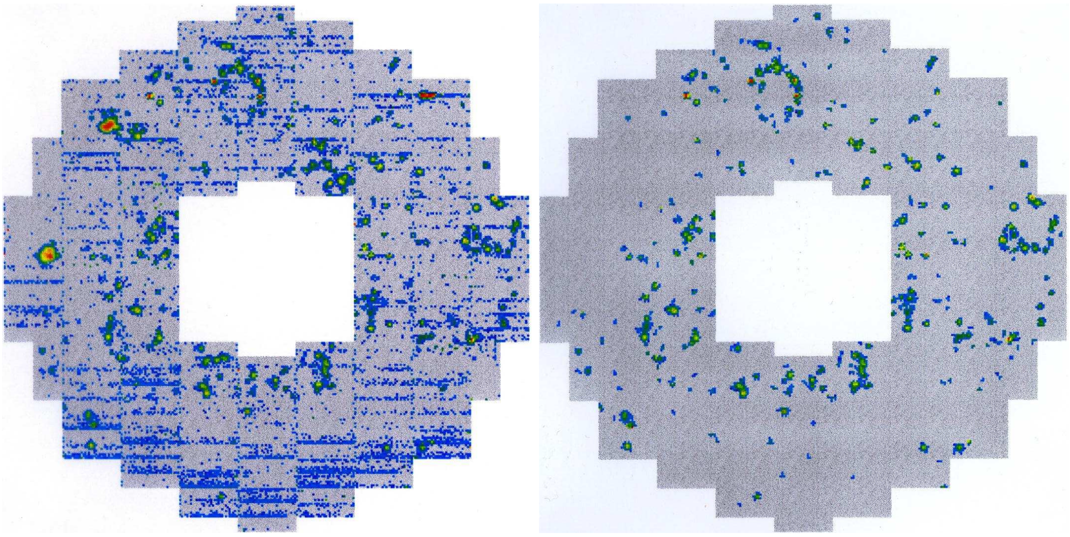

Figure 3.12: *RICH event with raw data (left) and after clean-up procedure (right). The common-noise structure seen in the left part exists only in a small fraction of the events; it is shown here to demonstrate the effectiveness of the clean-up.*

### 3.4.2 RICH Ring Reconstruction

RICH detectors require an additional step of pattern recognition: to combine hits to rings. A great simplification arises in the case of the electron analysis: only rings with asymptotic radius $R_\infty = f/\gamma_{th}$ produced by electrons and positrons need to be searched for. The ring reconstruction procedure is divided into two parts, a two-step point-to-ring Hough transformation with a search for candidate rings, and a robust ring-fit procedure applied to the candidate rings.

Due to the new setup in 1999, there was no more need for a B-field between the RICH's. The absence of the field allowed to use the two RICH's in a combined mode, treating them as one single unit. The point-to-ring Hough transformation then becomes a "double-Hough" procedure. In the first step, pads from both RICH's are transformed into the same coordinate system, using the coordinate system of RICH1, which has the larger acceptance, as the base system [48]. When the new system of pads is defined, the double-Hough procedure is employed in the same way as the single-Hough procedure used before [49]. Each pad of a UV-photon hit forms the center of a ring with nominal asymptotic radius. The "Hough array" which has the same cells and dimension as the data field, contains the image of all these rings, each original pad and associated ring contributing with the same weight ("digital Hough transformation").

The "Hough amplitude" is defined as the hit multiplicity of each cell in the Hough array. A ring candidate shows up as a peak in the Hough array, reflecting the intersection of a multitude of rings in the center of the electron ring in the original pad plane.

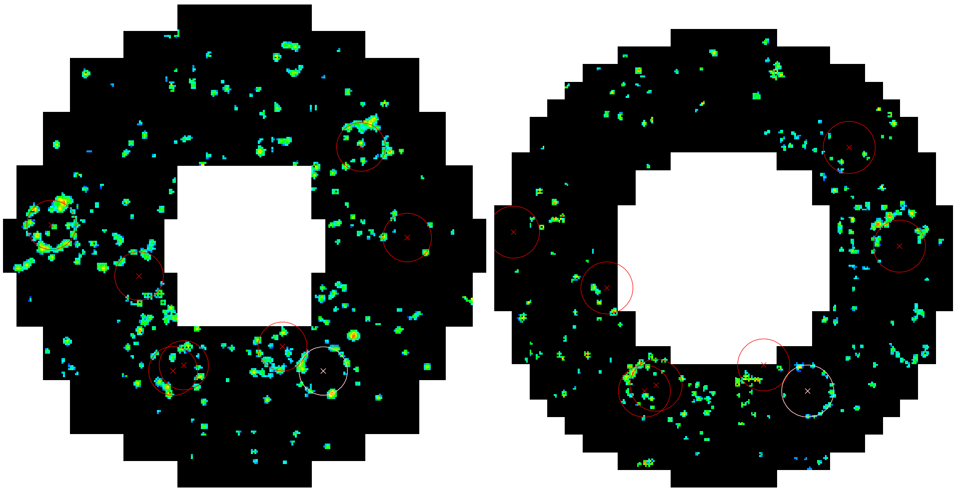

Figure 3.13: *RICH1 and RICH2 event display for a sample event, showing fitted candidate rings (presumably from $\gamma$-conversion or $\pi^0$ Dalitz pairs). The white fitted ring shows the example of a candidate pair aligning in the 2 RICH detectors and also matching to a track in the preceding SDD detectors.*

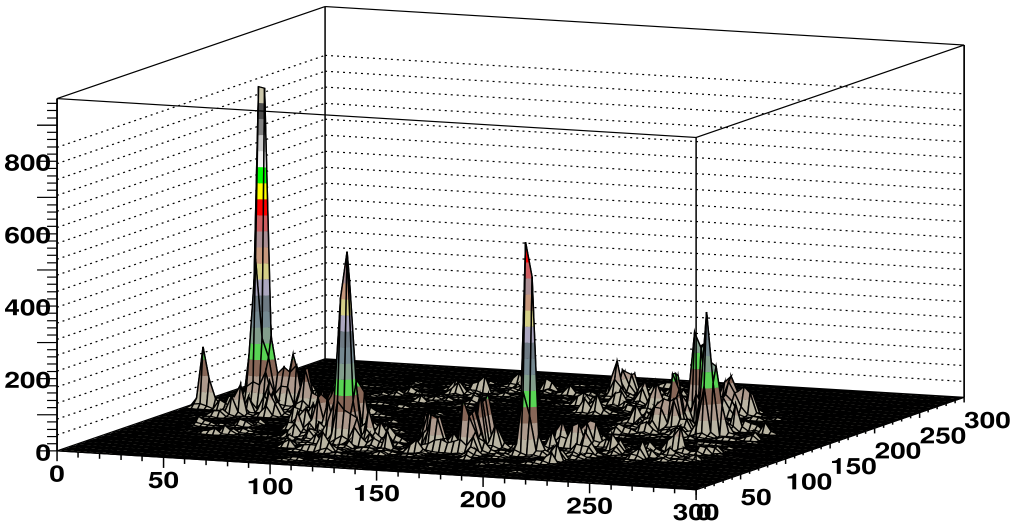


Figure 3.14: *Hough array, connected by a two-step point-to-ring Hough transformation to the event shown in Fig. 3.13. Several ring candidates are seen as pronounced peaks.*

Fake rings, due to ring-like random arrangements of photon-(or background) hits and usually associated with a smaller-than-average number of hits, show up as other local maxima in the Hough array. A second, non-linear Hough transformation is therefore added which assigns relative weights to the cells in the Hough array such that each hit counts most for its most favorable ring-center [49]. This additional step results in a larger gap between the amplitudes of real and fake rings and thus improves the discrimination. At the end, a list of ring candidates with double-Hough amplitudes above a chosen threshold is defined.

In the second part, the final x- and y- coordinates of the centers of the candidate rings are determined by a robust $\chi^2$ fit, keeping the radius fixed at the known value of the asymptotic radius. The fitting algorithm is described in [50, 17]. Minimization is done of a modified $\chi^2$ where the fit-potential varies in a Gaussian way (instead of quadratically) with the distance to the minimum. In the 1999 case of combined RICH1/RICH2 analysis, the fit applies of course simultaneously to the combined hits from both detectors. The information obtained at the end of this part consists of the number of fitted rings in the event and, for each ring, the x- and y- coordinates of the center, the total number of hits and the total analog amplitude summed over the hits, where the summation is done in a mask of $\pm 6$ mrad around the ring circumference.

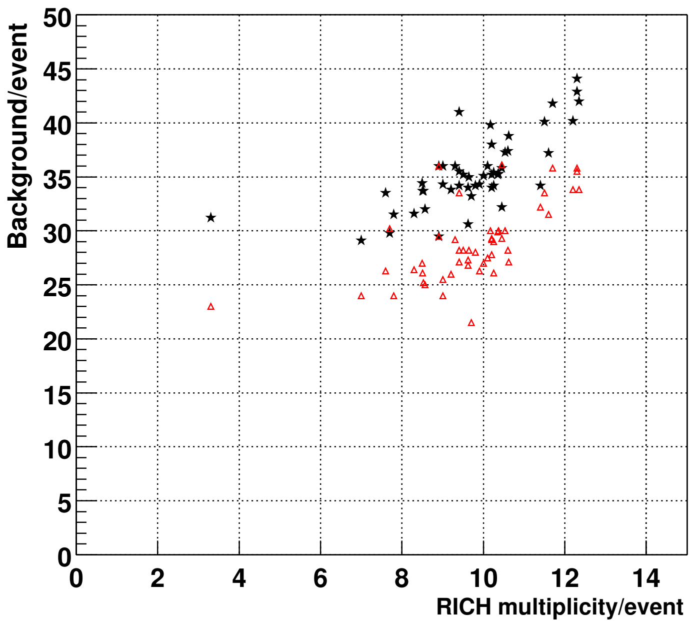


Figure 3.15: *Correlation of RICH candidate rings and (fake-ring) background tracks identified by the TPC for the individual runs of the 1999 data taking period. Black stars: positive particles; red triangles: negative particles. The pad threshold is set to 3.*

Fig 3.13 and 3.14 illustrate the two-part procedure for a sample event. A number of peaks are found in the Hough array (Fig. 3.14), which can be correlated 1:1 with the rings seen and fitted in the event display of the 2 RICH detectors (Fig. 3.13). Only the ring coded "white" has a satisfactory visual appearance in both detectors and also matches to a track in the preceding SDD detectors; the rest is either fake or an extremely soft conversion pair (highest peak in Fig. 3.14).

In the remaining part of this section, the choice of the double-Hough transformation parameters for the electron production and some performance figures for the combined rings in the double-RICH system will be discussed.

To reduce the number of candidate rings and, at the same time, to keep a high efficiency, the thresholds for the double-Hough amplitude and for the pad amplitude have to be optimized. Before optimization, the number of RICH candidate rings varied from 10-25/event and was correlated with background-(fake-ring) tracks, defined by a $dE/dx$-selection of $\pi$-tracks in the TPC (see subsection 3.4.5). Such a correlation, containing the run-to-run variations of candidate rings and background tracks during the very instable 1999 running period for a pad threshold of 3 is shown in Fig. 3.15. With this parameter choice, electron production would have been ineffective.

The optimization of the parameter-pair double-Hough amplitude and pad threshold was done using an overlay Monte Carlo mode. Idealized high-$p_t$ electron tracks were superposed onto real events, allowing the determination of the absolute track efficiency, while the number of candidate rings was directly obtained from the data. The results of this study as a function of the pad amplitude cut for a fixed double-Hough amplitude cut of $\geq$150 are shown in Fig. 3.16. A similar dynamical range for both quantities is found as a function of Hough amplitude in the range 150-200 for a fixed pad threshold of $\geq$7 [48]. The result of the optimization is the choice of a minimum double-Hough amplitude of 150 and a minimum pad amplitude of 7, corresponding to a RICH track efficiency of 94% and to about 4 candidates/event. Matching these (mostly fake-) candidate rings to SIDC tracks led, together with the other cuts and conditions, to the reduction of the number of events by about a factor of 4 in the first stage of the electron production as discussed in section 3.2.

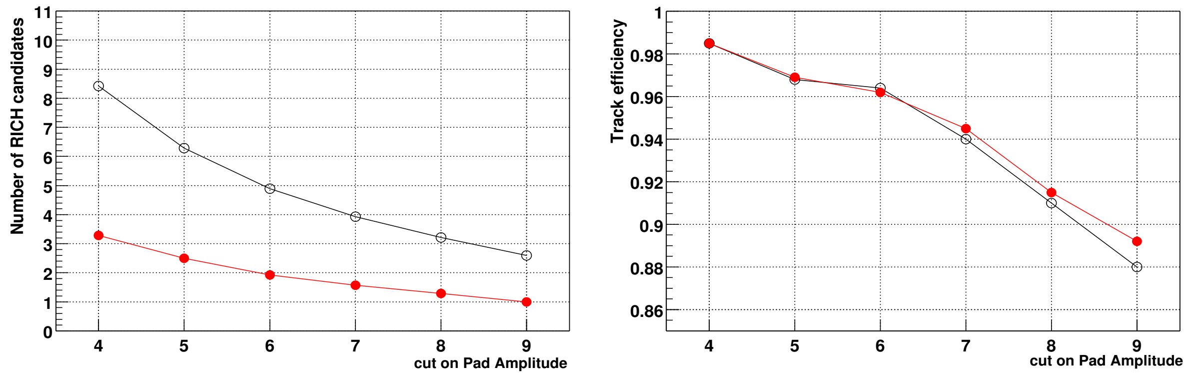


Figure 3.16: *RICH multiplicity and track efficiency as a function of the pad amplitude cut for full ring acceptance (red full circles) and for total acceptance (open black circles) from overlay MC [48]. The double-Hough amplitude cut is set to $\geq$150.*

The advantages of the combined use of RICH1 and RICH2 in the 1999 analysis compared to the separate use in 1995/96 can be summarized as follows:

(i) Improved ring reconstruction efficiency: In the previous analysis, a cut of >5 hits on the Poissonian hit distributions (with an average of about 10 each) was used in both RICH's separately resulting, together with other losses, in ring reconstruction efficiencies of 81% for RICH1 and 86% for RICH2, i.e. a RICH track efficiency of only 70% (see Fig. 3.17). In the combined mode, the average of the distribution doubles to

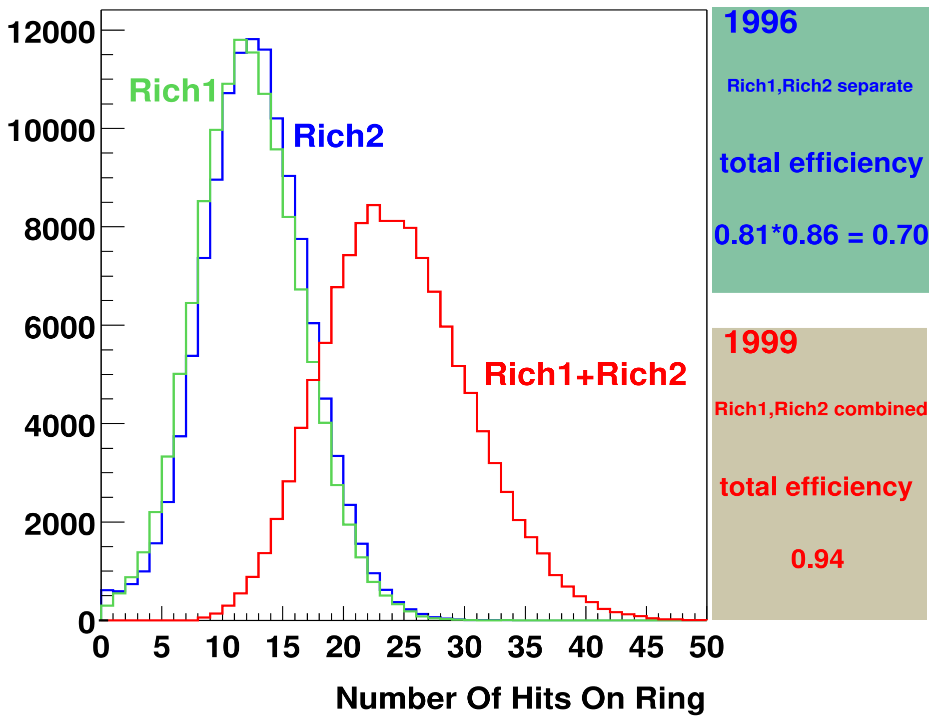


Figure 3.17: *UV-photon hit distributions for identified rings in the separate RICH1/RICH2 system as used in 1995/96 compared to the combined RICH system in 1999. The distribution for 1999 is not corrected for a contribution from background hits (∼4).*

about 20 hits (24-4 from background), but the safer cut of >10 hits on the combined distribution still results in an improved value for the track efficiency of 94% (for high-$p_t$ tracks; somewhat lower for realistic sources, see chapter 4). In addition, the losses of track efficiency with multiplicity are less steep compared to the separate uses of the RICH's (see subsection 4.2.3 below).

(ii) Improved ring-center resolution: In the 1995/96 analysis, ring-center resolution values of 1.3 and 0.6 mrad were obtained for RICH1 and RICH2, resp., including the influence of background hits and the ill-understood deterioration in RICH1 compared to MC. The combined use of the two RICH's should result in an overall ring-center resolution of 0.5 mrad, given a perfect intercalibration of the RICH's. Unfortunately, no simple way was found to verify this number in the 1999 data, since the matching distributions with other detectors are too wide to be sensitive (see section 3.4.5).

iii) Improved ability of separating rings: Extensive comparative MC studies done in the early phase of this work have shown double-ring separation values of 7.7 mrad (50 % probability value) for the combined RICH use [48], while 11 mrad for RICH1 and 9 mrad for RICH2 were obtained for the separate use. In practice, however, this improvement has not been relevant for the present analysis, since the total analogue sum amplitude turned out to be the more useful quantity for the recognition of close double rings.

In summary, the combined use of the RICH1/RICH2 system in the 1999 electron pair analysis has proven to be extremely beneficial.

### 3.4.3 TPC Hit Finding

As for the other detectors, the first step in the offline analysis is to unpack the highly compressed raw data of the TPC. As mentioned before, the TPC contains a total of $48 \cdot 16 \cdot 20 = 15360$ readout channels. The raw data of each channel consist of linear amplitudes from an 8-bit ADC in 256 time bins per channel, equivalent to amplitude information from a total of $\sim$4 million pixels. Hit finding in the TPC proceeds in the following steps:

- Clean-up procedure:

  The clean-up algorithm was tuned to minimize background from different sources while maintaining maximal efficiency. It is an event-by-event procedure removing all electronics defects, noise and pedestal fluctuations of the individual read out channels. In the 1999 data analysis suffering from the very instable TPC operation, the clean-up also detects and eliminates the (permanently changing) regions of faulty electronic readout; indeed, only two chambers (number 0 and 1) were really stable (see also section 4.1.3).

- Hit finding:

  The hit reconstruction software converts raw pixel data into reconstructed space points. *Clusters* are defined as connected pixel structures with at least one coordinate, pad or time-bin, being the same (no edge-to-edge connections). For each of the 20 planes going into pad direction ($16 \times 48$ pads in azimuthal direction), the slope in time direction is defined. The maximum in time direction is defined as the point where the slope changes sign. All neighboring pixels belonging to the same cluster are flagged. The centroid of the cluster is extracted as the maximum of a Gaussian regression by calculating the mean and the sigma. No minimum cluster size in pad- or time direction is required for the hit finder. The criteria to distinguish between one and two hit clusters are the widths of the Gaussian fit of the hit in pad ($\sigma_P$) and time direction ($\sigma_t$). If $\sigma = \sqrt{(\sigma_P^2 + \sigma_t^2)}/\sqrt{2} < 1.25$, the result is accepted as a one hit cluster. If $\sigma > 1.25$, then a double Gaussian fit could have been used to split a double-hit cluster into two hits; for reasons of computing time, this was not done.

  After the hits are defined, the next stage is a quality test of these hits. The quality is defined using $\sigma_p$ and $\sigma_t$. Only hits which satisfy the condition $\sigma = |0.707 \cdot \sqrt{\sigma_P^2 + \sigma_t^2} - 1| <$ 0.35 where $\sigma_P$ >0.2 and hit amplitude >50, are accepted as hit candidates for track reconstruction.

Occupancy and hit density are quite uniform over the acceptance in the polar angular range $\theta$= 8$^o$-15$^o$.

- Transformation from (time,pad,plane) to (x,y,z) coordinates:

  A particularly difficult task is the transformation from the (time,pad,plane)- to the (x,y,z) coordinate system. It requires the knowledge both of the complete geometry of the chamber and of the drift velocity in each space point of the TPC, which itself depends on the $\vec{E}$- and $\vec{B}$-field in each point

$$v_d = \mu \frac{1}{1 + (\mu|B|)^2} (\vec{E} + \mu(\vec{E} \times \vec{B}) + \mu^2(\vec{E} \cdot \vec{B})\vec{B}) \quad (3.2)$$

and the detailed gas properties [51]. The 1999 analysis was based on a quick zero-order approach to solve all the associated difficulties. The electric field was

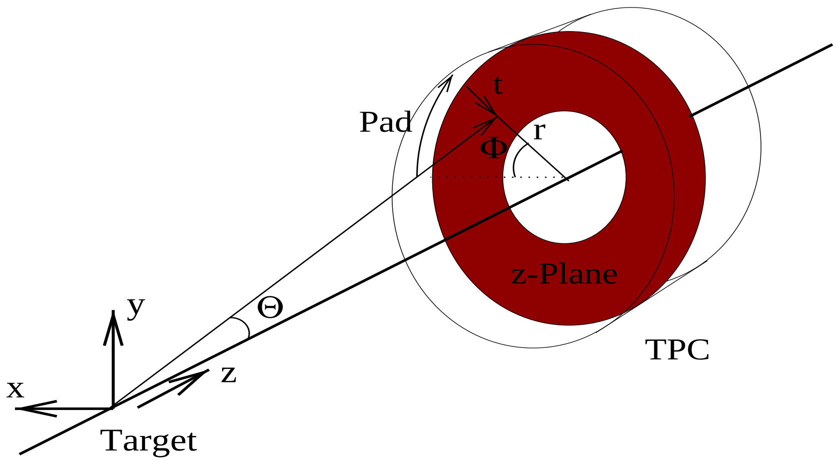


Figure 3.18: *Association of the TPC coordinates (time, pad, plane) with (x,y,z).*

calculated by using the finite-element "Mafia" package. Corrections are done in each consecutive plane along the z-direction using data at zero magnetic field. In the first step, the assumption is made that the tracks are straight in the 10 middle planes. Then, a linear fit is made, and the distribution of the values $\Delta r$ vs. $r$ for each of the remaining planes is used to correct the field, where the $\Delta r$ are the measured distances of the hits from the extrapolated straight track. In the next step, by using the first order approximation $v_d = \mu \cdot E$ of eq.(3.2) and assuming that $\mu$ is locally constant, the electric field is simply corrected by $E_{corr} = (1+f^{'}) \cdot E$, where $f^{'} = \Delta v_d / v_d = \Delta E/E$ [52]. A more refined procedure is underway in connection with the analysis of the data taken in 2000.

The monitoring of the gas properties allowed to correct for observed variations in the $Ne$-$CO_2$ mixture leading to changes in the drift velocity. The atmospheric pressure variation that also leads to drift velocity variations, was also taken into account. The correction factors were obtained from the drift velocity monitor (Goofie).

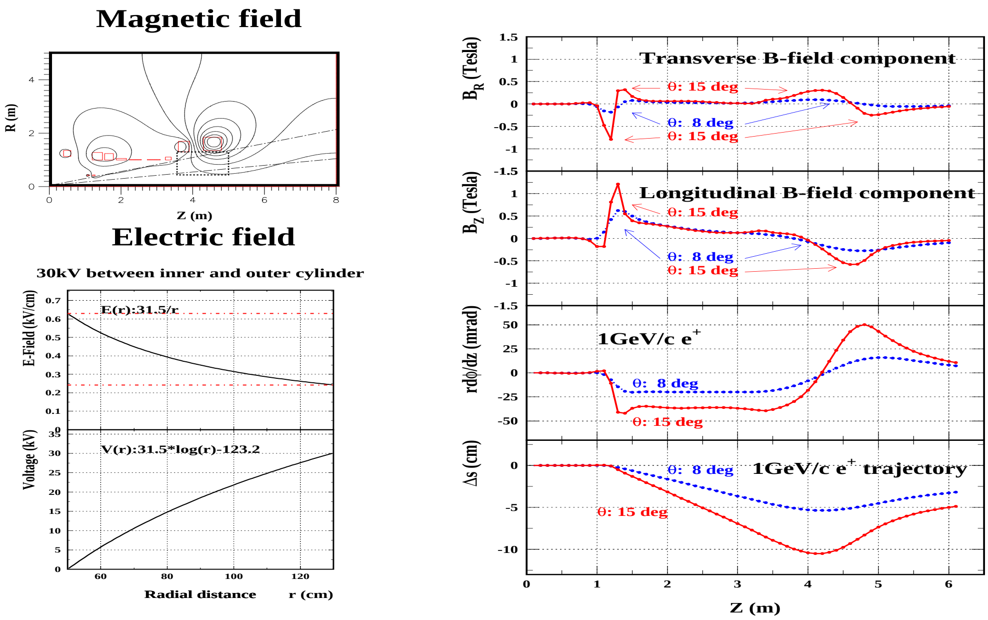


Figure 3.19: *The upper left panel shows the magnetic field lines and the active volume of the TPC (dotted line). The right panel indicates the components of the magnetic field (transverse and longitudinal) for different polar angles $\theta$ and for momentum tracks of 1 GeV/c [53]. It also shows that this magnetic-field configuration produces a deflection in azimuthal direction $\phi$, the precise measurement of which is used for determination of the momentum of the particles. The lower left panel contains the electric field and the potential in the TPC as a function of radius. Note that the magnetic field shown in this figure also contains the original localized field between the two RICH-detectors; for 1999 running, this part was actually switched-off as described in section 2.1.*

- Amplitude calibration:

  A calibration procedure is designed to equalize the electronics response as well as variations in gas gain within the chambers by introducing a relative gain constant. The gain corrections were applied for each individual cathode readout pad, with the correction values determined from zero-field data. Also the electron attachment corrections were taken into account. After the gain calibration, each pad has the proper amplitude. In a later stage of the analysis, the charge measurements of each hit are used to calculate the average energy loss of a particle along a track with the truncated-mean method.

### 3.4.4 TPC Track Reconstruction

As for the hit finding, a number of different points need to be discussed, relating to track fitting and momentum determination, momentum resolution, particle identification with $dE/dx$ and global alignment.

- Track finding, track fitting and momentum determination

Reconstructed hits which pass the quality criteria have to be linked to form particle tracks. To be efficient in the tracking analysis, "corridors" in three dimensional space are defined to limit the number of hits. They are chosen to be $\Delta\phi$=20$^o$ in the $\phi$-direction, while the slices in $\theta$ are only $\Delta\theta$ = 1$^o$, since to zero order there is no deflection in the polar angle $\theta$ of a track (see Fig. 3.19). Track finding begins from candidate hits with a $z$-position in the middle of the TPC. The pattern recognition then proceeds searching for the hits from the two neighboring planes in $z$-direction. These three hits together are used to find the sign of the track's curvature in $\phi$-direction which is, of course, the main bend direction of the particle's trajectory (see again Fig. 3.19). A window in the $\phi$-direction is then defined in which further hits are searched for, using the knowledge of the magnetic field in the TPC. Due to the strong inhomogeneity of the B field, it is not possible to find

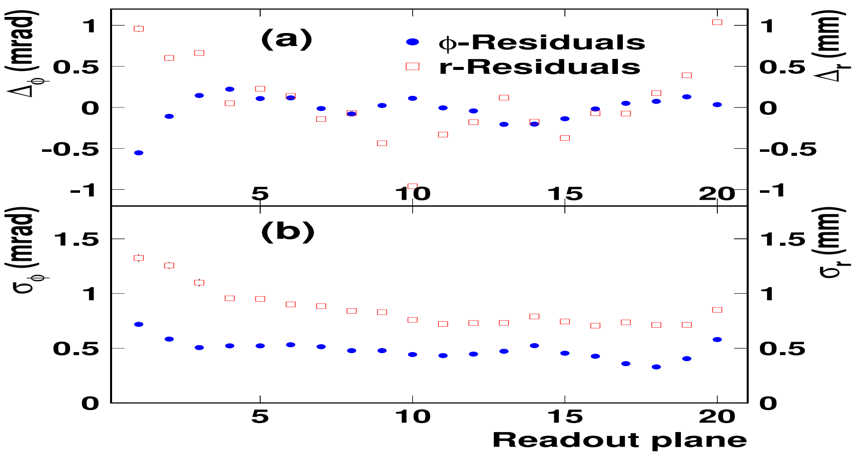


Figure 3.20: *Residuals of the true (reconstructed) hits relative to the fitted tracks in $r$- and $\phi$-direction for 1999 hadron data [39]. The $\Delta_{r,\phi}$ refer to the center-of-gravity, the $\sigma_{r,\phi}$ to the width of the respective residual distribution.*

an analytical solution for the track trajectory. Instead, the trajectory is defined using a two-dimensional momentum fit based on reference tables. These tables, produced in MC simulations, contain the hit coordinates of a reference particle with p=1GeV/c for different $\theta$-angles. After several iterations, only the hits close to the fitted track, typically within $dr$=2 cm and $rd\phi$=1 cm, are retained. The momentum is determined from the $\phi$-deflection, fitting the hits in the $\phi$-$z$ plane with a reference track, while the $\theta$ direction is obtained by fitting a straight line in the $r$-$z$ plane. The effects of multiple scattering are corrected for by assuming that all scattering originates from the mirror of RICH2, the largest amount of individual material in the spectrometer ($X/X_o$ ~4.7%) [54].

- Momentum resolution

A basic track property is the track length, the number of hits on the track. While the design value is 20, an average of only about 9 were found in the 1999 analysis, due to the problems with the TPC readout (see Fig. 4.6 in section 4.1.3). Tracks with a number of hits less that 4 were removed from the analysis.

The standard deviation of the distribution of differences between the original momentum and the reconstructed momentum is defined as the momentum resolution $\sigma_p$. It is determined at high momenta by the position resolution, at low momenta by multiple scattering. The position resolution realistically achieved in the 1999 analysis is summarized in Fig. 3.20 in terms of the residuals of the hits relative to the fitted tracks [39]. The values are about a factor of 2 above design.

All in all, the goal to achieve a mass resolution of $<2\%$, equivalent to a momentum resolution of also $<2\%$ for momenta of 2-3 GeV/c, could not be reached in 1999, due to the small number of hits/track, insufficient position resolution and the defects in the TPC readout. An attempt to obtain the momentum resolution vs. momentum in MC simulations, based on the understanding of the TPC as of the end of 2000, is shown in Fig. 3.21 [60]; it corresponds to a parametrization of $\sigma_p/p = ((0.04)^2 + (0.012 \cdot p)^2)^{1/2}$. According to the insight at the time of this

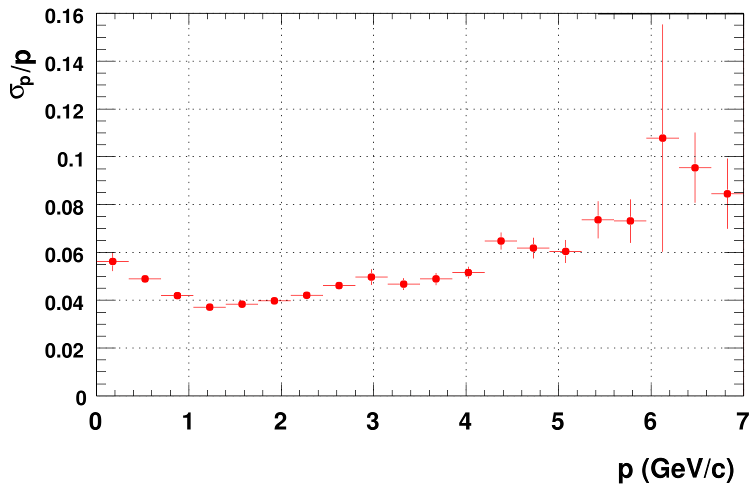


Figure 3.21: *Momentum resolution $\sigma_p/p$ vs. momentum, studied by using (somewhat idealized) Monte Carlo simulations for the 1999 TPC status [60].*

write-up, the slope constant of 0.012 may actually be unrealistically small. However, the only place in the whole present analysis where the numerical value of the TPC resolution enters is the folding process of the hadronic decay cocktail. To the extent that the 1999 statistics is completely insufficient to identify any of the narrow vector mesons $\omega$ or $\phi$ in the data, the precise resolution is in fact of minor importance.

- Particle identification by $dE/dx$

To support the electron identification done by the double RICH system, the specific energy loss of a particle traversing the TPC can be measured. The use of this tool in the 1999 analysis over the full range of momenta has indeed improved the $e/\pi$ separation compared to the previous analysis, where electrons and pions in the very-high momentum region could not be distinguished, and where an additional handle to suppress fake rings in the RICH's at lower momenta would also have been helpful. Operationally, since the charge collected for each hit along a

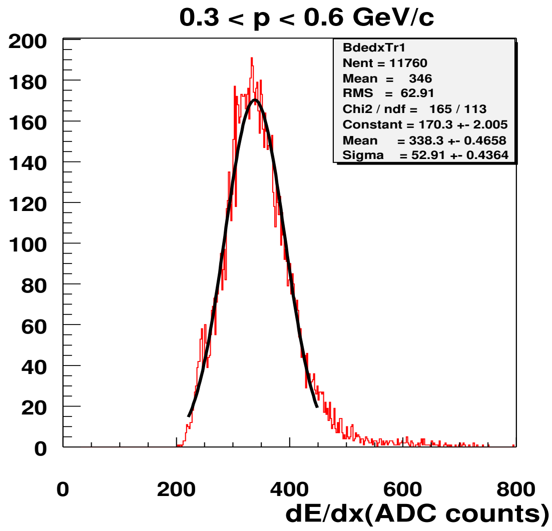


Figure 3.22: *The $dE/dx$ projection for $e^-$ tracks (from Fig. 3.24 in section 3.4.5) for the momentum selection 0.3<p<0.6 GeV/c. A Gaussian fit to the distribution gives a relative $dE/dx$ resolution of 16%.*

track is proportional to $dE/dx$, one could simply use the sum amplitude of all hits. Instead, as is common, the so-called "truncated-mean" procedure has been followed to reduce the fluctuations from the long Landau tails of the energy-loss distribution. Numerically, 35% of the highest-amplitude samples have been rejected to obtain a nearly Gaussian-like distribution. The resulting resolution of $\sigma(dE/dx)/dE/dx$ has been found to be $\sim$16% for electron tracks as shown in Fig. 3.22.

The dependence of the relative resolution in $dE/dx$ on the number of hits/track is plotted in Fig. 3.23. The comparison to various parametrizations is not quite satisfactory. However, these were done for Ar- rather than Ne-mixtures, and this change together with others for the ongoing analysis of the 2000 data seems to improve the agreement. The resolution value of $\sim$16% at a hit number of 9 can be read-off this plot; the full number of hits as expected for the 2000 analysis will automatically improve the resolution.

- Global geometrical alignment

  The geometrical alignment of the 16 chambers of the TPC is done using the data sample at zero magnetic field. The assumption is made that the RICH-coordinates are aligned with the beam and that the RICH gives $\theta$ and $\phi$ in absolute terms, thus defining a coordinate system to which all others detectors have to be matched. To find the proper values for the many correlated transformations

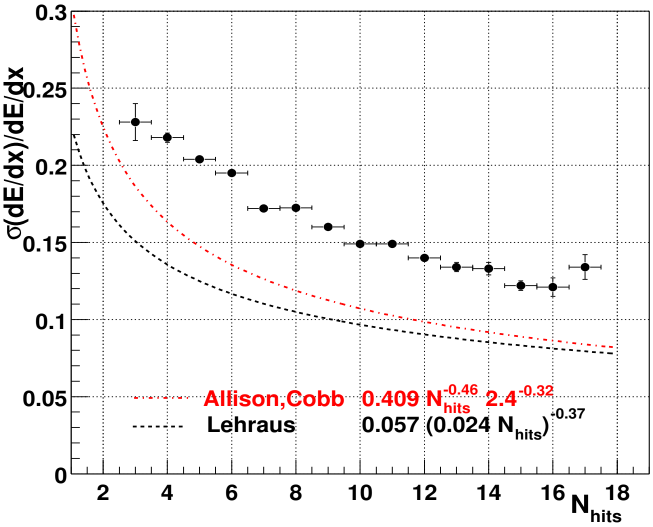


Figure 3.23: *$dE/dx$ resolution of the tracks in the TPC vs. the number of hits/track in comparison to different parametrizations (Lehraus and Allison/Cobb [58]). The measured results somewhat exceed these parametrizations (done for Ar-mixtures).*

like translations in x, y, z direction, rotations around the x, y, z axis, time offset and time factor, the MINUIT software was used.

### 3.4.5 Matching and Full Electron Track Reconstruction

Once the vertex is reconstructed and track segments in each of the detectors are found, the next major step is to combine them all into full electron tracks. Obviously, before starting the tracking, the local coordinates of the five detectors (2 SDD's, 2 RICH's and the TPC) need to be converted into the three-dimensional laboratory system. This global laboratory system uses left-handed Cartesian coordinates with the z-axis along the beam and the x and y-axis pointing to the right and upward, respectively, when looking along the beam direction. In the laboratory coordinate system, the origin is placed into the center of SDD-1, while in the event coordinate system the event vertex $(x_V, y_V, z_V)$ is taken as the origin. To reduce fake tracks as much as possible, efficient identification is required in all detectors. The double RICH system is powerful enough to nearly control the problem of hadron misidentification on its own. By matching SIDC- and TPC segments to the RICH system, $\sim$95$\%$ of all hadrons do not produce any signal.

In the postproduction (the second production step, see section 3.2), tracks are obtained from matching TPC tracks to global tracks, i.e. SIDC-RICH tracks. By pointing with SIDC-RICH matched candidates to the TPC, tracking in the TPC is only required within a window of $\pm$100 mrad in the $\phi$-direction around that candidate. The resulting tracks are expected to be dominated by electron tracks, due to the filtering by the RICH detectors. A contour plot of the $dE/dx$ distribution in the TPC versus particle momentum for these tracks is shown in Fig. 3.24. The dominance of electron tracks is easily recognized in the form of the most intense island with momentum-independent

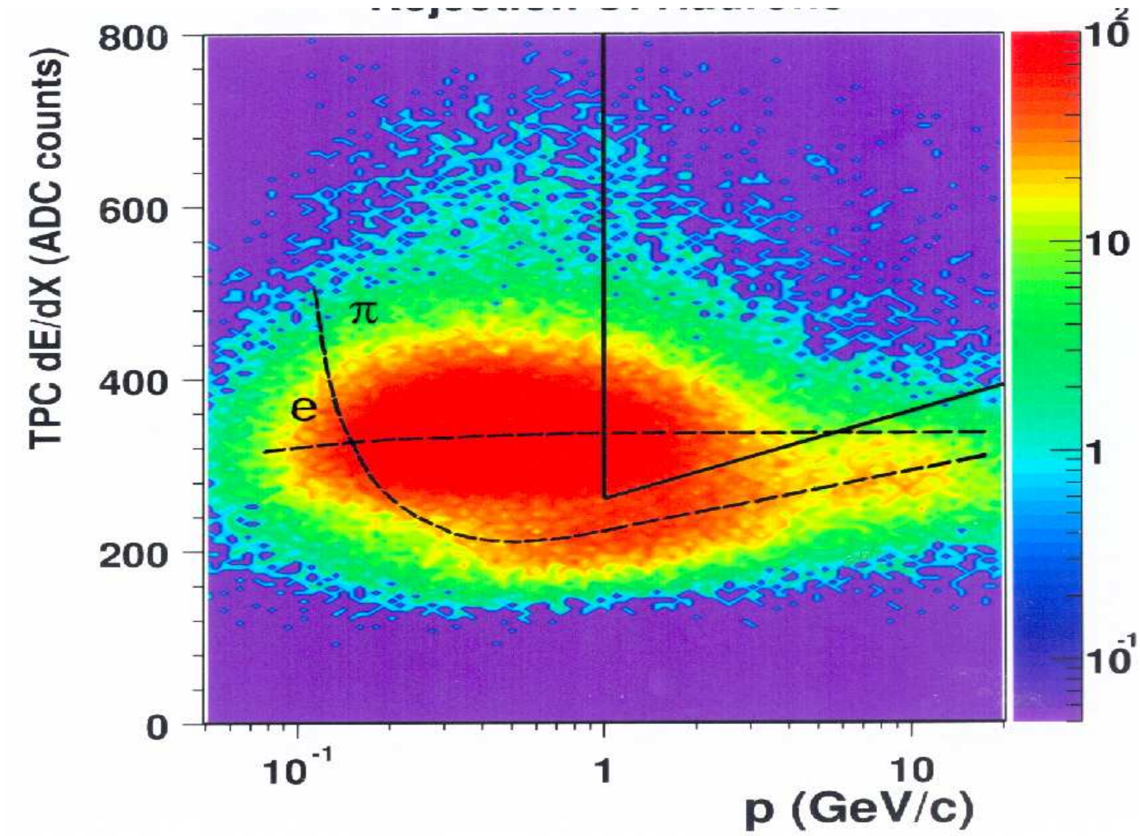


Figure 3.24: *Contour plot of the $dE/dx$ distribution in the TPC vs. particle momentum for electron-track candidates after the postproduction stage. The main island, described by the nearly-horizontal line, is dominated by low-momentum electrons from conversion- and Dalitz pairs. A $\pi^-$-contamination, following the expected $dE/dx$-line for pions (Bethe-Bloch), can also be recognized (see text); it is removed by the gliding cut parallel to the rising pion line. The vertical line indicates the single-electron $p_t$-cut $\geq$0.2 GeV/c$^2$ used to very much suppress the combinatorial background from low-mass pairs.*

values of $dE/dx$ around 350, well described by the (nearly horizontal) theoretical line for $e^-$. The very low average momenta around <p>=0.4 GeV/c (p$_t$=0.08 GeV/c) are consistent with the expectation for tracks originating from conversion and Dalitz pairs. The projection of this island onto the $dE/dx$ axis for 0.3<p<0.6 GeV/c corresponds exactly to the spectrum Fig. 3.22 shown in the preceding section. Two further much less intense islands with smaller values of $dE/dx$ can also be recognized. Both follow the expected line for $\pi^-$, taken over from Fig. 3.25. The region around $\sim$ 1GeV/c is due to $\pi^-$, misidentified as e$^-$ by the RICH (fake rings in regions of accidental high hit density). A projection onto the $dE/dx$ axis for the momentum selection 1<p<2 GeV/c (see Fig. 3.26) shows this contamination more quantitatively. The region around p$\sim$10 GeV/c is due to $\pi^-$ which create genuine Cherenkov rings with radii close enough to asymptotic electron rings to pass the ring selection cut; these tracks have inevitably to be there.

In the postpostproduction, a gliding cut along the line indicated in Fig. 3.24 be-

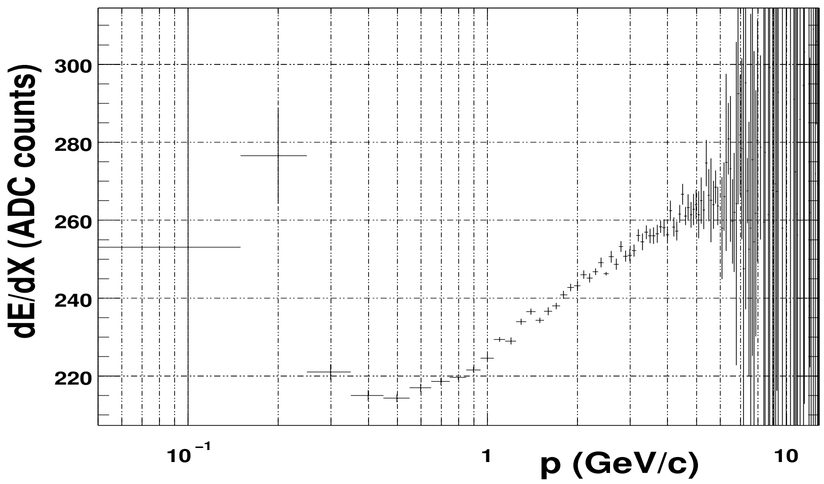


Figure 3.25: *Measured dependence of the mean ionization $\langle dE/dx \rangle$ on momentum for negatively charged particles from the TPC. The dashed line contained in Fig. 3.24 shows the theoretically expected dependence for the case of $\pi^-$; the functional form was taken from [55] and fitted to the region 0.3<p<2 GeV/c around the minimum. Above 2GeV, the data increasingly deviate from the $\pi^-$ expectation towards smaller values of $dE/dx$, due to the admixture of negative particles with higher masses, in particular $K^-$.*

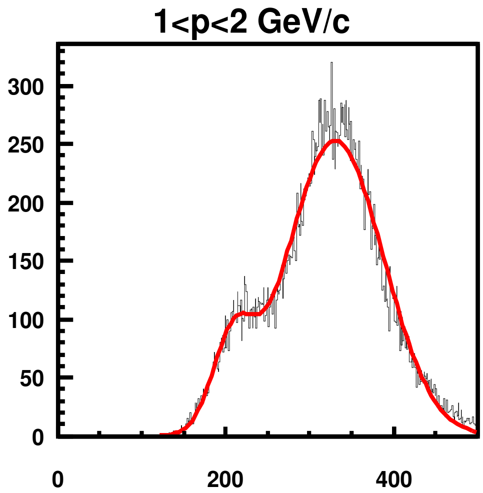


Figure 3.26: *The $dE/dx$ projection from Fig. 3.24 for the momentum region 1<p<2 GeV/c. It is dominated by electron tracks, but also shows some $\pi^-$ contamination (see text).*

tween the $e^-$ and $\pi^-$ islands is used to completely eliminate the residual hadron tracks. Indeed, only TPC tracks passing the cut are matched to global tracks. The other vertical line at p=1 GeV/c visible in Fig. 3.24 indicates the single-electron $p_t$-cut $\geq$0.2 GeV/c used to very much suppress the combinatorial background from low-mass pairs; this is discussed in more detail in section 3.5. Altogether, the efficient electron identification provided by the combined action of the double-RICH and the TPC allowed to minimize fake tracks to a negligible level, even at the highest $dN_{ch}/d\eta$. The matching distributions to be discussed next therefore consistently show a very low background.

The quality of the track matching between individual detectors is influenced by the multiple scattering which a particle suffers passing through the spectrometer, and therefore depends on the momentum of the particles. Integrating first over momenta, the quality of the matching distributions for electron tracks is shown in Fig. 3.27 for all 3 detectors. The $rms$ widths are broadened due to the fact that even after the geometric

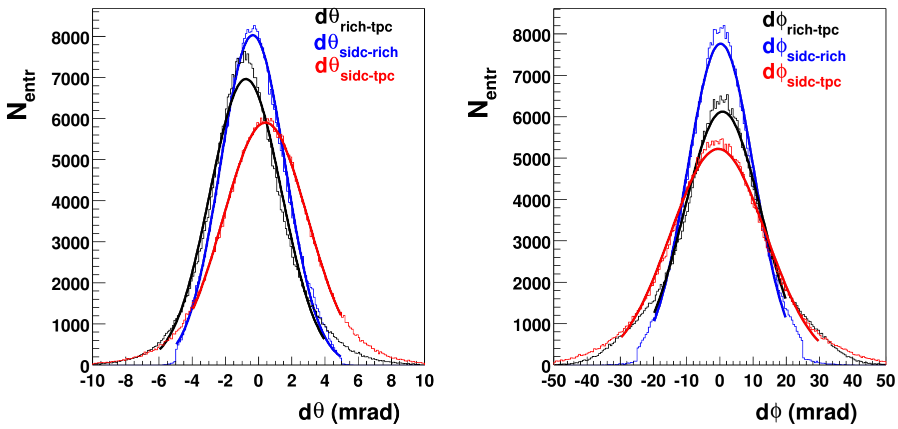


Figure 3.27: *Matching distributions in $\theta$ (left) and $\phi$ (right) for the three detector combinations RICH-TPC, SIDC-RICH and SIDC-TPC.*

intercalibration there is still a systematic misalignment of the detectors: the positions of the mean values for $d\theta$ and $d\phi$ deviate from zero. This is more detailed in Figs. 3.28 and 3.29, showing the variation of the centers of the differential matching distributions with $\theta$ and $\phi$; this variation obviously contributes to the widths in Fig. 3.27.

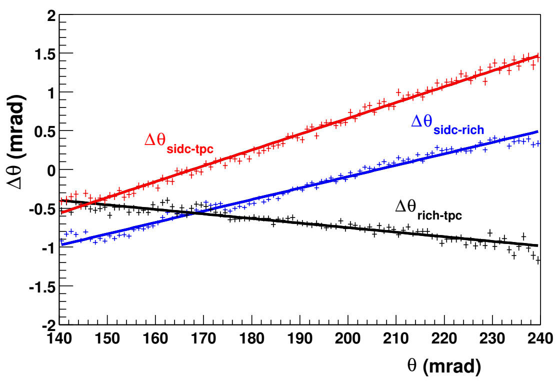


Figure 3.28: *Variation $\Delta\theta$ of the centers of the differential matching distributions in $\theta$ as a function of $\theta$ for the three detector combinations RICH-TPC, SIDC-RICH and SIDC-TPC.*

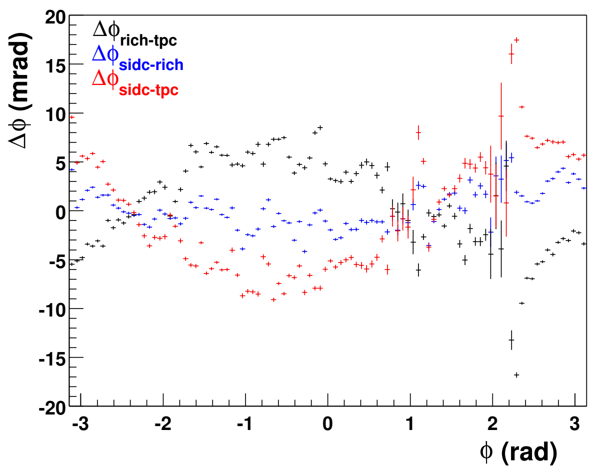


Figure 3.29: *Variation $\Delta\phi$ of the centers of the differential matching distributions in $\phi$ as a function of $\phi$ for the three detector combinations RICH-TPC, SIDC-RICH and SIDC-TPC.*

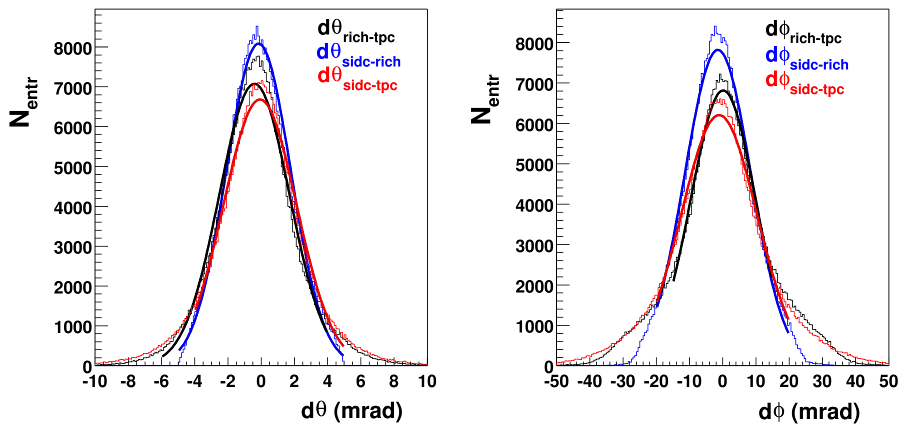


Figure 3.30: *Matching distributions in $\theta$ (left) and $\phi$ (right) for the three detector combinations RICH-TPC, SIDC-RICH and SIDC-TPC, after applying the corrections for misalignment.*

After recognizing the problem of residual misalignments, an ad-hoc correction procedure was applied, operating separately on all three detector combinations RICH-TPC, SIDC-RICH and SIDC-TPC [44, 60]. The procedure fits the matching distributions in a number of different $\theta$- and $\phi$- bins (7 in $\theta$, 16 in $\phi$), assuming Gaussian peaks and a parabolic background, derives correction values and feeds these back into the primary matching procedure. The improved results are shown in Fig. 3.30, 3.31 and 3.32, indicating smaller widths in the overall matching distributions and much less variation of the centers of the differential matching distributions.

A fair judgement of the final matching widths can only be done by disentangling the effects of multiple scattering. This is done in Figs. 3.33 and 3.34, showing the variation of the widths in $\theta$- and $\phi$-matching, resp., as a function of particle transverse

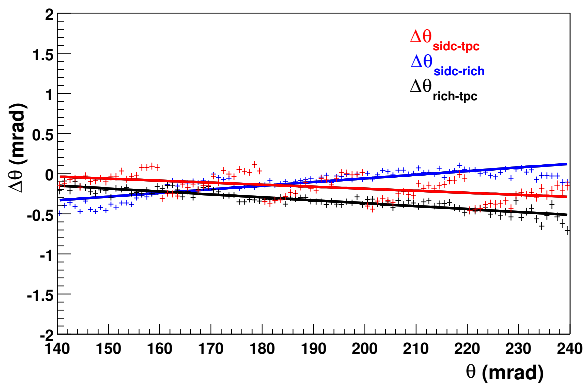


Figure 3.31: *Variation $\Delta\theta$ of the centers of the differential matching distributions in $\theta$ as a function of $\theta$ for the three detector combinations RICH-TPC, SIDC-RICH and SIDC-TPC, after applying the corrections for misalignment.*

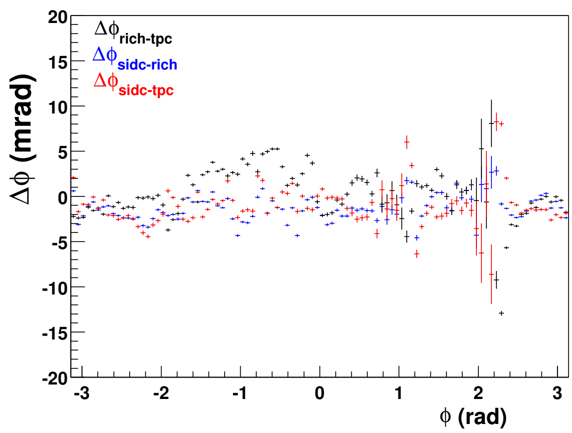


Figure 3.32: *Variation $\Delta\phi$ of the centers of the differential matching distributions in $\phi$ as a function of $\phi$ for the three detector combinations RICH-TPC, SIDC-RICH and SIDC-TPC, after applying the corrections for misalignment.*

momentum. Asymptotically at high momenta, values of 1.2-1.6 mrad in $\theta$ and 7.5-9 mrad in $\phi$ are reached. These are still larger than the comparable numbers in the 1996 analysis. On the other hand, as mentioned before, the background is extremely low, due to the superior electron identification by the combined action of the double RICH and the $dE/dx$ from the TPC, essentially eliminating all fake tracks. Therefore, very wide matching cuts of $\pm 3\sigma$ have been used throughout. The broad matching cuts of $\pm 3\sigma$ between TPC-RICH and TPC-SIDC are done in a momentum-dependent way, following the functional dependence of Figs. 3.33 and 3.34, while the matching cut between the RICH and the SIDC is done in a constant circular window with a radius of 5 mrad.

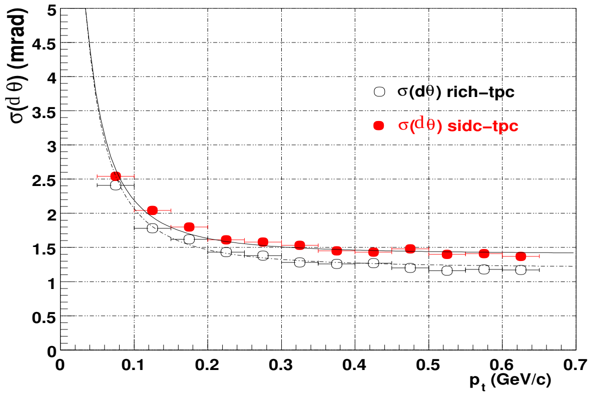


Figure 3.33: *Widths of the matching distributions in $\theta$ as a function of particle transverse momentum after applying the corrections for misalignment.*

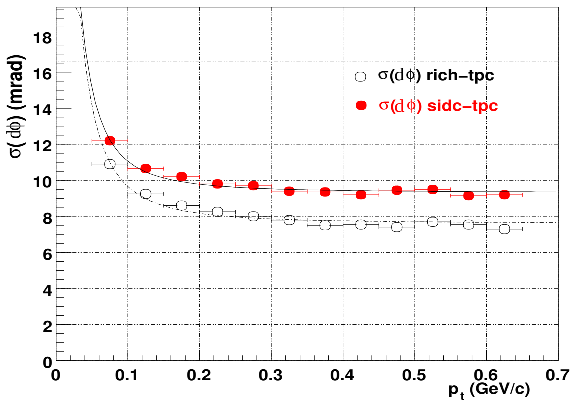


Figure 3.34: *Widths of the matching distributions in $\phi$ as a function of particle transverse momentum after applying the corrections for misalignment.*

## 3.5 Pairing and Combinatorial Background

### 3.5.1 Definition of Signal and Combinatorial Background

In the final step of data processing, tracks are combined into pairs, and the type of pairs is defined. Electron and positron tracks are measured in the same acceptance and with the same reconstruction efficiency. The main and very difficult task is then to extract the desired correlated unlike-sign pairs from the reconstructed single tracks because a flag on what belongs together does not exist. Therefore, a statistical procedure has to be used. Pairing is done by creating all possible combinations of electron and positron tracks from the same event. Integrating over all events, a number of unlike-sign ($N_{+-}$) and a number of like-sign ($N_{++}$,$N_{--}$) pairs is obtained. The total unlike-sign pairs consist of the correlated pairs which are the real physics signal $S^{corr}_{+-}$ originating from the same decays, and of the uncorrelated unlike-sign pairs which are combinatorial background made by pairing tracks from different decays:

$$S_{+-}^{corr} = N_{+-}^{total} - N_{+-}^{uncorr} \tag{3.3}$$

As mentioned before several times and detailed below, the background problem is indeed severe. There are two known techniques for defining the background to be subtracted: the so-called like-sign technique, and the event mixing technique. Both work successfully due to the absence of important correlated components in the like-sign dilepton spectra in this region. Starting from the Poisson probability distribution of the electron and positron multiplicity [56] and using the fact that both charges have the same acceptance and the same track reconstruction efficiency, it is easy to show that the mean unlike-sign combinatorial background is given by twice the geometrical mean of the like-sign pairs, which is very insensitive (more than the arithmetic mean) towards the small charge asymmetries present in the experiment:

$$N_{+-}^{uncorr} = B_{comb.} = 2 \cdot \sqrt{N_{++} \cdot N_{--}} \tag{3.4}$$

The physics signal $S_{+-}^{corr}$ searched for in the CERES experiment consists of correlated electron-positron pairs in the invariant mass range $m >$0.2 GeV/c$^2$. The invariant mass is determined as usual from the sum of the four-momentum squares as

$$m_{pair} = \sqrt{\mathbf{p}_{\mu\mathbf{e}^+}^{\mathbf{2}} + \mathbf{p}_{\mu\mathbf{e}^-}^{\mathbf{2}}} \tag{3.5}$$

Since the rest mass of the electrons is small, the relativistic limit E$\sim|p|$ holds, allowing to determine the invariant mass only from the three momenta of the tracks:

$$m_{pair} = \sqrt{2 \cdot p_{e^+} p_{e^-} (1 - cos\Theta_{ee})} \tag{3.6}$$

As already discussed in the introduction, the abundance of the pairs to be investigated is only of order 10$^{-5}$ relative to the hadrons present. The efficient electron identification (see previous section) powerfully copes with the problem of hadron misidentification. The much more severe problem is the ratio of again only 10$^{-5}$ relative to the total $\gamma$'s present. Photons convert in the target and in the detector material immediately thereafter, and although the total material has been optimized to be only $\sim$1% of a radiation length, these photon conversions together with $\pi^0$-Dalitz decays still exceed the number of high mass pairs by a factor of $\sim$10$^3$. In other words: low-mass pairs would have to be recognized and taken out of the combinatorics on the level of a factor of 10$^3$ to assure an (idealized) signal-to-background ratio of 1/1. This is indeed *the* problem of the CERES experiment.

Fortunately, the kinematic characteristics of the two main electron sources $\gamma$ conversions and Dalitz pairs are quite different from those of the high mass pairs. First, they have very soft single-electron p$_t$ spectra; the average $p_t$ is only $\sim$ 0.08 GeV/c, $1/4$ of that of the mother pions. Therefore, a single $p_t$-cut of 200 MeV/c is extremely effective and *one of most important rejection handles* of background. Second, connected to their small invariant mass $\ll$0.2 GeV/c$^2$, they have small opening angles. For identification and rejection of such close pairs on the basis of the opening angle, it is extremely

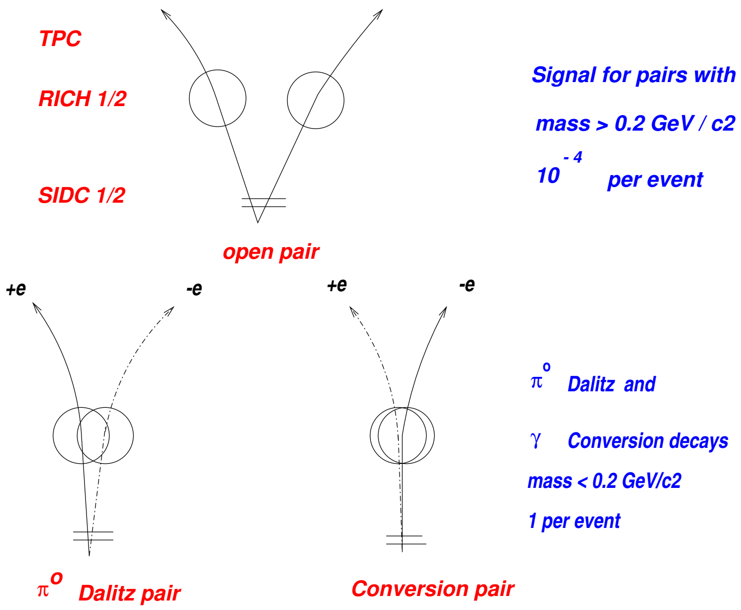


Figure 3.35: *Signature of a genuine open pair with two hits in the SIDC detectors, two rings in the RICH detectors and two opposite-sign (bent) tracks in the TPC (upper part). Two close pairs in the same event, only partially reconstructed; the two lone tracks form an open pair with two opposite-sign electrons, i.e. a high-mass combinatorial-background pair (lower part).*

important that, due to zero magnetic field up to the TPC, the opening angle remains unchanged in the major part of the setup until the TPC. Still, even given that the characteristics ($p_t$, m, $\theta_{ee}$) of the two main electron sources are so different from high mass pairs, limited track reconstruction efficiency and acceptance lead to a remaining *combinatorial high mass background*. An imperfect recognition of close pairs generates lone tracks, if the co-track is lost because of falling out of acceptance, or of not getting reconstructed, or of getting incorrectly assigned. The lone track will contribute to the pairing and create combinatorial background. Events in which two or more low-mass pairs are only partially reconstructed are particularly dangerous, since the resulting combinatorial pairs have automatically large opening angles and therefore contribute to the high-mass range of interest. This is illustrated schematically in Fig. 3.35. An only small fraction of close pairs with only one recognized track gives rise to random pair combinations with a sufficiently large Poissonian probability to easily outnumber the signal. To reduce the background as much as possible beyond efficient electron identification, an effective rejection of low-mass pairs in SIDC1/2, RICH1/2, and, to some extent, in the TPC is absolutely vital.

About $\sim 90\%$ of all pairs with opening angles $< 50$ mrad and invariant masses below 150 MeV/c$^2$ result from Dalitz decays, therefore the physics pair sample is restricted to m>200 MeV/c$^2$. However, a Dalitz-pair sample with m<200 MeV/c$^2$ and opening angles $\geq$35 mrad has also been collected. It is used to control the pair reconstruction efficiency after various rejection steps and, very important, to help to assess the pair reconstruction efficiency vs. multiplicity $dN_{ch}/d\eta$ in control of the MC simulations (see chapter 4).

### 3.5.2 Reduction of the Combinatorial Background

A big challenge in the pair analysis is then to maximally reject the recognized low-mass pairs with small opening angles, while keeping a high reconstruction efficiency for pairs with larger opening angles. The detailed individual steps taken to reach this goal are described in the following.

Benefitting from the difference in kinematic characteristics between low- and high-mass pairs, a transverse momentum cut of $p_t$>100 MeV/c on each track selected by electron identification is already done in postpostproduction, i.e. in the third production stage. Raising the $p_t$-cut on single electron tracks later to >200 MeV/c leads altogether to a drastic reduction of the combinatorial background by a factor of >10. In the next stage, an opening-angle cut of $\theta$>35 mrad is applied as in the 1996 analysis.

The evolution of the total number of pairs for the remaining rejection steps is shown in Fig. 3.36. A further factor of 10 in background reduction is achieved, but not the factor of 100 required for the idealized case of S/B=1/1. The plot starts at a point where the strong reduction of the background (without affecting too much the high mass signal) has already occurred through the $p_t$-cut. To reject very close pairs, certain isolation cuts to assure the cleanliness of a track environment are imposed both in the SIDC's and in the RICH's. Close conversion- and Dalitz pair recognition is most powerfully achieved by summing the pulse heights up to an opening angle of 10 mrad in the two SIDC detectors. Pairs with opening angles < 10 mrad which are not recognized as two close individual electron rings in the RICH detectors appear than as double-$dE/dx$ information in the two SIDC detectors in a correlated way (see Fig. 3.37). The cut along the lines indicated in the figure completely removes these close pairs. The combinatorial background is thereby reduced by a factor of 5, while the pair efficiency is kept at a level of $\sim$65% (see Fig. 3.40 below and chapter 4). The power of the correlated cut in two independent SIDC detectors is best illustrated by projecting the two islands in Fig. 3.37 onto the two axis of independent SIDC1 and SIDC2 information (Fig. 3.38). If only one detector would exist, good rejection would automatically destroy good efficiency (and vice versa).

As mentioned before, the double-RICH system can resolve neighboring double rings already at 7 mrad (50% probability level). The SIDC double-hit resolution in the 1999 data analysis was supposed to be improved compared to 1996 in resolving double hits, both in anode and in time bin direction, to a level of $\leq$5 mrad (see section 3.3.1 above). However, the problem of artifical hit splitting completely prohibited the use of resolved double hits and therefore double tracks up to at least 5 mrad (as also discussed already in section 3.3.1). This is dramatically apparent from the contour plot of the angular-distance distributions between neighboring hits, shown in Fig. 3.39 for both SIDC detectors. Efficient rejection is therefore much better obtained by integrating information rather than to resolve it. All hits in a circular window of 10 mrad (also

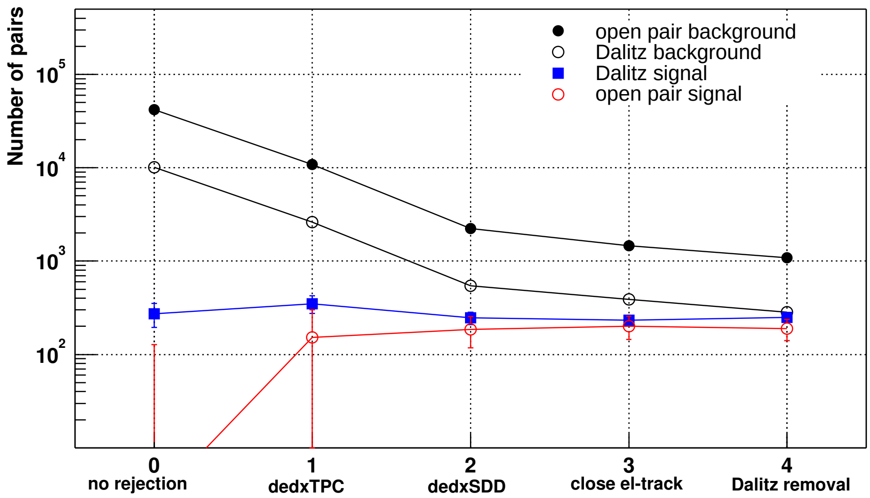


Figure 3.36: *The upper (black) line shows the open-pair combinatorial background calculated as the total like-sign pairs with masses >200 MeV/c$^2$. Similarly, the background in the Dalitz region is determined as the like-sign pairs with m≤200 MeV/c$^2$. The net open-pair signal (red line) defined as $(N_{+-} - B)$ consists of electron-positron pairs in the invariant mass range m>200 MeV/c$^2$, while the net Dalitz signal consists of $e^+e^-$ pairs in the mass region of m≤200 MeV/c$^2$ with an opening angle selection of ≥35 mrad. The combinatorial background strongly decreases for the different rejection steps by a factor of 10 (disregarding the particle-ID contribution of a factor of 5), while the pair efficiency as controlled by the positively identified Dalitz pairs remains nearly constant.*

shown in Fig. 3.39) are summed, and genuine close tracks up to an opening angle of 10 mrad appear as clean double $dE/dx$ information in Fig. 3.37.

Although the cut value of 1000, used in the two SIDC detectors (Fig. 3.37) to remove close pairs, looks natural, an objective tool to optimize the cut was developed (and also used for other cuts). Any handle to reject tracks from low-mass pairs leads to unavoidable efficiency losses for the desired tracks; therefore, all rejection cuts have to be optimized. The optimization is done by maximizing the effective signal, defined as $S_{eff} = S/(1 + 2 \cdot B/S)$. For S, the Dalitz signal is used (defined in eq. 3.3) with opening angles $\theta$>35 mrad and m<200 MeV/c$^2$, while for B the open pair background is used (defined in eq. 3.4) with opening angles $\theta$>35 mrad and m>200 MeV/c$^2$. In the limit $B/S \gg 1$, the effective signal becomes $S_{eff} \sim S^2_{dal}/B_{open} \sim \epsilon^2/Rej$, and this then should be maximal. The efficiencies and rejection factors are defined as follows: $\epsilon = \prod_{i=1}^{ncut} S_i^{dal}/S_{i-1}^{dal}$ and $Rej = \prod_{i=1}^{ncut} Rej_i = \prod_{i=1}^{ncut} B_i/B_{i-1}$, where $S_0^{dal} = S_{initial}^{dal}$ and $B_0^{open} = B_{initial}^{open}$. The potential danger of this optimization method is to create a signal out of statistical upward fluctuations by the choice of the cut. Indeed, the method would be unthinkable, if the high-mass signal itself with its unfavorable S/B would be used for S. It is the rather stable Dalitz part (statistically totally independent of the high-mass background) which makes the procedure legitimate.

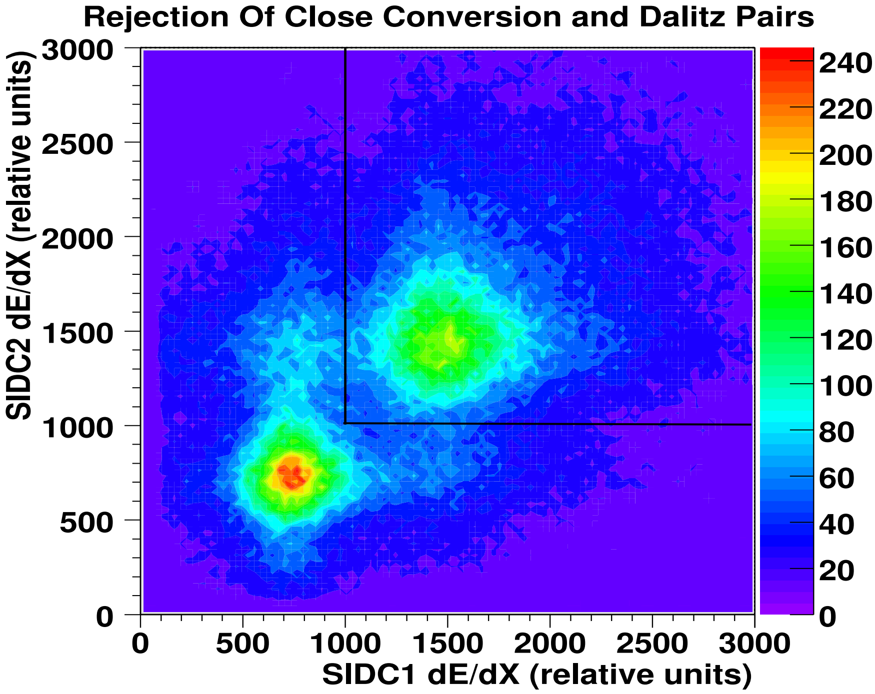


Figure 3.37: *Contour plot of the distributions of $dE/dx$ in SIDC2 vs. $dE/dx$ in SIDC1. The two dominant islands, separated by the lines, correspond to single tracks (with $dE/dx$ < 1000 in both SIDC's) and double tracks (with $dE/dx$ >1000 in both SIDC's). The double tracks are mostly conversions (and very close Dalitz pairs) from the target; they are rejected by cutting double $dE/dx$ in both detectors as indicated by the cut lines. A much less intense contribution from late conversions (in SIDC1) is visible as a weak island with double-$dE/dx$ in SIDC2, but with (smeared) single-$dE/dx$ in SIDC1.*

The result of the optimizition is shown in Figs. 3.40, 3.41. The cut value of 1000 chosen before is clearly favored. To prove that the choice of Dalitz pairs does make the procedure uncritical, the same quantity $S^2_{dal}/B_{open}$ was evaluated in Monte Carlo simulations, overlaying Dalitz pairs with data (see chapter 4). The results are shown in Fig. 3.42; they are absolutely identical to those using Dalitz pairs from data and therefore justify the original procedure. Fig. 3.40 also allows to simultaneously see the effect of the $dE/dx$ cut on the open-pair background and on efficiency: Both decrease with the cut-value, reaching an optimum with a background reduction by a factor of $\sim$5 and a track efficiency loss of $\sim$20$\%$ (remaining pair efficiency $\sim$0.65).

In summary then, conversion- and Dalitz pairs with opening angles $\leq$10 mrad which cannot be recognized as two individual rings in the RICH detectors are efficiently rejected by the two SIDC detectors. Some remaining contribution of close pairs with $\theta$<10 mrad is due to inefficiencies in the SIDC's.

As mentioned before, data taking in 1999 suffered from the poor performance of the TPC readout, resulting in a TPC pair efficiency of only $\sim$19$\%$ (see chapter 4.). Even

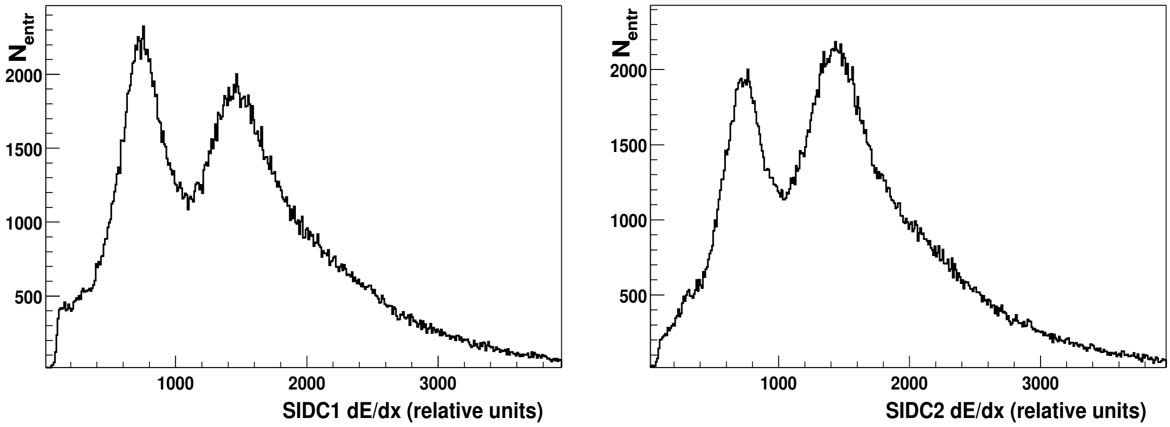


Figure 3.38: *Projections of the distributions from Fig. 3.37 onto the two $dE/dx$ axis before applying the rejection cut. It is clear that $dE/dx$ information for efficient rejection can only be used in a correlated way; otherwise, a cut at the minima, separately in both SIDC's, would lead to a high efficiency loss, due to removing the long Landau tails of single tracks.*

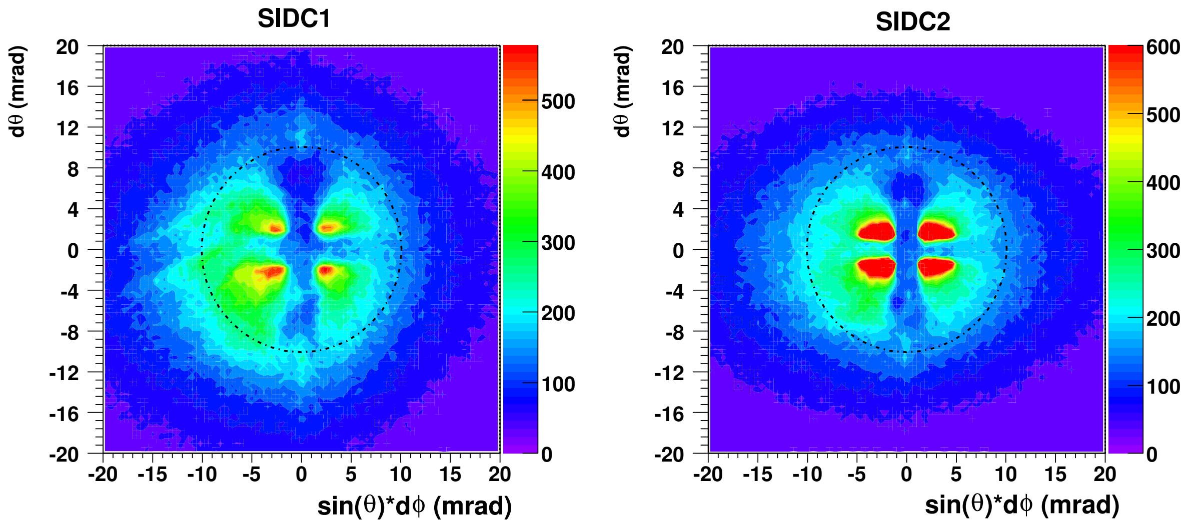


Figure 3.39: *Angular-distance distribution between neighboring hits in a $d\theta$- vs. $sin(\theta) \cdot d\phi$-plane. The circles indicate the distance of ≤10 mrad for hits to be summed. The gap in the middle corresponds to the limit of double hit resolution, while the bright spots signify the effects of artificial hit splitting.*

if the efficiency of the TPC would be high, its usefulness for low-mass pair rejection would still be limited, due to a strong decrease of the track reconstruction efficiency for low momenta ($p_t$<200 MeV/c), i.e. for the momentum range of conversion- and Dalitz pairs ($\langle p_t \rangle$~80 MeV/c). Given a track candidate with $p_t$>200 MeV/c, the other partner of a pair may well be much softer and will therefore not be reconstructed by the TPC, even if pair opening angles >10 mrad are accessible.

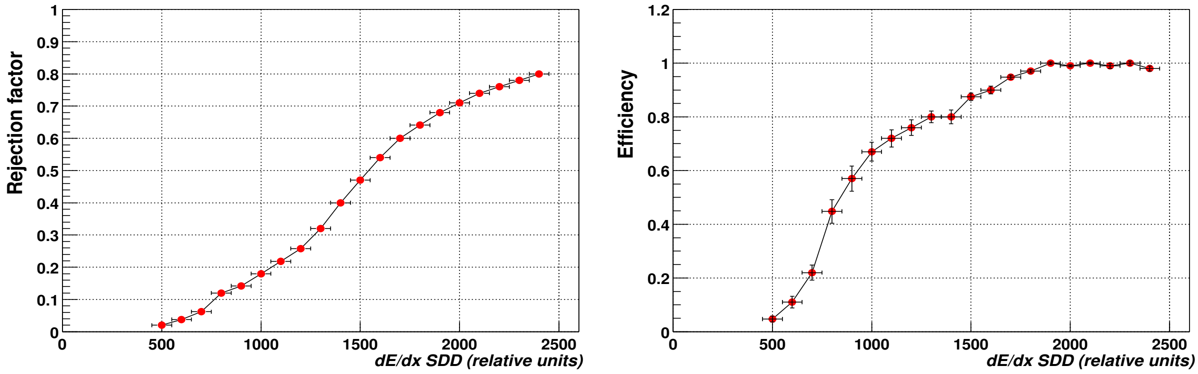


Figure 3.40: *Relative rejection of open-pair background (left panel) and relative efficiency of Dalitz pairs (right panel) vs. $dE/dx$ cut applied in the two SIDC's in a correlated way (see Fig. 3.37). In both cases, the normalization is done to the respective preceding step.*

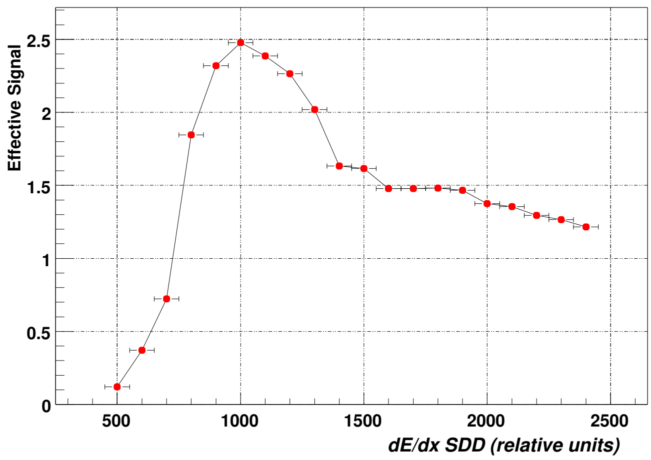


Figure 3.41: *Effective signal $S_{eff} = S^2_{dal}/B_{open} \sim \epsilon^2/Rej$ vs. cut value, using Dalitz pairs and open-pair background, i.e. relative efficiency and relative rejection from Fig. 3.40 (see text).*

To reject low-mass pairs with opening angles >10 mrad, a different strategy is therefore used, relying on the superior performance of the double-RICH system. All full electron tracks which have a SIDC-RICH electron-candidate track within 70 mrad, are removed even if that candidate has no match to the TPC (interpreting it to be the second leg of a close pair). Since there is no magnetic field in the RICH's, the opening angle can be calculated from the polar coordinates $\theta$ and $\phi$ measured by the RICH system. The cut value of 70 mrad is evaluated as before, maximizing the effective signal. In the final step, identified Dalitz pairs, i.e. pairs with m<200 MeV/c$^2$ are excluded from further combinatorics. As can be read-off from Fig. 3.36, the last two steps together reduce the background by a further factor of 2, while their effect on efficiency is nil.

The evolution of the total number of pairs after various rejection steps can be sum-

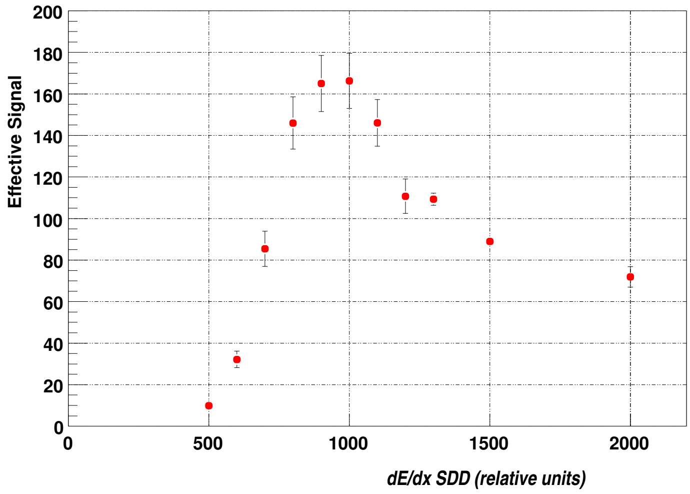


Figure 3.42: *Same as Fig. 3.41, but using Monte Carlo simulations with $\pi^0$-Dalitz pairs overlayed onto data.*

marized as follows (Fig. 3.36): Altogether, a rejection factor of >100 is obtained (including the $p_t$-cut), while at the same time, the efficiency losses for open pairs associated with the rejection cuts are less than a factor of 2, as illustrated by the positively identified Dalitz pairs with opening angles >35 mrad and masses m<200 MeV/c$^2$. The physics signal, defined by the open pairs with m>200 MeV/c$^2$, is seen to be also roughly constant showing, at least within the large errors, that its *size is stable even if the background varies by a large amount*.

One further rejection cut has actually been investigated in some detail: the so called "predictor cut". To reject low-mass pairs with opening angles >10 mrad, where the double-ring resolution of the RICH-system is sufficient to resolve two close rings, the SIDC information on two close tracks can be used as a predictor of the two ring centers. With properly chosen masks around these centers, the analogue sum of the hit amplitudes of the two rings can then be created and used as a cut variable to distinguish single from double rings. Monte Carlo simulations of this procedure have been encouraging [48]. However, the dynamical range between single- and double ring amplitudes turned out to be much smaller in the data than in the MC simulations, and the cut was finally discarded as too risky without having reached complete understanding.

It should at the end be emphasized that only very few rejection cuts have altogether been applied. All of them are perfectly understood by using either the data themselves (as explained above) or Monte Carlo simulations. The small number and the good understanding of the rejection cuts results in correspondingly small contributions to the systematic uncertainties of the high-mass yield (see chapter 5).

### 3.5.3 Strategies of Background Subtraction

The net signal $S_{+-}^{corr}$ of the correlated unlike-sign pairs was already defined and discussed in section 3.5.1 (eqs. 3.3 and 3.4). It is given, in simplified notation, by

$$S_{+-} = N_{+-} - 2 \cdot \sqrt{N_{++} \cdot N_{--}}, \tag{3.7}$$

using the like-sign technique for describing the combinatorial background. The geometrical mean of $N_{++}$ and $N_{--}$ contained in eq. (3.7) is robust in case of slight charge asymmetries. However, a test of charge symmetry presented in Fig. 3.43 shows the background to be symmetrical on the level of $1.05 \pm 0.02$ (before rejection) or $0.98 \pm 0.05$ (after rejection). Therefore, the arithmetic mean could just as well have been used in the analysis. Indeed, the relative difference between one and the other is given by $\delta \approx 1/8\Delta^2$, where $\Delta$ defines the relative charge asymmetry; for $\Delta$=10%, for example, $\delta$ would only be $10^{-3}$.

The statistical error of the signal $S_{+-}$ defined by eq.(3.7) is given by

$$\delta S_{+-} = (N_{+-} + N_{++} + N_{--})^{1/2} \tag{3.8}$$

assuming statistical independence of the errors in $N_{+-}$, $N_{++}$ and $N_{--}$ (this result is actually independent of whether the geometrical or the arithmetic mean is used for the background). Since S$\ll B_{comb}$, $N_{+-} \approx N_{++} + N_{--} \approx B_{comb}$ and

$$\delta S_{+-} \approx (2B_{comb})^{1/2} \tag{3.9}$$

which is obviously very much larger than $(S_{+-})^{1/2}$. In the alternative procedure of high-statistics event mixing for defining the like-sign combinatorial background, the error could potentially be reduced by a factor of $\sqrt{2}$, if the problem of *absolute normalization* of the background per event could be solved. However, none of the previous analysis efforts of CERES including the most recent one on 1996 data [56] has been able to find a solution, and therefore the final errors quoted on the *sum signal* have always been the one defined by eq. (3.8).

The situation becomes somewhat different if the background subtraction in eq. (3.7) is done bin-by-bin in *differential spectra*, for example in every bin of an invariant mass spectrum. The statistical error given by eqs. (3.8), (3.9) can then be *locally* reduced by a factor of $\sqrt{2}$ in each bin, if at least the *shape* of the like-sign combinatorial background can be determined with sufficient accuracy. The error of the sum over all bins does, of course, remain unaffected.

The local improvement of the spectral significance has been done in all previous CERES analysis work. Originally, the background was simply smoothed by using an appropriate fit function. In the 1995 ([18, 19, 23]) and 1996 ([20, 21, 22, 23]) analysis, the like-sign pair background was generated by a random combination of single tracks in high-statistics Monte Carlo simulations; the track distributions in $p_t$, $\theta$ and $\phi$ were directly taken from the experimental data. Small residual deviations from the measured like-sign background were taken care off by a correction function. In the most recent 1996 analysis [56], high-statistics event mixing was used which creates an unlike-sign

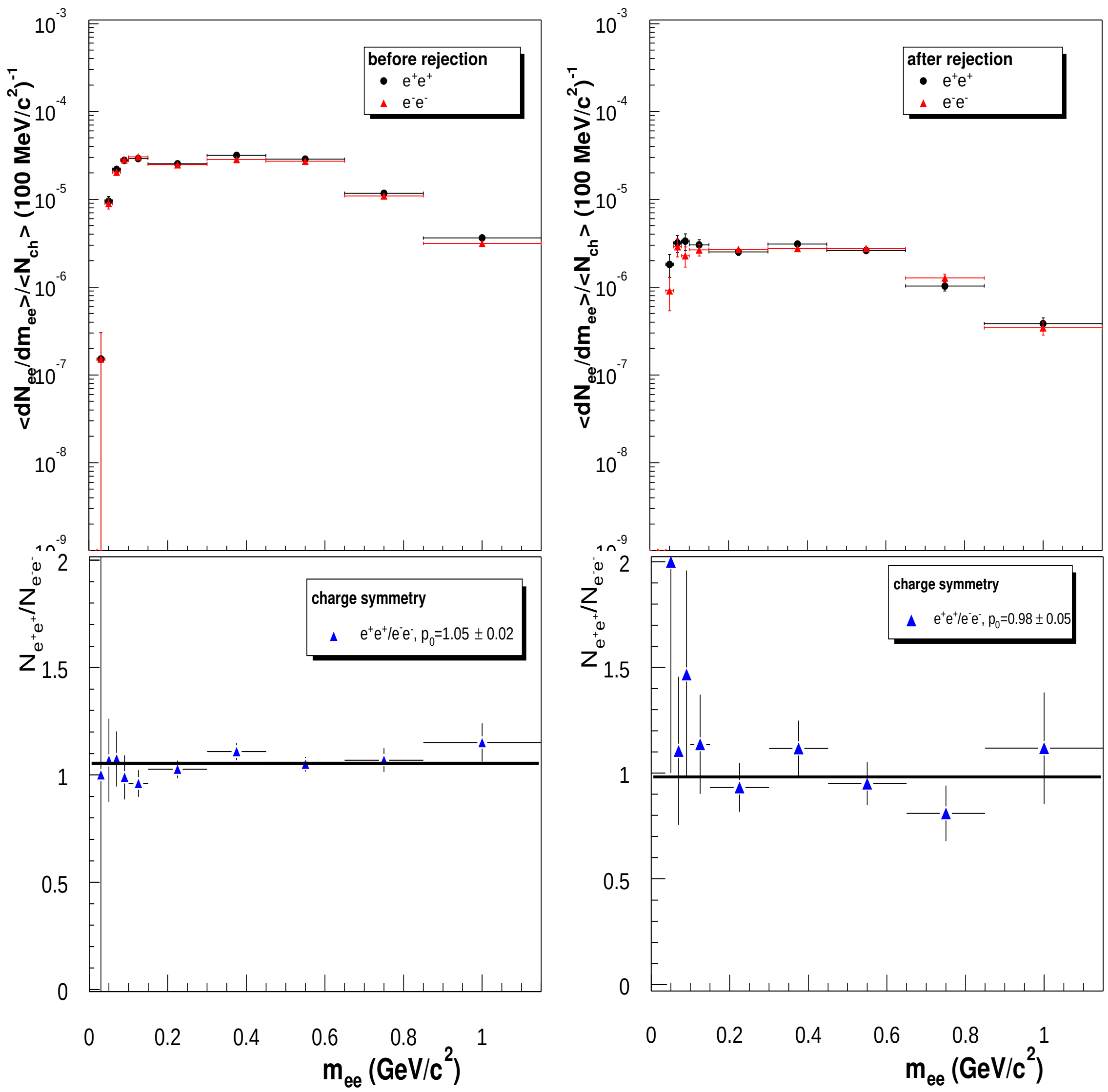


Figure 3.43: *Upper panel: Like-sign combinatorial background* $N_{++}$ *and* $N_{--}$ *vs. invariant mass* $m_{ee}$ *for partial rejection corresponding to the second step in Fig. 3.36 (only* $p_t$ *and TPC* $dE/dx$ *cut) (left panel), and for full rejection corresponding to the last step in Fig. 3.36 (right panel). The normalization of the ordinate is described in chapter 5. Lower panel: Ratio of* $N_{++}/N_{--}$ *for the two rejection cases.*

combinatorial background in addition to the like-sign one (identical by construction); also here, residual deviations had to be corrected.

In the present work, a still different approach has been taken. Since the like-sign combinatorial background after rejection step 1 in Fig. 3.36 (only $p_t$- and TPC $dE/dx$ cut) contains about 10 times more entries than the final background after all rejection steps, it was felt completely sufficient to properly rescale it and then use it directly, bin-by-bin, for background subtraction; with a down-factor of 10, the residual statistical

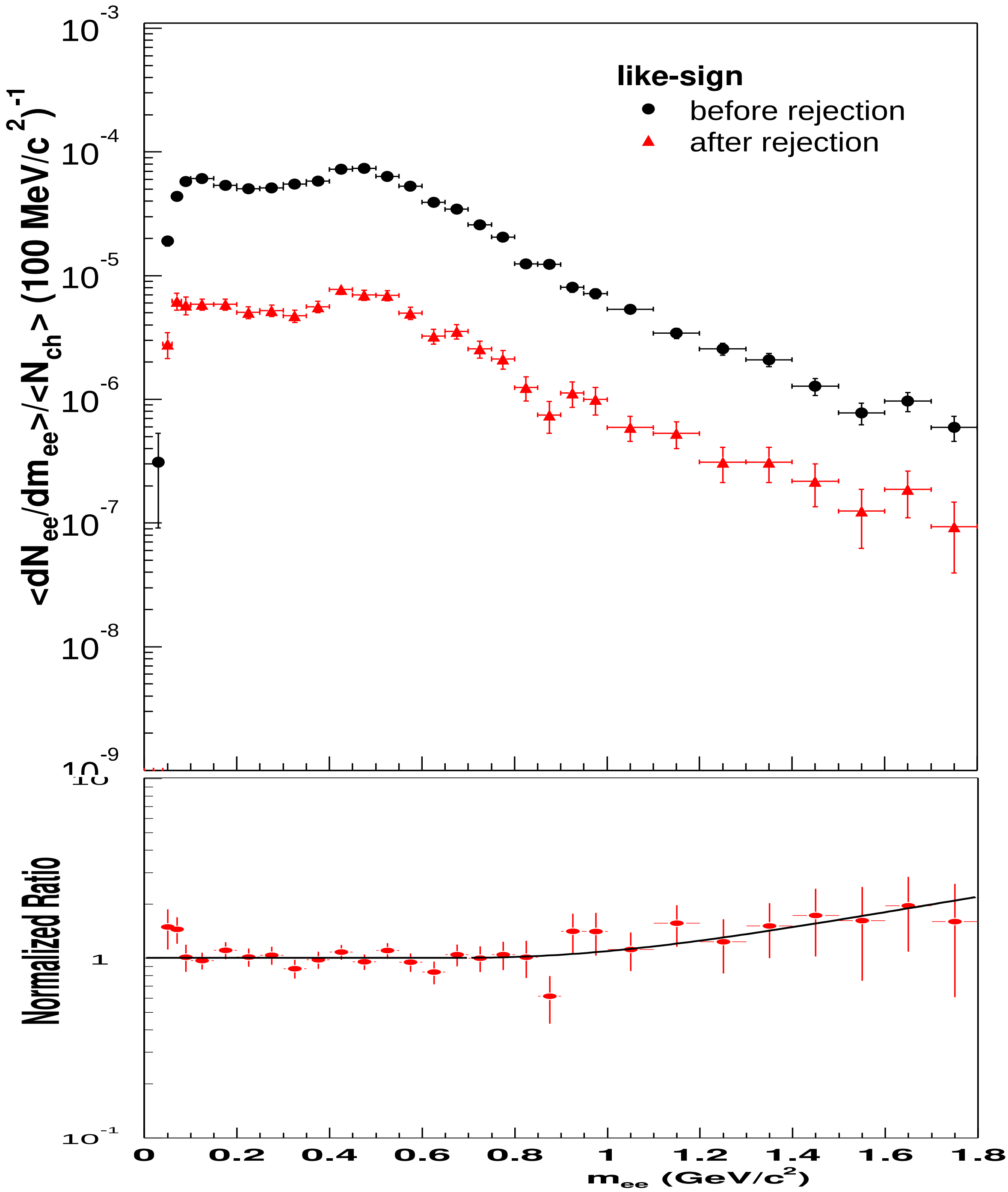


Figure 3.44: *Upper panel: Invariant-mass spectra of like-sign pairs before (black circles) and after (red triangles) applying the last 3 rejection steps in Fig. 3.36, showing the stability of the shape for the two distributions. The normalization of the ordinate is described in chapter 5. Lower panel: Ratio between normalized pre-rejection and after-rejection background vs. invariant mass; the normalization is done in the region 0.2-1 GeV/c$^2$, requiring a factor of 10.14±0.3.*

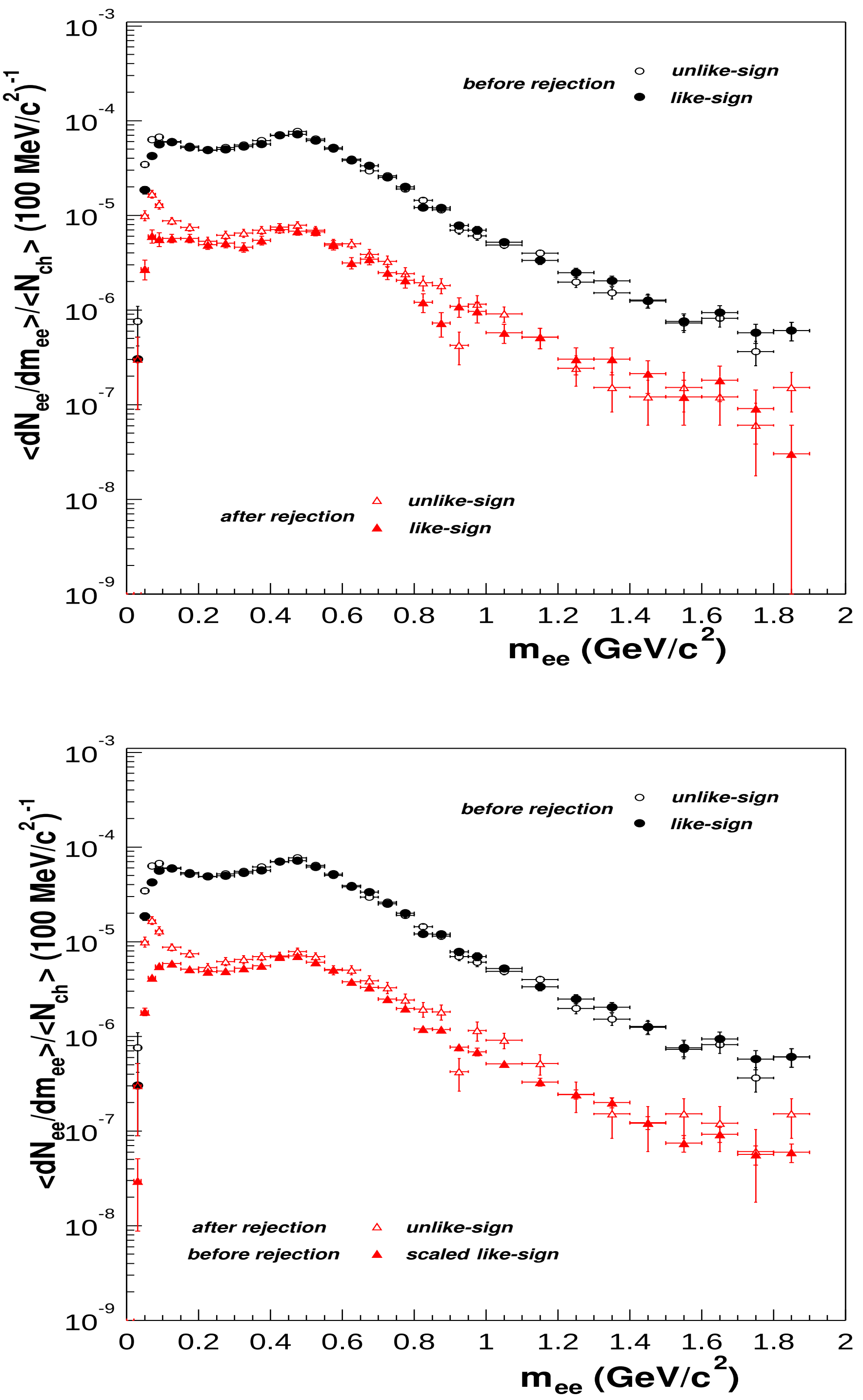


Figure 3.45: *Upper panel: Invariant-mass spectra of unlike-sign and like-sign pairs with partial rejection (black circles) and after full rejection (red triangles). Lower panel: Mass spectra of unlike-sign and like-sign pairs with partial rejection (black circles), and of unlike-sign pairs after full rejection together with the rescaled like-sign pairs with partial rejection (red triangles). The normalization of the ordinate is described in chapter 5.*

bin-to-bin errors are already quadratically small compared to those of $N_{+-}$. The corresponding mass spectra of the like-sign combinatorial background before and after the last 3 rejection steps of Fig. 3.36 are compared in Fig. 3.44. It is gratifying to see that the shape is nearly identical, including the structure in the region $<$0.4 GeV/c$^2$, due to the single-electron transverse momentum cut $p_t \geq$200 MeV/c (a use of the even higher-statistics background *before* the $p_t$-cut is clearly excluded). The ratio between the two spectra is shown in the lower part of Fig. 3.44, where the normalization is done in the region 0.2-1 GeV/c$^2$. The normalization factor required to conserve the integral of the post-rejection background (used then for rescaling before subtraction) is 10.14$\pm$0.3; the associated error, discussed in section 5.3, is also quadratically small compared to the bin-to-bin errors. In the mass region $\geq$1 GeV/c$^2$, the normalized ratio increasingly deviates from 1, somewhat similar to, but more so than in the 1996 procedure. The corresponding fit function does actually only affect one bin in the mass spectra to be shown later, namely that of the $\phi$-region.

To assess the improvements obtained for the like-sign combinatorial background in direct comparison with the unlike-sign pairs, all relevant spectra, with partial rejection (only $p_t$- and TPC $dE/dx$ cut) and with full rejection, are summarized in Fig. 3.45. As is to be expected, no significant difference between unlike- and like-sign pair spectra exists for the partial-rejection case, while with full rejection, in particular in connection with the rescaled partial-rejection background, a clear excess of unlike-sign pairs is seen throughout the whole mass range.

# Chapter 4

# Monte Carlo Simulations

The detailed properties of the individual detectors of the CERES spectrometer like geometry, materials, known deficiencies etc., have been implemented in the GEANT detector simulation package. For certain corrections of the multiplicity distribution and, in particular, for the understanding of pair efficiency and rejection on an absolute level, MC simulations are indispensable. The package simulates the interactions of particles and photons with the detector material like energy loss, multiple scattering, generation of Cherenkov photons, etc. Simulations are done by generating particles from a known source with well known decay kinematics. The trajectories of these particles are traced through GEANT [57] including all modifications due to multiple scattering, hadronic interactions, deflection in the magnetic field etc. Moreover, the complete events need to be generated in the proper background environment. However, a realistic simulation of the background is very difficult. Therefore, the MC is used in “overlay mode”: particles from a known source are simulated by the MC code and then overlayed onto real events from experimental data. The information of all detector effects like limited geometrical acceptance, tracking efficiency, finite momentum resolution, etc. has to be simulated in the proper way. Indeed, to get correct results, the Monte-Carlo simulations have to resemble the data in all details. Since the analysis cuts are applied in an identical way to data analysis and to MC simulations, all quantities like $\theta$, $\phi$ distributions of the tracks, matching between detectors, hit amplitude distributions in all detectors etc. need to have the proper description in MC.

## 4.1 Detector Simulations

### 4.1.1 Simulation of the SIDC Detectors

As for all detectors, the parameters of the SIDC-detector simulation have to be tuned in a way to achieve the best description of the data. This implies to compare the reconstructed tracks from the MC output to the reconstructed SIDC tracks from real data in all their properties. The first comparison to be discussed concerns the amplitude distribution $dE/dx$ of the hits in the two SIDC’s. Fig. 4.1 shows a strong discrepancy between the $dE/dx$ distribution measured from the data and the one obtained from the original version of GEANT. The width of the MC Landau distribution is found to be too narrow, and the tails in the small $dE/dx$ region visible in the data are not described in MC. The poor description of the $dE/dx$ distribution by the MC also leads to a discrepancy between data and MC in the specific rejection factor connected to the 2-dimensional $dE/dx$-cut (see section 3.5.2 and Fig. 3.25); this is illustrated in Fig. 4.2.

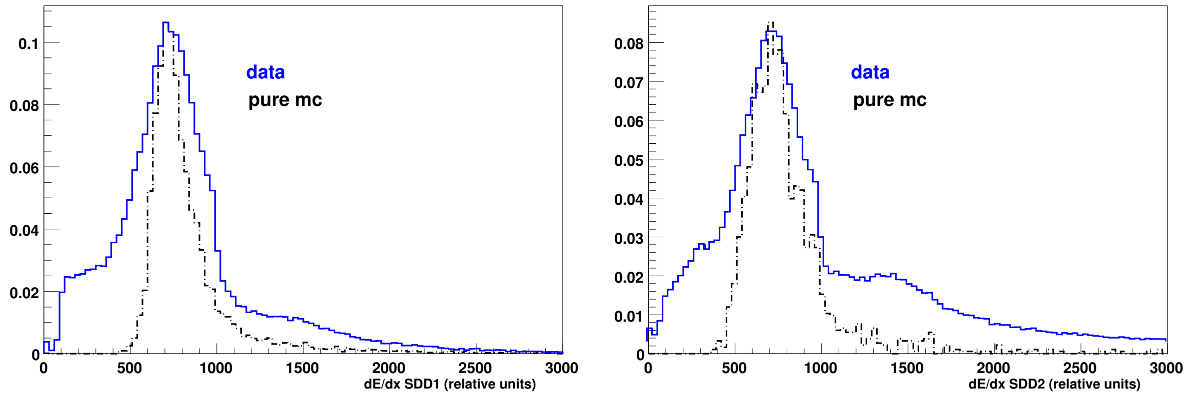


Figure 4.1: *Comparison of the $dE/dx$ distributions between data and MC for SIDC1 (left panel) and for SIDC2 (right panel), using the initial version of the GEANT simulations.*

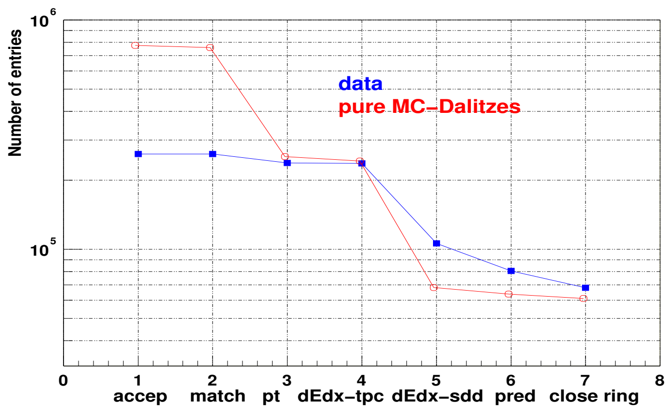


Figure 4.2: *Comparison of rejection factors between data and MC for the $dE/dx$-cut of the SIDC's, using the initial version of the GEANT simulations. In contrast to Fig. 3.36, the $dE/dx$-cut of the TPC is already contained in the first 3 steps along the abscissa.*

The MC was therefore modified in the following way. In the first step, the known permanently dead anodes (18 in SIDC1 and 25 in SIDC2) including their detailed map in the $\phi$ direction were included in the MC. However, the scanned dead channels in both SIDC detectors lead to an efficiency reduction of only 5%, leaving still $95\%$. In the next step, other quantities influencing the amplitude, width and overall shape of the $dE/dx$ distribution were tuned, namely the gain of the electronics, the noise of the readout electronics and diffusion along the drift path. The results of including these steps in the simulations are shown in the Fig. 4.3.

Obviously, there is still a discrepancy between the two distributions in the region of small $dE/dx$. Just using information about permanently dead anodes apparently is not sufficient to describe the observed SIDC track reconstruction efficiency, the proper shape of the Landau $dE/dx$ distributions and the proper rejection factor. It should also be recalled from section 3.31 that the low tails of the $dE/dx$-distribution are intimately connected to the problem of artificial hit splitting. Two ways were considered to cure the remaining problems: randomly adding further "dead anodes", and randomly adding "dead cells" in time bin direction. The first one was finally used. Specifically, adding to the map of the known permanently dead anodes in SIDC1/2 an additional 9% in SIDC1 and 4% in SIDC2 at random, the result is a realistic description of the $dE/dx$ distribution (Fig. 4.4), and the rejection factor of the double $dE/dx$-cut from the MC now agrees with that from the data (Fig. 4.5).

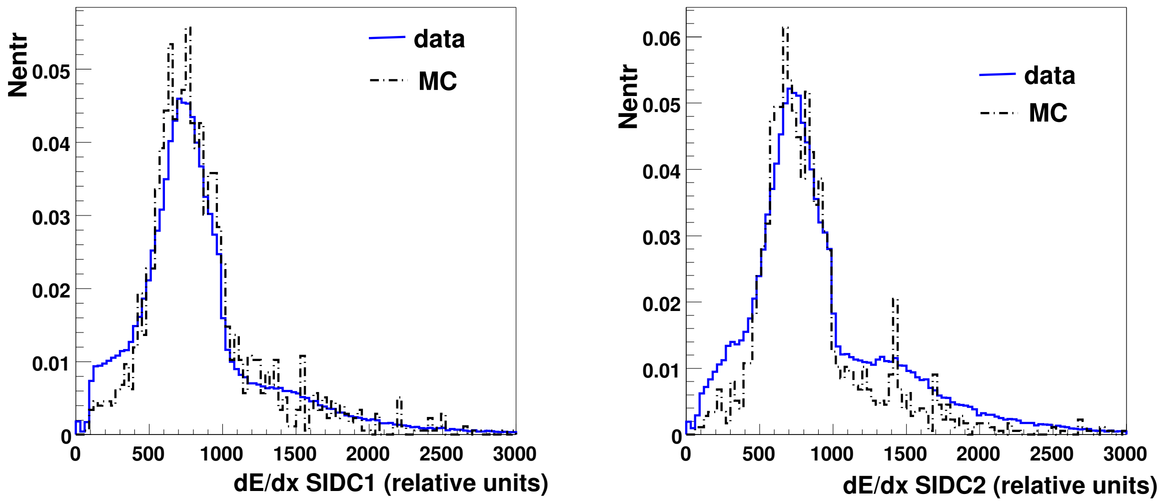


Figure 4.3: *Comparison of $dE/dx$ distributions for data and MC after inclusion of known dead anodes, tuning electronic noise and gain for SIDC1 (left panel) and for SIDC2 (right panel).*

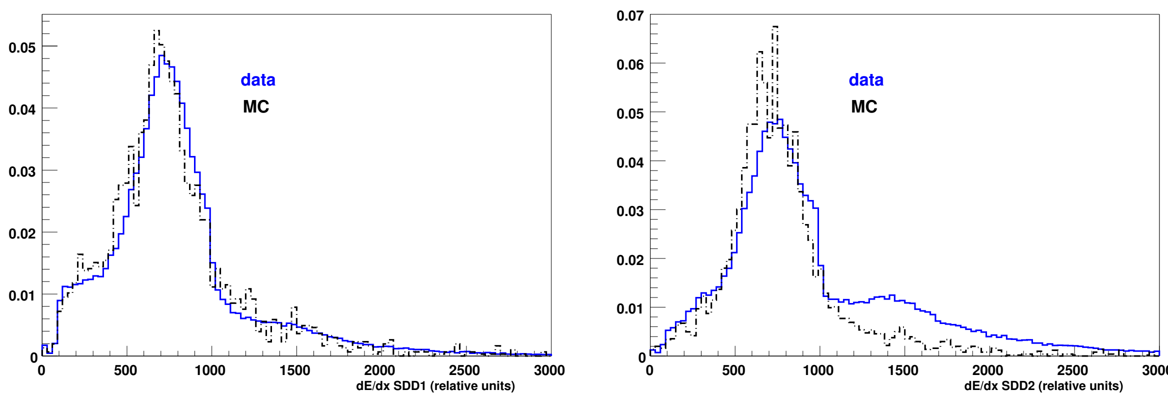


Figure 4.4: *Final comparison of $dE/dx$ distributions between data and MC for SIDC1 (left panel) and for SIDC2 (right panel) after implementation of all improvements (see text).*

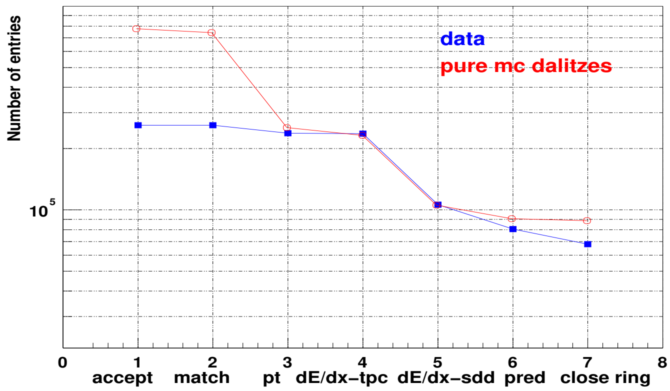


Figure 4.5: *Final comparison of rejection factors between data and MC for the $dE/dx$ cut of the SIDC's after implementation of all improvements (see text). In contrast to Fig. 3.36, the $dE/dx$-cut of the TPC is already contained in the first 3 steps along the abscissa.*

However, the observed track efficiency from the Monte Carlo is found to be still on the high level of $88\%$, independent of $dN_{ch}/d\eta$. The main reason is that the local dead anodes together with the additional dead anodes put in at random have only a small influence on the efficiency as long as they are isolated, i.e. as long as the immediate neighbors of dead anodes are alive. The final MC results discussed in section 4.2 are therefore downward-corrected by a factor of $0.76/0.88$ to be consistent with the experimentally determined overall SDD track efficiency of $0.76$ (see section 3.3.3).

### 4.1.2 Simulation of the RICH Detectors

In the RICH detectors, the simulated effects in the MC include chromatic aberrations, mirror quality and multiple scattering in the radiators, and diffusion in the conversion zone, gas gain and noise of the readout electronics in the UV detectors [23].

As already mentioned in section 3.4.2, the overlay mode of the MC simulations results in an overall track efficiency of 0.94 for the combined use of RICH1 and RICH2, using idealized high-$p_t$ tracks in full ring acceptance (162<$\theta$<240 mrad). The efficiency is found to be lower for realistic simulations of the $\phi$-meson, 92$\%$, and still lower for tracks from $\pi^0$-Dalitz pairs (with mostly overlapping rings), about 86$\%$. For the (larger) nominal acceptance of the spectrometer of $\Delta\eta$=0.53 (142<$\theta$<240 mrad), the values drop further: averaged over the acceptance to 90$\%$ for the $\phi$ and to 83.5$\%$ for Dalitz pairs. This is mostly due to the Hough-amplitude cut which is not sufficiently lowered at the inner edge of the spectrometer to follow the loss of UV photons per ring, once rings are partially cut by the acceptance. The remaining improvements compared to the 1995/96 analysis with the separate use of the RICH detectors are still remarkable: compared to the global 0.70 found there for $\pi^0$-Dalitz pairs (other sources were not investigated), they amount to factors of 1.2 and 1.3 for $\pi^0$-Dalitz pairs and the $\phi$, resp., on the track level, and 1.4 and 1.65, resp., on the pair level.

### 4.1.3 Simulation of the TPC

Principal MC simulations of the CERES TPC have a long history [59]. Fine-tuning of all relevant quantities characterizing the detector system to describe the data as closely

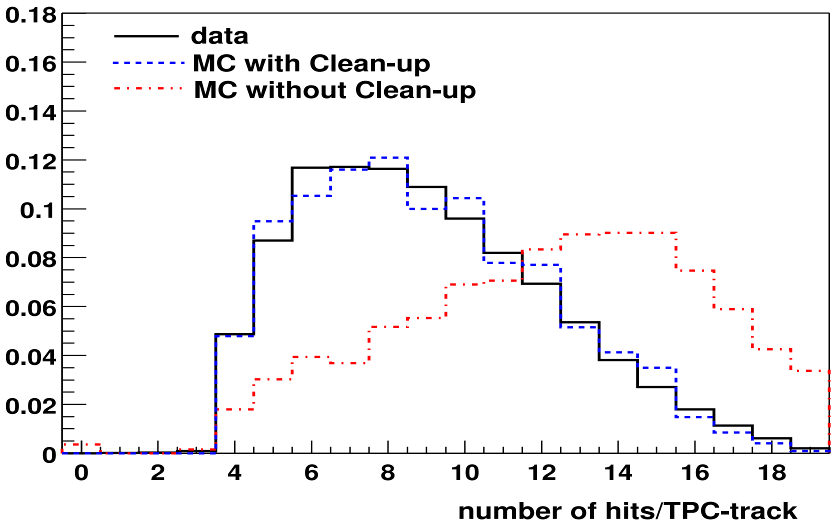


Figure 4.6: *Distribution of the number of TPC hits per track for data (solid), MC without(red dashed-dotted) and MC with clean-up procedure(blue dashed line).*

as possible has also occurred since some time [60, 61], though all within the limits imposed by the fast "zero-order" approach chosen for 1999 in contrast to 2000 (see

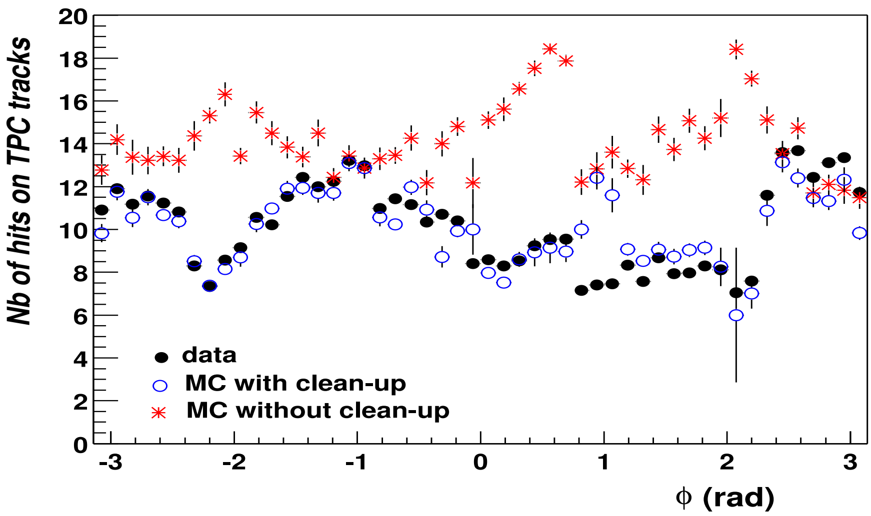


Figure 4.7: *Distribution of the mean number of hits/TPC-track vs. azimuthal angle for data (full circles), for MC without (stars) and for MC with clean-up procedure (open circles).*

discussion in sections 3.4.3, 3.4.4). The electron analysis described in this work has greatly benefitted from these efforts. The only variable requiring additional tuning (by about 20%) was the overall gain, controlling the center-of-gravity of the $dE/dx$-distribution. The electron-identification cut used in the data analysis to suppress fake pions had to be precisely simulated also in the MC to assess the electron-efficiency losses at higher $p_t$ associated with this cut (see section 4.2.2).

As discussed already before, the very instable TPC operation in 1999 with (permanently changing) regions of faulty electronics, whole sectors missing etc. drastically deteriorated the overall track efficiency of the TPC. The clean-up procedure for these defects as used in the data analysis had to be properly incorporated in the MC simulations to obtain final efficiency values anywhere near to reality [62]. The remarkable agreement between data and MC achieved for this particularly important aspect is illustrated in Figs. 4.6-4.8. The distribution of the number of hits/track in the TPC is shown in Fig. 4.6. While the unmodified MC simulations give a value of about ∼14, the modifications associated with the event-by-event clean-up procedure reduce this to only ∼9, in close agreement with the data. A similarly strong effect can be seen in the mean number of hits/track vs. azimuthal angle $\phi$ in the TPC (Fig. 4.7): without clean-up, the MC variations vs. $\phi$ are even out-of-phase with the data, while with clean-up, near-perfect agreement is seen.

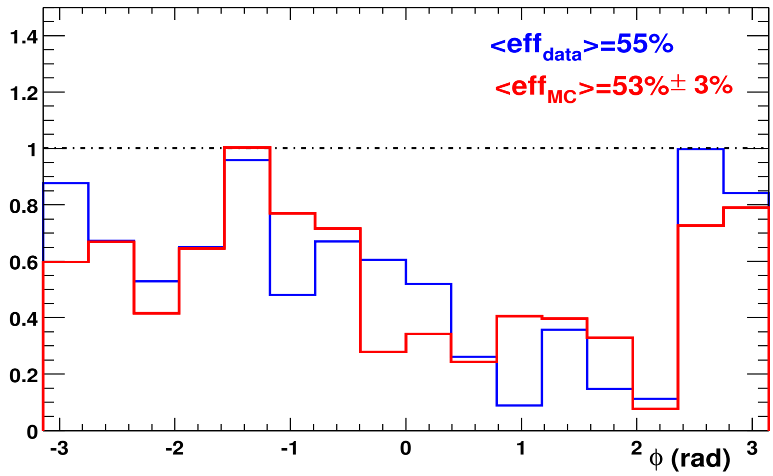


Figure 4.8: *The measured $\phi$-distribution of electron tracks (blue) compared to the $\phi$-distribution for $\pi^0$-Dalitz tracks from overlay-MC simulations (red line).*

The drastic influence of the defects in the TPC on the average track efficiency can be recognized in Fig. 4.8. With the arbitrary normalization of the efficiency of sector $No$. 1 (second-last on the right) to 1, the relative track efficiency averaged over $\phi$ is found to be 0.55 for the data, implying losses by a factor of $>$3 in pair efficiency compared to a perfectly functioning TPC! The overlay-MC simulations with $\pi^0$-Dalitz-pairs, using a representative sample of data files across the run (but, of course, not the full run), give a value of 0.55±0.03, in good agreement with the data and in perfect support of the corrections of the clean-up procedure.

## 4.2 Pair Reconstruction Efficiency

To allow for a quantitative comparison with physics sources, the measured $e^+e^-$ pair spectra in invariant mass, transverse momentum or other variables have to be corrected for experimental pair efficiency on an absolute level. This implies a Monte Carlo simulation of the whole CERES spectrometer, including the detailed properties of the individual detectors discussed in the previous section, total track reconstruction, particle identification, low-mass background rejection etc. Again, the technique of overlaying pairs with known decay kinematics onto real experimental events is used (1 pair/event), always under condition of the full analysis chain and the usual analysis cuts, i.e. acceptance $2.11<\eta<2.64$, pair opening angle $\Theta_{ee}>35$ mrad, single-electron transverse momentum $p_t>200$ MeV/c etc. The pair efficiency is then, in principle, obtained as the number ratio of the reconstructed pairs to the input pairs.

In practice, given the low pair efficiency of order 3-4$\%$ in the 1999 situation, a direct evaluation of pair efficiency in MC simulations with sufficient statistical accuracy has proven to be completely unrealistic. A different approach has therefore been followed. Single track efficiencies $\epsilon^{track}$ are determined for a number of sources from $\pi^0$- and $\eta$-Dalitz- to $\omega$ and $\phi$ resonance decays to study the sensitivity to different kinematical properties like mass, momentum, pair opening angle etc, but ignoring pair acceptance, i.e. requiring only one track of a pair to be in the acceptance. To zero order, the pair efficiency is then given by

$$\epsilon_{ee}^{pair} = \epsilon_e^{track1} \cdot \epsilon_e^{track2}, \tag{4.1}$$

independent of the character of the source. All figures of this section containing pair efficiencies (Fig. 4.12-4.14) have been evaluated in this way, including the final functional dependence on $dN_{ch}/d\eta$ (Fig. 4.17).

To higher order, subtle source dependences do exist, due to potentially different dependences on $dN_{ch}/d\eta$ and the single-track phase space parameters $p$,$\theta$,$\phi$. The more important of these, $dN_{ch}/d\eta$ and $\theta$, lead to deviations of the true value of $\langle\epsilon_{ee}^{pair}\rangle$, averaged over the distributions in $dN_{ch}/d\eta$ and $\theta$, from the above formula

$$\langle\epsilon_{ee}^{pair}\rangle = \langle\epsilon_{ee}^{track1} \cdot \epsilon_{ee}^{track2}\rangle \cdot C(m_{ee}, ...) \tag{4.2}$$

where the correction function $C$, depending on the specific parameters of the source and its specific dependence on $dN_{ch}/d\eta$, is still of order 1, but can deviate from 1 by up to about 10$\%$. This has been investigated with proper folding procedures outside the MC chain (but using all ingredients from MC) and will be discussed in some detail in subsection 4.24. Ultimately, the averaging is actually done on $1/\epsilon$ to be consistent with the upward correction of the data (see also 4.24).

Instead of applying a properly evaluated global efficiency correction with $\langle\epsilon_{ee}^{pair}\rangle$ as done in this work, a different approach has been taken in the 1996 data analysis. The data were corrected *event-by-event* on the level of the *primary* unlike-sign and like-sign pair samples $N_{+-}$ and $N_{\pm\pm}$, using weights defined by

$$w = \frac{1}{\epsilon^{track1}(N_{ch}, \theta_1)} \cdot \frac{1}{\epsilon^{track2}(N_{ch}, \theta_2)} \tag{4.3}$$

where the functional dependences of $\epsilon^{track}$ on $dN_{ch}/d\eta$ and $\theta$ were determined from overlay-MC in the same way as in this work. Unfortunately, as was only recognized recently, the (implicitly done) transformation of an efficiency matrix in $N_{ch}$ and $\theta$, assessed with good MC statistics, into another multi-dimensional efficiency matrix in the variables of interest ($m_{ee}$ etc), using the limited-statistics data themselves, introduces statistical fluctuations of the elements of the correction matrix which are inevitably of the same order as the statistical fluctuations of the data themselves. In view of the fact that the whole higher-order corrections expressed in $C = C(m_{ee}, ...)$ are *smaller* than the additional fluctuations introduced by the event-by-event correction procedure, this approach is obviously inappropriate and has therefore not been used in this work (and may have to be discarded in retrospect in the 1996 data analysis also).

### 4.2.1 Basic Results for $\pi_0$-Dalitz Pairs

Close pairs from $\pi^0$-Dalitz decays play the role of a benchmark in the efficiency discussion. They are the only known $e^+e^-$ source positively identified in the CERES experiment (at least at present), their $S/B$ ratio is favorable (of order 1/1), their relative efficiency vs. $dN_{ch}/d\eta$ can be taken from the data and, after normalization, directly compared to the corresponding overlay-MC results (which are on an absolute level), and finally even their absolute level (which includes the $\eta$-Dalitz part for $m$<200 $MeV/c^2$) can be taken from the data and compared to MC (subject to the uncertainty of an additional “direct-source” contribution to the data in the Dalitz region of unknown origin). The cuts selected for the following discussion are the usual ones used in the whole analysis, i.e. acceptance, $m$<200 $MeV/c^2$, $p_t$>200 MeV/c, with the exception that the opening-angle cut is reduced from >35 mrad to >25 mrad to increase the statistics both in the data and in the overlay-MC. The data situation will be discussed first.

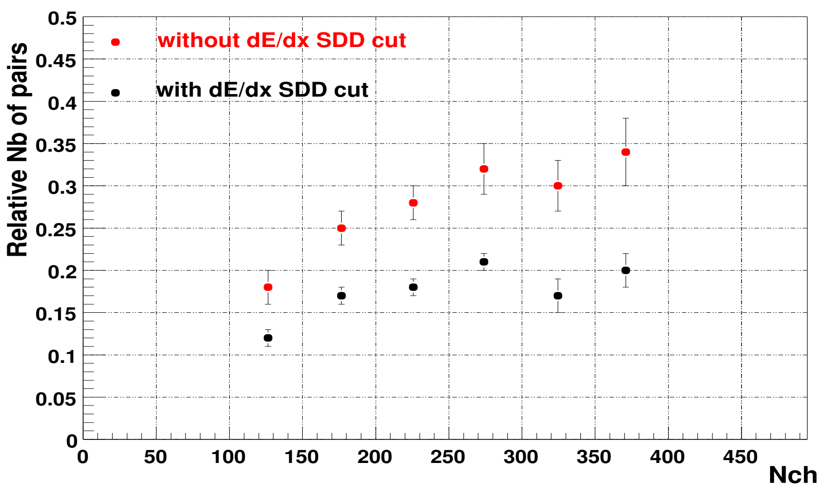


Figure 4.9: *Measured number of Dalitz pairs, normalized to the SIDC multiplicity distribution, for two different rejection cuts.*

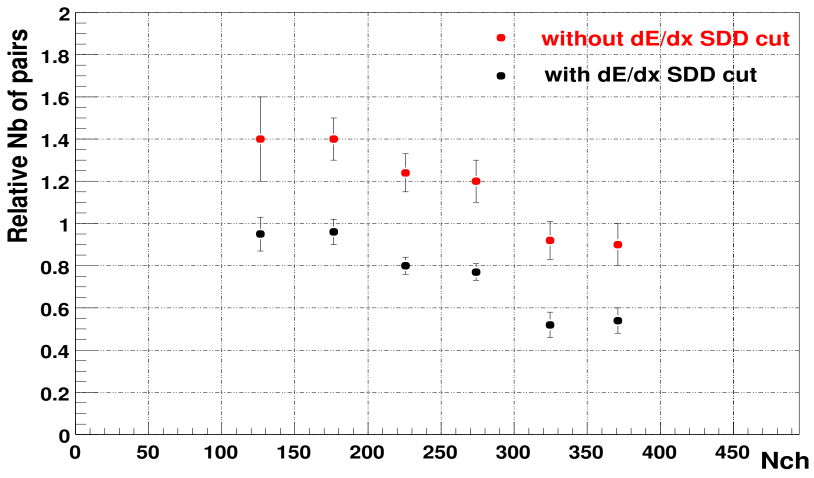


Figure 4.10: *Measured number of Dalitz pairs, normalized to the SIDC multiplicity distribution and the number of charged particles $\langle N_{ch} \rangle$ in the respective bin, for two different rejection cuts. The relative number of pairs defined in this way is proportional to the relative reconstruction efficiency.*

The normalized number of measured $\pi^0$-Dalitz pairs as a function of raw-data event multiplicity is shown in Fig. 4.9. The normalization is done by dividing the integral of measured Dalitzes in each bin of multiplicity by the number of entries in that bin. The comparison of the two data sets shows the strong influence of the SDD-$dE/dx$ rejection cut, leading to an efficiency loss by pile-up of pions in the large summation window of 10 mrad as described in the previous chapter 3. It is clearly visible in Fig. 4.9 that the probability of pion pile-up increases with multiplicity.

In the next step, the relative pair efficiency is determined as the number of Dalitz pairs normalized, in addition to the SIDC multiplicity, to the average number of charged particles $\langle N_{ch} \rangle$ in that bin to correct for the rise of Dalitz pairs proportional to multiplicity. The result is shown in Fig. 4.10. In the ideal case of no efficiency loss with multiplicity, both distributions would be flat. However, there are significant losses, and the effects of pion pile-up are stronger in the region of higher multiplicity as shown by the increasing relative differences between the two data sets; these differences are actually quantitatively described by the overlay-MC (see below).

A study similar to Fig. 4.10 has been done by using the open pair combinatorial background, i.e. the total like-sign pairs with $m_{ee}$>200 MeV/c$^2$. These have a quadratic dependence on charged multiplicity, and therefore the normalization of the differential rate of the open pair background has to be done relative to $\langle N_{ch} \rangle^2$ in each bin, in addition to the normalization to the number of events in that bin. The results are shown in Fig. 4.11. Again, no flat distributions are seen. Instead, the background suffers from similar efficiency losses as the Dalitz pairs, including the influence of the $dE/dx$ rejection cut (to ease the comparison between the two data sets, the strong reduction of the combinatorial background by a factor of 5, using the $dE/dx$ cut, is compensated by a corresponding upward multiplication).

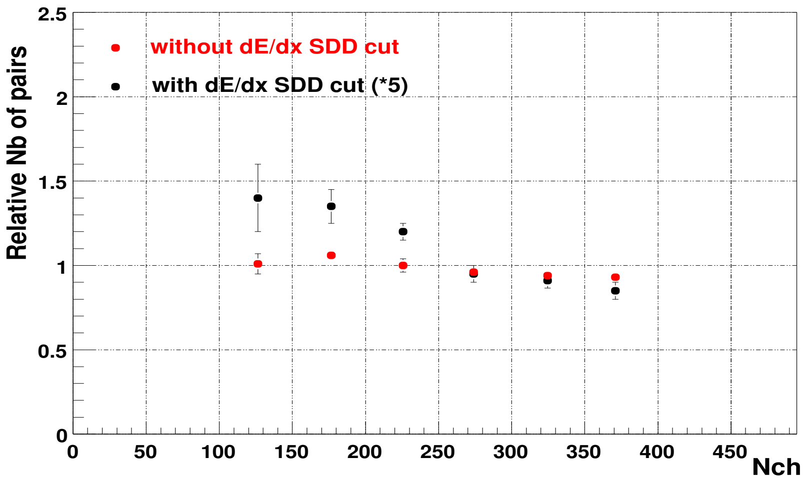


Figure 4.11: *Open-pair combinatorial background, normalized to the SIDC multiplicity distribution and the square of the number of charged particles $\langle N_{ch}\rangle^2$ in the respective bin, for two different rejection cuts. The relative number of pairs defined in this way is proportional to the relative reconstruction efficiency.*

The results on the *absolute* pair reconstruction efficiency vs. charged multiplicity, determined from the Monte Carlo simulations by overlaying $\pi^0$-Dalitz pairs onto real events, are shown in Fig. 4.12. The experimental events used for the overlay were selected from different parts of the run to avoid any bias due to subtle changes in the set-up. The pair efficiency is obtained as the square of the single track efficiency as discussed in detail above, ignoring in the evaluation of the track efficiency the need of a second partner in the acceptance. The results contain all rejection cuts, including the SIDC $dE/dx$ cut. It should be noted that the raw $N_{ch}$-scale, used in the MC studies shown in Fig. 4.12 (and Fig. 4.13), is shifted to slightly larger values of $N_{ch}$ compared to the raw-data scale in Fig. 3.6, because a symmetrical matching window between SIDC1 and SIDC2 has been used in the MC studies (see section 3.3.3). The value of the pair efficiency obtained from the fit to the MC points at the average multiplicity ($\langle N_{ch}\rangle$=236; $\langle dN_{ch}/d\eta\rangle$=216) is 3.95%±0.31%(stat).

The absolute pair reconstruction efficiency determined from overlay MC is compared in Fig. 4.13 to the experimental data points of Fig. 4.10 (including the SIDC $dE/dx$-cut), normalized in a way to fit the MC line on average. It is very satisfactory to see that the slope of the decrease of the efficiency with event multiplicity shows, within the errors, perfect agreement between data and MC.

### 4.2.2 Basic Results for High-Mass Pairs

Even on the level of track efficiencies, there is a certain danger to blindly carry over the results from $\pi^0$-Dalitz pairs to higher-mass pairs. The phase space population is indeed different. For Dalitzes, rings always overlap, tracks are close together, the average $\langle p_t\rangle$

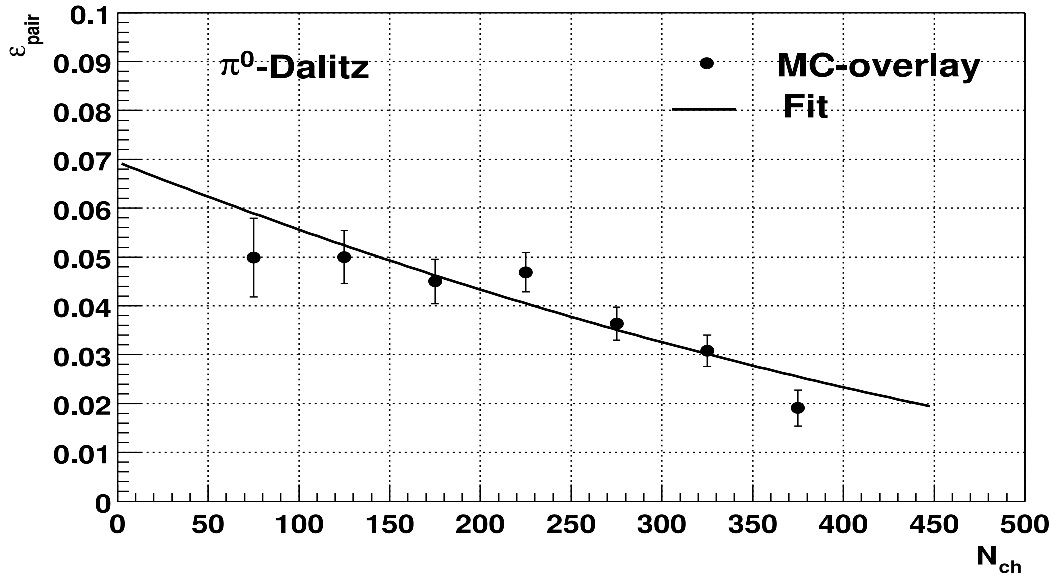


Figure 4.12: *Absolute pair reconstruction efficiency vs. multiplicity determined from MC studies, using $\pi^0$-Dalitz pairs overlayed onto real events. The line drawn is a fit to the MC points.*

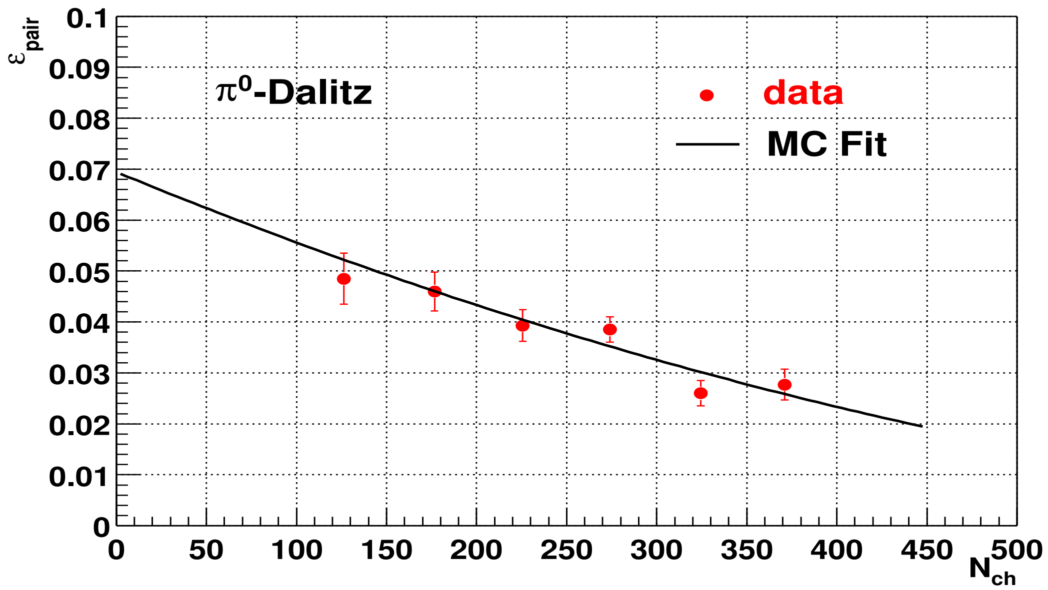


Figure 4.13: *Absolute pair reconstruction efficiency vs. multiplicity from overlay-MC (full line from Fig. 4.12) compared to the properly normalized experimental data points from Fig. 4.10, including the SIDC $dE/dx$ cut. Very good agreement is seen between MC and data in the slope of the decrease of the efficiency with event multiplicity, ranging from $\sim$6% at low $N_{ch}$ to $\sim$3% at high $N_{ch}$.*

is abnormally low: effects which altogether lower efficiency. High-mass pairs, on the other hand, are always open and have larger $\langle p_t \rangle$, both favorable for efficiency, but just because $\langle p_t \rangle$ is larger, they are also more sensitive to the TPC $dE/dx$-cut aiding particle

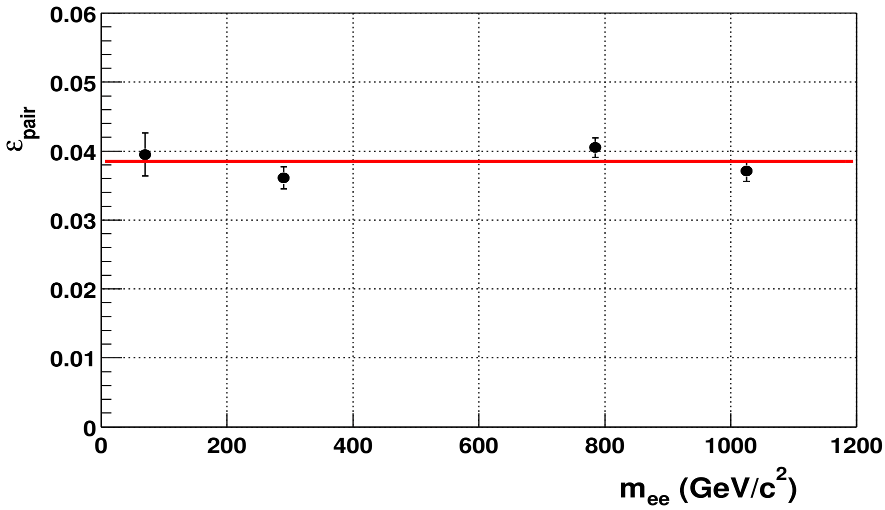


Figure 4.14: *Absolute pair reconstruction efficiency as a function of invariant mass, studied in MC by overlaying sources with known properties from the hadronic decay cocktail ($\pi^0$, $\eta$, $\omega$, $\phi$) onto real events. The values plotted correspond to $\langle N_{ch}\rangle$=236 ($\langle dN_{ch}/d\eta\rangle$=216).*

identification in 1999 (equivalent to the "pion-cut" on rings imposed on 1996 data). To obtain the differential behaviour of the absolute pair efficiency as a function of mass in addition to $\pi^0$-Dalitz pairs, $\eta \to e^+e^-\gamma$ Dalitz pairs with mass $m$>200 MeV/c$^2$ and two body decays $\omega \to e^+e^-$ and $\phi \to e^+e^-$ have been used. In all cases, track efficiencies were studied vs. multiplicity as described for the $\pi^0$-Dalitz case in the previous subsection. The outcome of this study, taken again at the average value of the multiplicity distribution ($\langle N_{ch}\rangle$=236, $\langle dN_{ch}/d\eta\rangle$=216), is shown in Fig. 4.14. The flat behaviour is assuring, but somewhat unexpected; it reflects the cancellation, by chance, of a number of different influences. The mass-averaged pair-efficiency value corresponding to Fig. 4.14 is 3.85$\%\pm$0.08$\%$(stat.). It is important to add that the slopes of track efficiencies vs. multiplicity were found, within errors, to be identical in all 4 cases.

As was explained in detail in sections 3.4.4 and 3.4.5, the main electron identification done by the double RICH system is further improved by using the characteristic energy loss of electrons in the TPC. To identify individual particles by $\langle dE/dx\rangle$, the resolution width must be smaller than the difference between the mean values. Separation of the average energy loss of an electron from that of other particles such as pions, kaons etc. is momentum dependent. At the lowest momenta (see Fig. 4.15) the pions have a greater ionisation loss than the electrons which are already in the saturation region of the Fermi plateau. The pions cross the electron band at $\sim$ 150 MeV ($p_t$≈30 MeV) and reach the minimum at about 300-400 MeV/c. The difference between the minimum and the Fermi plateau is about a factor of 1.6. Therefore, in the low-momentum region, the separation of electrons from other particles is very powerful. Conversely, in the region of the average momenta populated by the resonances $\phi$, $\omega$ ..., the separation between electrons and pions in the relativistic rise starts to be increasingly difficult. Moreover, as discussed in detail in section 3.4.4, the experimental resolution width of the $\langle dE/dx\rangle$ distribution is rather poor, due to the small average hit number of the TPC tracks in 1999. Therefore, the electron-identification cut line

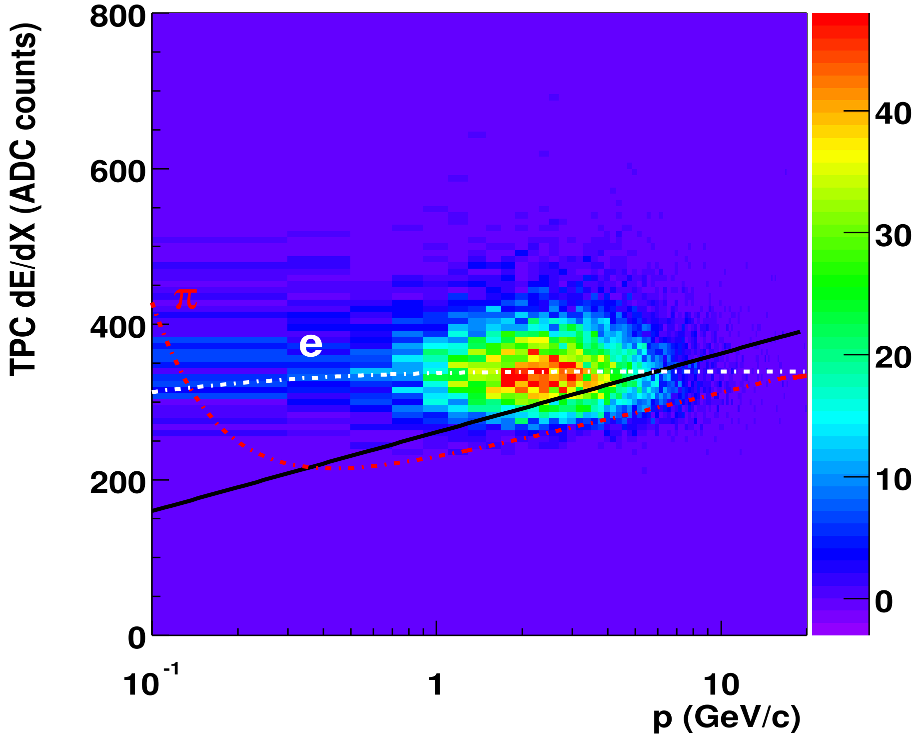


Figure 4.15: *A contour plot of the $dE/dx$ distribution in the TPC versus momentum for electron tracks produced in $\phi$ decays (pure MC). The gliding cut used in the analysis affects the efficiency of the high momentum electrons. The dependence of the average energy loss on momentum for electrons and pions (Bethe-Bloch) is included for orientation.*

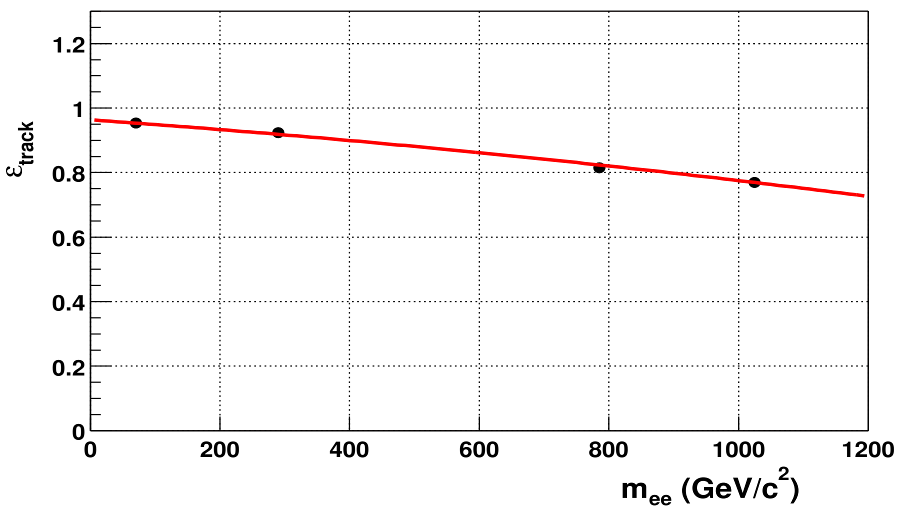


Figure 4.16: *Influence of the TPC $dE/dx$-cut on the relative electron track efficiency, studied in MC-simulations by using different sources from the GENESIS generator ($\pi^0$, $\eta$, $\omega$, $\phi$).*

discussed in section 3.4.5 does remove a lot of pions, but also removes part of the high momentum electrons. This is illustrated in Fig. 4.15 for the example of $\phi \to e^+e^-$, containing the electrons with the highest average transverse momenta in the mass spectrum. For these simulations, sources again from the GEANT decay cocktail have been used, but in a pure MC-(non-overlay) mode. Quantitatively, as shown in Fig. 4.16, the track efficiency loss for the $\phi$ is about 20%, monotonically less so for smaller masses (equivalent to smaller average transverse momenta).

To obtain the flat behaviour of the overall pair efficiency vs. mass shown in Fig. 4.14, a compensation of the results of Fig. 4.16 by effects increasing the efficiency with mass is required. These have been located in the detailed response of the double-RICH and, somewhat surprisingly, of the TPC to the different sources (see sections 4.12 and 4.13 above), while the SIDC-system turned out to be completely insensitive with a stable efficiency value of 0.88 through the mass range. A summary of these findings is contained in the next section (Table 4.1).

### 4.2.3 Summary of Basic Results

The outcome of the overlay-MC studies described in the previous two subsections is summarized in Fig. 4.17. The abscissa has been converted from raw-data $N_{ch}$ to

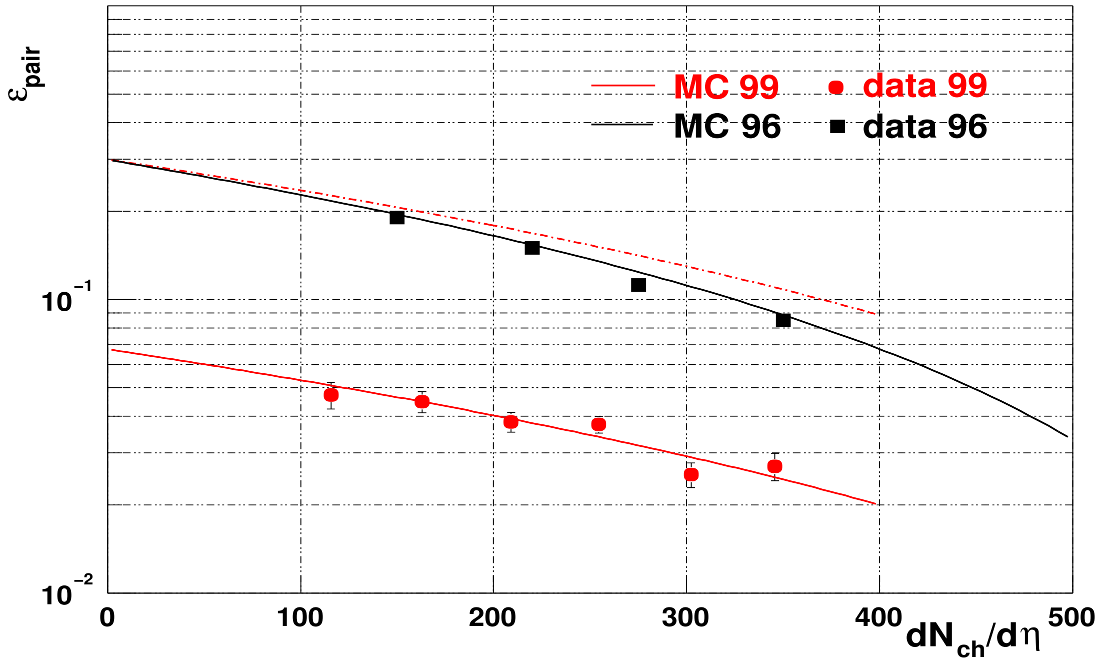


Figure 4.17: *Pair reconstruction efficiency vs. charged multiplicity density from overlay-MC simulations, taking the average of 4 simulated sources ($\pi^0$, $\eta$, $\omega$, $\phi$). For comparison, the results from the 1996 analysis [22, 20, 21] are included in the plot. To help that comparison, the 1999 results are also shown rescaled such as to have the same value at $dN_{ch}/d\eta$=0 (dashed line).*

$dN_{ch}/d\eta$ (compatible with Fig. 3.11), and the efficiency values now correspond to the average over the 4 simulated sources (with identical slopes vs. multiplicity). The experimental data points for $\pi^0$-Dalitz pairs have correspondingly been renormalized. For comparison, Fig. 4.17 also shows the efficiency obtained in overlay-MC simulations for $\pi^0$-Dalitz pairs from the 1996 analysis [22, 20, 21]. While the 1999 absolute efficiency values are much smaller, due to the defects of the TPC, the relative multiplicity dependence is seen to be less steep. This improvement is presumably connected to the superior pattern recognition of the combined RICH1/RICH2 analysis.

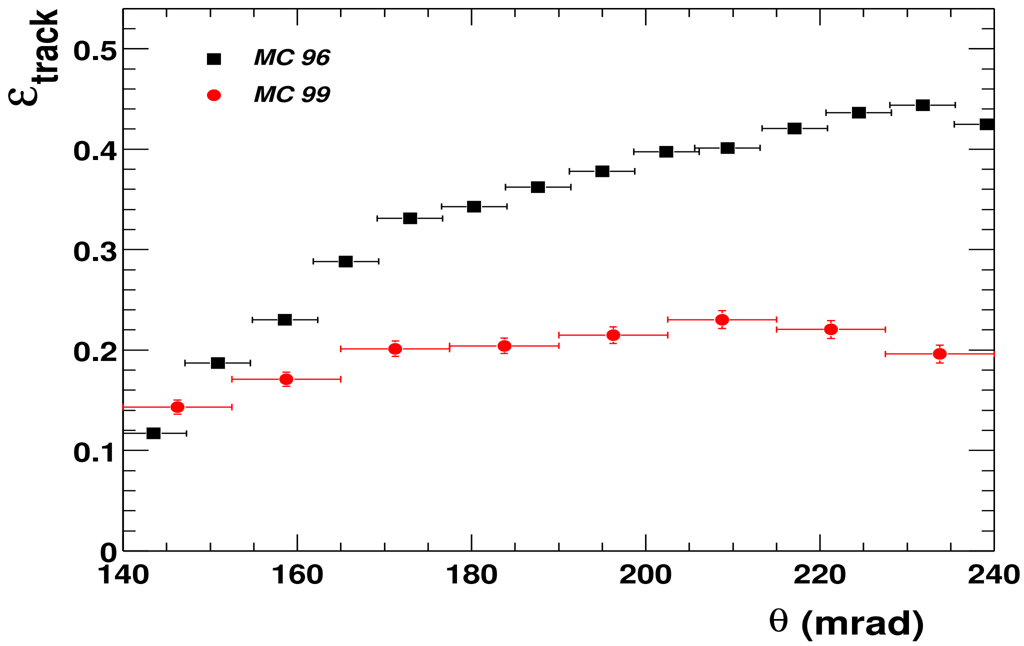


Figure 4.18: *Track reconstruction efficiency vs. polar angle $\theta$ from overlay-MC simulations, taking the average of 4 simulated sources ($\pi^0$, $\eta$, $\omega$, $\phi$). For comparison, the results from the 1996 analysis [22, 20, 21] are also shown. They span a much larger dynamical range (see text).*

The only other primary experimental variable in which strong variations of the efficiency occur, is the polar angle $\theta$. The overlay-MC results for the track reconstruction efficiency vs. $\theta$, again for the average of the 4 sources, are shown in Fig. 4.18. Other than in Fig. 4.17, $\epsilon_{track}$ has to be used, since $\theta$ refers to single electrons, and a pair efficiency can only be derived from $\epsilon_{track}(\theta)$ after folding over both partners of a pair (see below). Also different from Fig. 4.17, the primary MC points have been kept rather to show smooth fit lines. The comparison to the 1996 results [20, 21, 22] shows the dynamical range of the variation of efficiency with $\theta$ for the 1999 data to be much smaller, only a factor of 1.6 compared to nearly 4. The reason is the following. In the central part of the acceptance, both dependences are roughly proportional to $sin(\theta)$, reflecting the losses due to occupancy. Towards lower values of $\theta$, the additional losses due to a decreasing number of hits/ring for rings increasingly cut by acceptance are much less severe in 1999 than in 1996, because of the combined RICH1/RICH2 analysis and a gliding cut in the double-Hough amplitude at the acceptance boundaries in 1999. At the upper end of the $\theta$-range, the 1999 efficiency values flatten because of increasing losses of tracks in the TPC (tracks exiting the TPC before reaching its end, coupled to the small number of hits/track in 1999; see Fig. 4.6 above).

To get some feeling on how the overall efficiency is roughly understood, table 4.1

contains a summary of the efficiency values extracted from the data (where known) and from the overlay-MC simulations of the different detectors, always taken at $\langle dN_{ch}/d\eta\rangle$ =216. The MC-values of the detectors have been individually evaluated with the exception of the TPC, where the values are derived from the final MC results of the overall chain, using all other entries of table 4.1 as an input. Note as stressed before, that the overall MC results are rescaled by 0.76/0.88 to compensate for the incorrect MC value of the SIDC-system. Note also that all MC-entries have statistical errors. All in all, the understanding of the overall efficiency on the basis of the individual contributions is satisfactory.

| detector | | data track efficiency | MC track efficiency | |
|---|---|---|---|---|
| | | | $\pi^0$-Dalitz | $\phi$-res. |
| SIDC1/SIDC2 | | 0.76 (hadr. data) | (0.88) | (0.88) |
| SIDC rejection | | 0.84±0.10 | 0.79 | 0.79 |
| RICH | | | 0.835 | 0.90 |
| TPC | azimuthal distribution | 0.55 | | |
| | unpacking | 0.90 | | |
| | track effic.(idealized) | 0.90 | | |
| | polar distribution | 0.97(hadr. data) | | |
| TPC overall | | 0.43 | (0.42) | (0.46) |
| TPC $dE/dx$ cut | | | 0.95 | 0.77 |
| overall | | | 0.20 | 0.19 |

Table 4.1: *Track efficiencies at $\langle dN/d\eta\rangle$=216 for the individual detectors SIDC, RICH and TPC from studies based on data (where available) and from overlay-MC simulations. The SIDC MC values are too high. The TPC values are derived from the final MC results of the overall chain, using all other entries; they therefore contain the rest of other small influences like overall matching losses.*

### 4.2.4 Efficiency Folding: Higher Order Corrections

As discussed before, the final efficiency correction of the data requires the appropriate folding of the track efficiencies with the relevant probability distributions in the variables $dN_{ch}/d\eta$ and $\theta$ according to eq. (4.2).

#### $dN_{ch}/d\eta$-dependence of low-mass pairs

The probability distribution vs. $dN_{ch}/d\eta$ of pairs with mass $< 0.2$ GeV/c$^2$ is determined by the weights $w_i$

$$w_i = \frac{dN_i}{dN_{ch}/d\eta} \cdot (\frac{dN_{ch}}{d\eta})_i \tag{4.4}$$

where the $dN_i/(dN_{ch}/d\eta)$ are the entries of the multiplicity distribution, and the $(dN_{ch}/d\eta)_i$ reflect the fact that the number of Dalitz pairs is proportional to multiplicity (used throughout section 4.2 and iterated in Fig. 7.5 in the result chapter 7). In each bin of $(dN_{ch}/d\eta)_i$, the Dalitz *pairs* are measured as $N_i^{Dal} = \epsilon_i \cdot w_i$ where the $\epsilon_i$ are the pair efficiencies vs. $dN_{ch}/d\eta$ discussed above. The weighted efficiency correction is then given by

$$\langle \frac{1}{\epsilon_{pair}} \rangle = \frac{\sum_{i=1}^{n} \frac{1}{\epsilon_i} \cdot N_i^{Dal}}{\sum_{i=1}^{n} N_i^{Dal}} = \frac{\sum_{i=1}^{n} \omega_i}{\sum_{i=1}^{n} \epsilon_i \omega_i} \tag{4.5}$$

Using the MC-fit line from Fig. 4.17, $\langle 1/\epsilon_{pair} \rangle^{-1}$=3.6% is obtained. The difference to the value 3.85% taken at the average $\langle dN_{ch}/d\eta \rangle$=216 is -6%.

### $dN_{ch}/d\eta$-dependence of high-mass pairs

Both in the 1995-[18, 19, 23] and the 1996-[20, 21, 22, 23] data analysis, the number of high-mass pairs with m>0.2 GeV/c$^2$ is found to increase approximately with the square of the charged multiplicity, requiring

$$w_i = \frac{dN_i}{dN_{ch}/d\eta} \cdot (\frac{dN_{ch}}{d\eta_i})^2 \tag{4.6}$$

for the weights in the folding procedure. The resulting value for $\langle 1/\epsilon_{pair} \rangle^{-1}$ is 3.4%, i.e. lower by a relative 6% than for linear weighting. However, the 1999 data on the multiplicity dependence of high-mass pairs shown in Fig. 7.5 in the result chapter 7 have such large error bars that a multiplicity dependence steeper than linear cannot independently be deduced. Indeed, most of the statistics in Fig. 7.5 is concentrated in the central of the 3 multiplicity bins. Doing the folding on the basis of these data themselves yields the original low-mass value of 3.6%, but with increased error bars. An efficiency correction for high-mass pairs different from low-mass pairs on the grounds of their $dN_{ch}/d\eta$-dependence can therefore not be justified in the 1999 data analysis.

### $\theta$-dependence

Much of the variation of $\epsilon_{track}$ with $\theta$ is due to the occupancy increasing towards the inner edges of the acceptance. Care has therefore to be taken to avoid double-counting in correcting for the $\theta$- on top of the $dN_{ch}/d\eta$-dependence. Indeed, if all pairs would have tiny opening angles, a $\theta$-correction would *not* be required, because the averaging over $\theta$ in that limit (equivalent to eq.(4.1)) would automatically be contained in the $dN_{ch}/d\eta$-correction. An additional correction in $\theta$ is meant to be a *differential* correction, accounting for a possible *difference* in the single-electron $\theta$-weight distribution between closed low-mass pairs and open high-mass pairs.

A comparison between the polar-angle distributions of the single-electron tracks associated with the low-mass and the high-mass net signal as directly taken from the (uncorrected) data is shown in Fig. 4.19 (left panel). There seems to be a tendency, analogous to the 1996 data, for the high-mass tracks to be more forward-peaked than the Dalitz-tracks, but the errors are such that an explicit correction based on such marginal differences could hardly be justified. The combinatorial background, measured with much better statistics and shown in Fig. 4.19 (right panel), does not contain significant

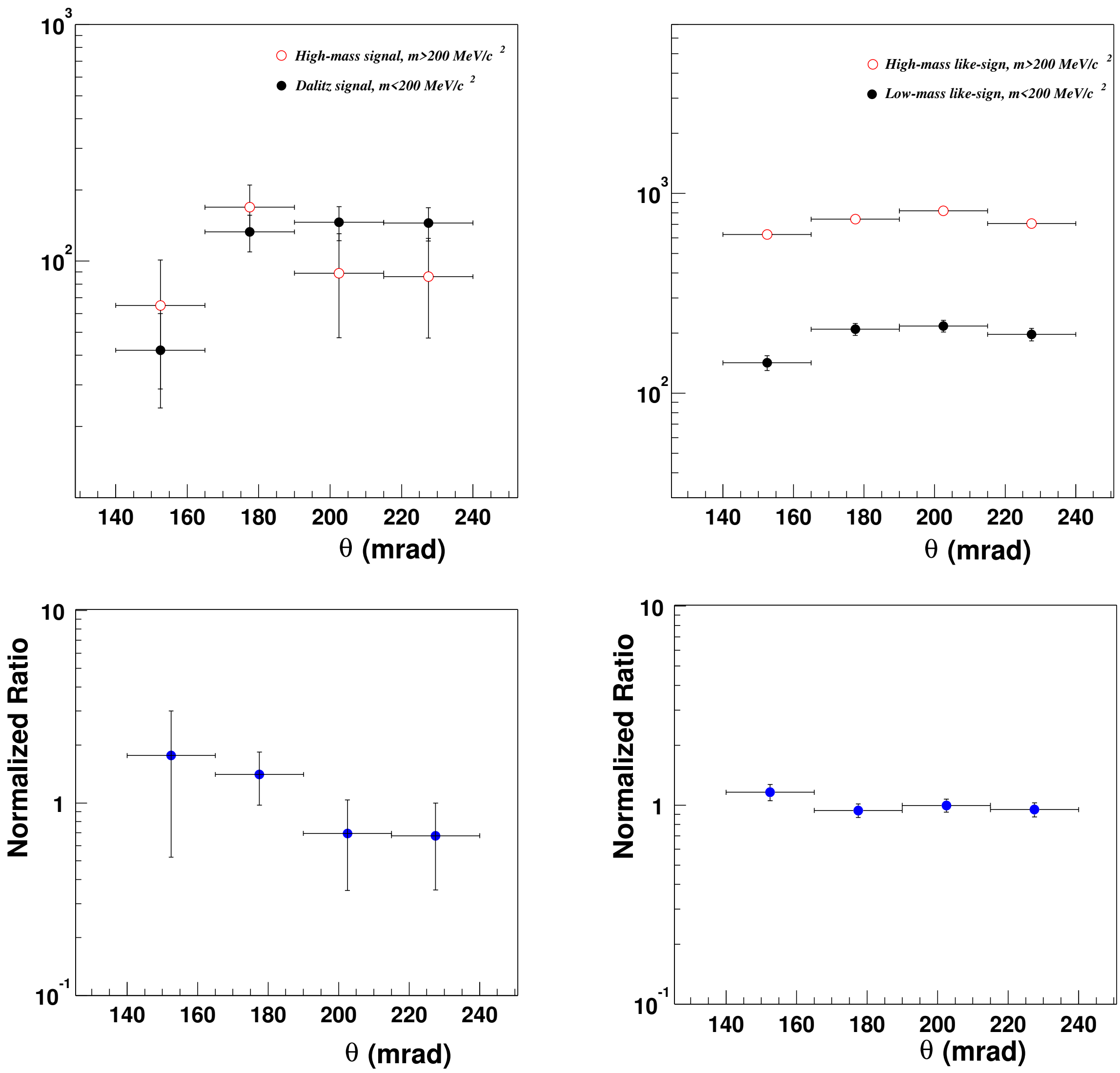


Figure 4.19: *Polar-angle distributions of the single-electron tracks for the net signal from high-mass ($m$>200 MeV/$c^2$, open red circles) and from Dalitz pairs ($m$<200 MeV/$c^2$, full black circles) together with their normalized ratio (left panel). Similarly, track distributions for the high-mass ($m$>200 MeV/$c^2$, open red circles) and low-mass ($m$<200 MeV/$c^2$, full black circles) like-sign combinatorial background together with their normalized ratio (right panel).*

differences between low-mass and high-mass pairs, as may have been expected in the absence of correlations.

In lack of proper evidence from data, the polar-angle distributions of the single-electron tracks have been studied in pure (non-overlay) MC simulations for the two extreme ends of the mass spectrum, $\pi^0$-Dalitz pairs and $\phi$-decays. The results are plotted in Fig. 4.20. Sizable differences are now apparent: the Dalitz-tracks are grouped symmetrically around the middle of the acceptance, and the $\phi$-tracks are rather forward-peaked, with a dynamical range in the differences of $\leq$1.7. Folding the Dalitz distribution with the $\theta$-correction function of Fig. 4.18 gives the important (but expected)

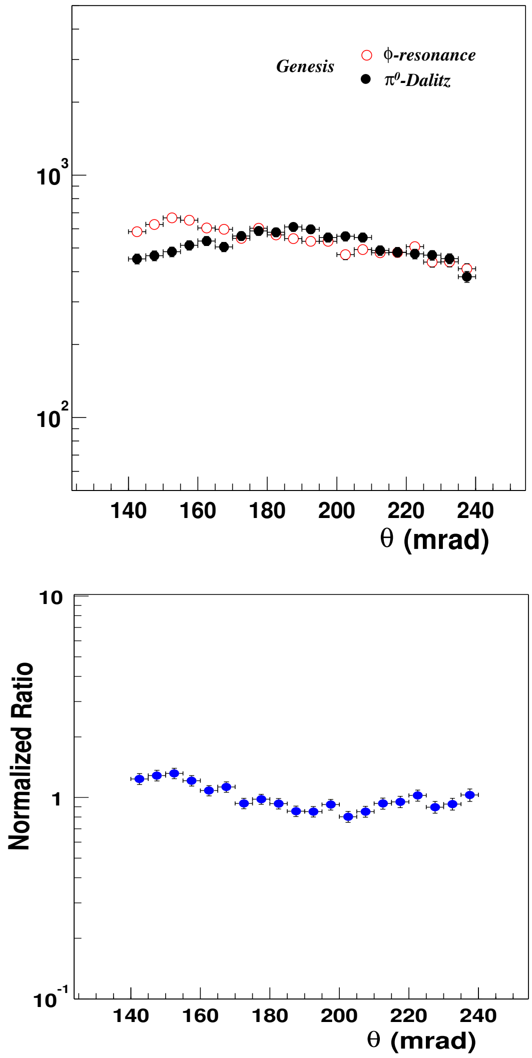


Figure 4.20: *Polar-angle distributions of single-electron tracks for $\pi^0$-Dalitz and $\phi$-decays from pure (non-overlay) MC simulations, together with their normalized ratio.*

result, that the effective pair efficiency from the folding procedure is, to within 1%, identical to using eq.(4.1), i.e. $C$=1 in eq.(4.2): close Dalitz pairs do not require any $\theta$-correction. Conversely, folding-in the $\phi$-track distribution gives $C$=0.96, i.e. the effective pair efficiency for $\phi$-decays is smaller by -4% than that of Dalitz pairs (and presumably less for masses in between). In view of the much larger statistical errors of the 1999 data, corrections on such a low level were judged to be negligible.

### 4.2.5 Conclusion

The efficiency correction of the 1999 mass- and transverse momentum spectra can, within the given errors, be done with one global value:

$$\langle 1/\epsilon \rangle_0^{-1} = 3.6\% \pm 0.07\% (stat.) \tag{4.7}$$

# Chapter 5

# Basic Results

This is a short and somewhat incomplete chapter. It is meant to discuss the main ingredients to the more complete presentation of the final results in chapter 7: the absolute normalization of the data, the creation of the net signal for the particular example of invariant mass spectra, and an overview of the systematical errors of the data. The complete set of the results - mass spectra, transverse momentum spectra and multiplicity dependences - is contained in chapter 7, together with a comparison to the expectations from hadronic decays and various models of direct pair production.

The common conditions for all results are the following: Pb-Au collisions at 40 AGeV in the lab frame, equivalent to ~8.7 AGeV in the center-of-mass frame; trigger selection of the most central 30% of the geometrical cross section; polar angle coverage $0.142 \leq \theta \leq 0.240$ rad; pseudorapidity coverage $2.11 \leq \eta_L \leq 2.64$ in the lab frame, equivalent to $-0.11 \leq \eta_{CM} \leq +0.42$ in the center-of-mass frame; pseudorapidity acceptance $\Delta\eta$=$0.53$; minimum pair opening angle ≥35 mrad; minimum transverse momenta ≥200 MeV/c for both tracks of a pair.

## 5.1 Data Normalisation

The results of this work are mostly communicated as differential spectra in pair mass, in pair transverse momentum or in charged multiplicity. They all undergo an identical procedure of an *absolute* normalization and of an *absolute* efficiency correction. For the example of mass spectra, the final differential quantity plotted is

$$\frac{\langle dN_{ee}/dm_{ee}\rangle_{acc}}{\langle N_{ch}\rangle_{acc}} = \frac{(dN_{ee}/dm_{ee})_{meas}}{N_{ev} \cdot \langle dN_{ch}/d\eta\rangle \cdot \Delta\eta} \cdot \langle 1/\epsilon\rangle_o \tag{5.1}$$

where $\langle dN_{ee}/dm_{ee}\rangle_{acc}$ is the mass-differential probability of $e^+e^-$ pairs/event averaged over the CERES acceptance, $\langle N_{ch}\rangle_{acc}$=$\langle dN_{ch}/d\eta\rangle \cdot \Delta\eta$ is the average number of charged particles within that acceptance, $(dN_{ee}/dm_{ee})_{meas}$ is the raw-data net signal expressed as number of pairs/mass interval, $N_{ev}$ is the total number of analyzed events, and $\langle 1/\epsilon\rangle_o$ is the global mass-independent efficiency correction derived and justified in detail in section 4.2. Numerically, $\langle dN_{ch}/d\eta\rangle$=216 including all corrections (section 3.3.3), $\langle N_{ch}\rangle_{acc}$=$216 \cdot 0.53$=$115$, $N_{ev}$≈8 million events, and $\langle 1/\epsilon\rangle_o^{-1}$=0.036.

## 5.2 Mass Spectra

The normalized and efficiency-corrected mass spectra for the total unlike-sign pairs $N_{+-}$, the like-sign pairs $B_{comb} = 2(N_{++} \cdot N_{--})^{1/2}$ and the net unlike-sign pairs $S_{+-} = N_{+-} - B_{comb}$ are shown in Fig. 5.1. For a direct comparison, the two cases of background treatment discussed at lenght in section 3.5.3 are plotted side-by-side: the background obtained after all rejection steps, and the rescaled background using only partial rejection (up to step 1 in Fig. 3.36, i.e. only $p_t$- and TPC $dE/dx$ cut). Looking at the latter, the improvements in the spectral significance of the net signal in terms of smaller point-to-point fluctuations and smaller error bars (by $\sim \sqrt{2}$) are immediately noticable. Otherwise, the spectral shape of the net pairs reflects the same features as seen in all previous CERES analysis work - a pronounced peak in the region of Dalitz decays for $m$<0.2 GeV/c$^2$, and a structureless continuum for $m$>0.2 GeV/c$^2$, extending up to the region of the $\phi$-meson around 1 GeV/c$^2$.

The integrated data sample entering the mass spectra of Fig. 5.1 after all rejection steps is the following: in the low-mass region $m_{ee}$≤0.2 GeV/c$^2$: total unlike-sign pairs 532±23, like-sign pairs 283±17, net unlike-sign pairs 249±28, signal-to-background ratio 1/1; in the high-mass region 0.2≤$m_{ee}$≤1.15 GeV/c$^2$ (including the $\phi$-bin): total unlike-sign pairs 1236±35, like-sign pairs 1051±32, net unlike-sign pairs 185±48, signal-to-background ratio 1/6. The high-mass sample of 185 pairs is only about 10% of the 2018±237 pairs found in the 1996 analysis, essentially due to the unfortunate running conditions in 1999.

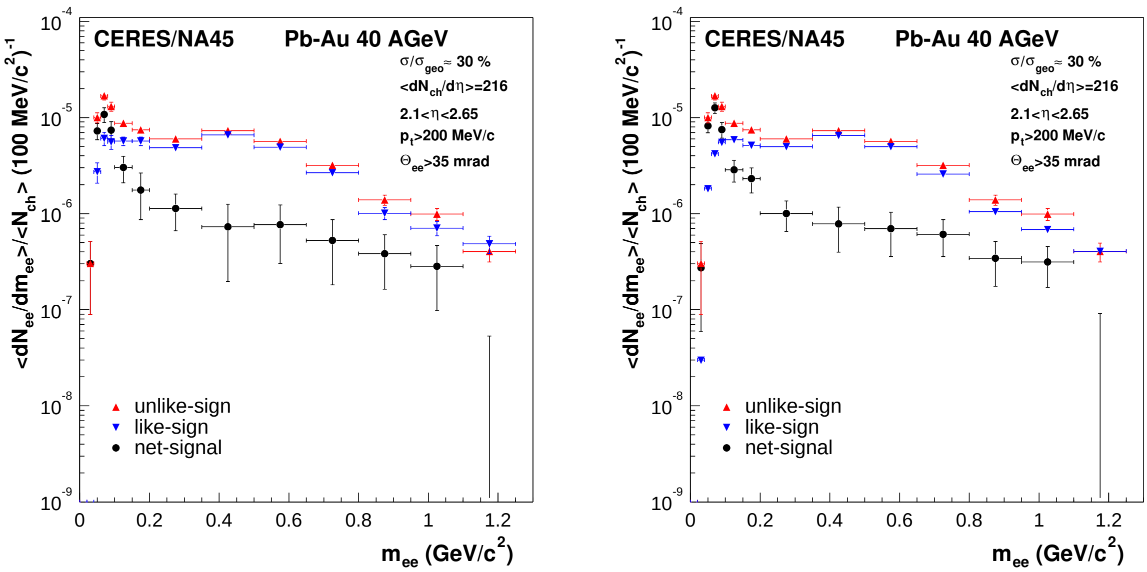


Figure 5.1: *Normalized and efficiency-corrected mass spectra of the total unlike-sign pairs (red triangles), like-sign pairs (blue triangles) and net unlike-sign pairs (black circles). Left panel: like-sign pairs and net signal after all rejection steps. Right panel: rescaled like-sign pairs and net signal using only partial rejection ($p_t$-and TPC $dE/dx$ cut). For a discussion of the experimental errors, see section 5.3 and subscript of Fig. 7.1.*

## 5.3 Systematical Errors

The systematical errors of the data summarized in this section strictly refer to the absolutely normalized differential yield plotted in Fig. 5.1 (and to analogous plots in chapter 7). Systematical errors using different normalizations or referring to comparisons with hadronic decays will be discussed in later sections where needed.

The error estimates can be subdivided into two parts: one, referring to the errors of all entries in eq. (5.1) and therefore common to all masses, the other, connected to the uncertainties of the background subtraction procedure and therefore of importance only for the high-mass region with its unfavorable S/B ratio. The efficiency correction $\langle 1/\epsilon \rangle_o$ in eq. (5.1) gives the largest individual contribution to the overall error. The following uncertainties can be associated with the detailed entries in table 4.1 in section 4.2.3 (all on the *track* level): 3% for the SIDC system (based on data), 2% on the SIDC rejection (based on MC and on pile-up losses from pions on first principles), 3% for the RICH (based on a well-developed MC), 5% for the TPC (based on data and MC), and $\leq$2% for the TPC $dE/dx$ cut (small overall effect). Assuming statistical independence of these values leads to an uncertainty in $\langle 1/\epsilon \rangle_o$ of 14% on the *pair* level. All higher-order corrections of the efficiency discussed in section 4.2.4 are in themselves quadratically small compared to 14%, not to speak about their own errors. The total number of events (8 Mill.) has some uncertainty connected with the first-path filtering; this is estimated to be 5%. The error of the charged multiplicity density, based on the size of the corrections and their understanding, is also estimated to be 5% (supported by the agreement with NA49 data on this level). Assuming again statistical independence for the superposition, an overall error of 16% is obtained for the normalization procedure of eq. (5.1).

In the high-mass region, additional uncertainties arise from the understanding of the rejection cuts and the details of the background subtraction procedure. For the combined 1995/96 analysis, an overall value of 20% has been proposed for this, based on the variation of the final result in a number of independent analysis efforts [23]. For the 1999 analysis with only very few and transparent rejection cuts, the specific error associated with rejection alone is believed to be only about 10%. In the case of the rescaled partial-rejection background with its smaller bin-to-bin errors (by $\sqrt{2}$, right panel of Fig. 5.1), an additional *statistical* error is reintroduced into the normalization by the statistical error of the rescaling factor 10.14±0.3, i.e. 3%, which translates via the S/B ratio of 6 into 18% referred to the net signal and thus to the normalization. The statistical error of the sum over the (improved) data points for the high-mass region is 19%; superposing both numbers gives 26%, consistent with the error of the sum over the post-rejection data points (left panel of Fig. 5.1), which directly mirrors the net high-mass pair sample of 185±48 events. Altogether, assuming statistical independence of all individual contributions, total systematical errors of roughly 20% (full-rejection background) and 26% (rescaled partial-rejection background) are obtained for the high-mass region, including the normalization error connected with eq. (5.1).

# Chapter 6

# Hadronic Decay Sources

## 6.1 The GENESIS Generator

To be able to understand the data and to find *new* physics if possible, the contributions from *known* physics to the inclusive $e^+e^-$ pair spectra need to be discussed. The essential sources of $e^+e^-$ pairs which are definitely expected to contribute are connected to the electromagnetic decays of some of the hadrons produced in the interaction. To describe these decays, the Monte Carlo generator GENESIS has been developed [63, 64], a special event generator written to cope with the requirements of CERES. GENESIS simulates the $e^+e^-$ pair spectra originating from hadronic decays in proton-proton, proton-nucleus and nucleus-nucleus collisions. The sum of all these contributions is called the "hadronic-decay cocktail", and this then is the base which needs to be compared to the data.

The most important of the hadrons contributing to the decays are the neutral mesons: the pseudo-scalars $\pi^0$, $\eta$ and $\eta^{'}$ making Dalitz decays into $e^+e^-\gamma$, and the vector mesons $\rho$, $\omega$ and $\phi$ making direct decays into $e^+e^-$ as well as Dalitz decays, $\omega \rightarrow e^+e^-\pi^0$ and $\phi \rightarrow e^+e^-\eta$. One-by-one, the particles are randomly selected according to their (relative) production cross section and then decayed according to their (relative) decay probability, described by the branching ratio of the respective decay. Since 1994, hadron production has systematically been studied in Pb-induced reactions by several experiments at CERN: NA44, NA49, WA97 and WA98. Therefore, good knowledge exists on the distributions of the primary particles in rapidity and transverse momentum as well as on their total cross sections. All information not directly measured is taken from the statistical model [24, 25], which describes the hadronic final state quite well. The models used to calculate particle production at chemical freeze-out are formulated in the grand canonical ensemble with global baryon, strangeness and charge conservation; all particle ratios are then a function of only two parameters, the freeze-out temperature T and the baryon chemical potential $\mu_B$. The known (vacuum) values for the hadronic masses and the partial decay widths are used without including possible in-medium interaction effects (m$\rightarrow$m$^*$, $\Gamma\rightarrow\Gamma^*$). The inclusive production ratios of the hadrons are implemented relative to the number of $\pi^0$'s; the production ratios of the heavier mesons like $\eta/\pi^0$ or $\phi/\pi^0$ are quite enhanced relative to proton-proton collisions. All yields are normalized via the $\pi^0$ to the charged particle density by

$$\langle dN_{\pi^0}/d\eta\rangle / \langle dN_{ch}/d\eta\rangle_{\eta_{CM=0}} = 0.40 \tag{6.1}$$

which is used as an input parameter. A summary of the particle ratios of relevance is contained in Fig. 6.1 and in table 6.1.

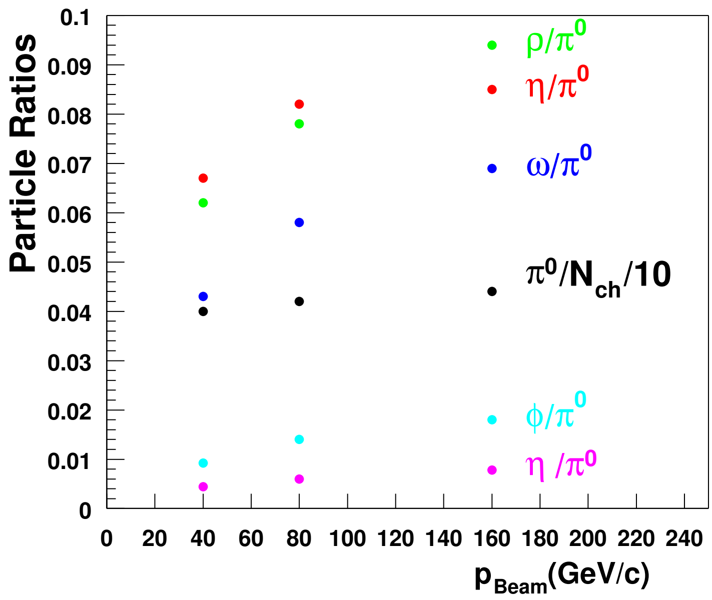


Figure 6.1: *Relative abundance of hadrons calculated from the thermal model for three different beam energies 40, 80 and 160 AGeV [69].*

Each particle is generated with a kinematics based on its specific rapidity and transverse momentum distributions. For the rapidity distribution of all hadrons, the measured rapidity distribution of the pions is assumed to be a sufficiently good approximation. It is taken from NA49, centered at $\eta$=2.3 with $\sigma_\eta$=1.08. The transverse momentum distributions are more complex. Single-inclusive invariant particle spectra are typically exponential in transverse momentum; the reason is phase space of the final multi-particle state. Multi-particle production saturates the available phase space, such that final-state hadrons have exponential spectra with a slope that can be interpreted as a temperature, and an absolute normalization that can be interpreted as fugacity [65]. The $p_t$ distributions of all hadrons except the $\pi^0$ are calculated under the assumption that their spectral shape can be described as

$$\frac{1}{m_t}\frac{dN}{dm_t} \propto exp(-(m_t - m_0)/T), \tag{6.2}$$

where $m_t = \sqrt{m_0^2 + p_t^2}$ is the transverse mass and $m_0$ the particle rest mass. In Pb-induced collisions at the CERN SPS, the slope parameters for the most abundant particle species show a strong dependence on particle mass. The slopes increase linearly with mass, $T_{slope}$=a + b·m, where the parameter $a$ is the slope parameter determined by multiparticle momentum space; $a \sim E/N$ is independent of the system size. The constant $b$ parametrizes additional collective motion; it is proportional to the average collective flow velocity of the radially expanding system [66, 67]. The functional behaviour $T_{slope}$(m) is determined from fits to the experimental data. At 160 AGeV, it is found to be $T_{slope} = 0.175 + 0.115 \cdot m$, mirroring directly the average $T_{f.o.}$ of 175 MeV and the average collective flow velocity $\langle v_T \rangle$ at freeze-out [68]. At 40 AGeV, all heavier mesons are assumed to have the same slope parameters as at 160 AGeV, based on preliminary experimental information. For the special case of $\pi^0$'s, the $m_T$-spectra of $\pi^-$'s are taken from NA49, assuming isospin-independence. However, an additional correction is done, adding the contribution from $\eta \to 3\pi^0$ decays which somewhat softens the $m_T$-spectrum. The final tuning of the GENESIS cocktail for 40 AGeV has much profitted from [64, 69].

| decay | branching ratio | $N_{meson}/N_{\pi^0,tot}$ |
|---|---|---|
| $\pi^0 \to e^+e^-\gamma$ | $1.198 \cdot 10^{-2}$ | 1 |
| $\eta \to e^+e^-\gamma$ | $5.0 \cdot 10^{-3}$ | 0.067 |
| $\rho \to e^+e^-$ | $4.44 \cdot 10^{-5}$ | 0.062 |
| $\omega \to e^+e^-$<br>$\omega \to \pi^0 e^+e^-$ | $7.15 \cdot 10^{-5}$<br>$5.9 \cdot 10^{-4}$ | 0.043 |
| $\phi \to e^+e^-$<br>$\phi \to \eta e^+e^-$ | $3.09 \cdot 10^{-4}$<br>$1.3 \cdot 10^{-4}$ | 0.0092 |
| $\eta' \to e^+e^-\gamma$ | $\sim 5.6 \cdot 10^{-4}$ | 0.0044 |

Table 6.1: *The main particle decays, branching ratios and relative cross sections at 40 AGeV implemented in GENESIS. The branching ratios are taken from the Particle Data Group.*

The branching ratios of the different electromagnetic decays as taken from the review of particle properties are also contained in table 6.1. Dalitz decays are simulated with the Kroll-Wada expression [70]. The resulting rates are multiplied by the electromagnetic transition form factors fitted to the data measured by the LEPTON-G [71] collaboration. The pole approximation $F(M^2) = (1 - b \cdot M^2)^{-1}$ is used for the determination of the form factors of the $\pi^0$ and $\eta$ Dalitz decays [72]. For the $\omega$ and $\eta'$ Dalitz decays, the form factors are determined by fitting a Breit-Wigner function $F(M^2) = m_\rho^4/((M^2 - m_\rho^2)^2 + (m_\rho \cdot \Gamma_\rho)^2)$; the vector-dominance (resonant) behaviour is then described in a proper way. The shape of the $\rho$ is folded with a $\pi^+\pi^-$ phase space factor. For the resonance decays, isotropy is assumed. For the Dalitz decays into $e^+e^-\gamma$, a $(1 + cos^2(\theta))$ distribution is assumed where $\theta$ is measured with respect to the virtual photon direction.

To be able to compare the results from the GENESIS hadronic decay cocktail to the data, the same kinematical cuts need to be applied as for the data, implying in detail (to repeat from chapter 5): acceptance in pseudorapidity 2.11< $\eta_L$ <2.64 in the lab frame with $\Delta\eta$=0.53; minimum pair opening angle $\theta$ >35 mrad; minimum transverse momenta $p_t$ > 200 MeV/c for both tracks of a pair. For a realistic comparison, the GENESIS output finally has to be folded with the experimental resolution functions for the electron momenta and the pair opening angles in the lab frame in order to obtain the appropriate mass resolution in the hadronic decay cocktail (using eq. (3.6)). For the lab momenta, the resolution function was obtained from MC studies as discussed in section 3.4.4 and shown in Fig. 3.21. Numerically, it is described by

$$\sigma_p/p = ((0.04)^2 + (0.012 \cdot p)^2)^{1/2} \tag{6.3}$$

The opening angle resolution is given by

$$\sigma_{\Theta_{ee}} = ((\sqrt{2} \cdot \sigma_\theta)^2 + \overline{sin^2\theta} \cdot (\sqrt{2} \cdot \sigma_\phi)^2)^{1/2} \tag{6.4}$$

with $\sigma_{theta}$=0.6 mrad and $\sigma_\phi$=3 mrad; its influence on the mass resolution is completely negligible.

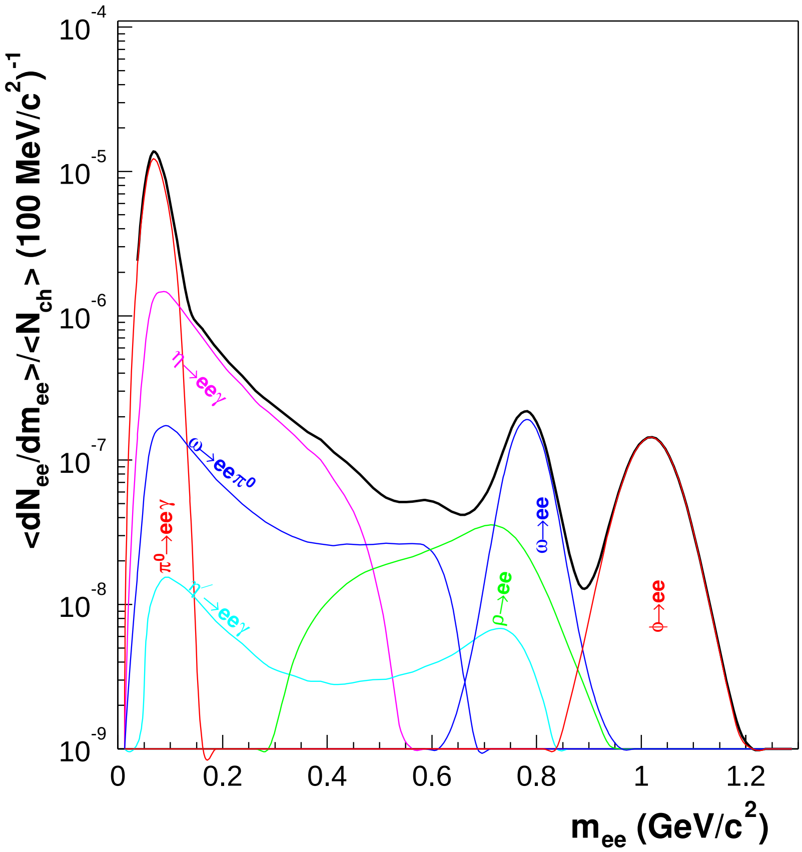


Figure 6.2: *Final dilepton mass spectrum of neutral meson decays ("hadronic decay cocktail") obtained from MC simulations with the event generator GENESIS, including all acceptance and analysis cuts as well as folding with the experimental resolution. The systematical errors as discussed in section 6.2 are 8% for m≤0.2 GeV/c² and about 30% for m>0.2 GeV/c².*

Exactly as for the data, the final results are obtained as normalized differential spectra in pair mass or pair transverse momenta. For the example of mass spectra, the differential quantity plotted is

$$\frac{\langle dN_{ee}/dm_{ee}\rangle_{acc}}{\langle N_{ch}\rangle_{acc}} = \frac{\langle dN_{ee}/dm_{ee}\rangle_{acc}}{\langle dN_{ch}/d\eta\rangle \cdot \Delta\eta} \tag{6.5}$$

where $\langle dN_{ee}/d\eta\rangle_{acc}$ is the predicted mass-differential probability of $e^+e^-$ pairs/event averaged over the CERES acceptance, and $\langle N_{ch}\rangle_{acc} = \langle dN_{ch}/d\eta\rangle \cdot \Delta\eta$ is the average number of charged particles within that acceptance.

The final dilepton mass spectrum for Pb+Au at 40 AGeV, expected from the superposition of the electromagnetic decays of neutral mesons created in the collision, is shown in Fig. 6.2. In the low-mass region <0.2 GeV/c$^2$, the Dalitz decay of the $\pi^0$ completely dominates, while in the high-mass region, the decays of the vector mesons $\omega$ and $\phi$ are most pronounced. The mass resolution, resulting from the folding of the decay cocktail with the experimental momentum- and opening-angle resolution, can be read-off from Fig. 6.2 as $\sigma_m$=4.2% in the region of the $\rho/\omega$. Partial integration of the mass spectrum gives the normalized number of $e^+e^-$ pairs per event and per charged particle for the two mass intervals of interest:

| | |
|---|---|
| low-mass region ≤0.2 GeV/c$^2$ | $7.67 \cdot 10^{-6}$ |
| high-mass region >0.2 GeV/c$^2$ | $1.09 \cdot 10^{-6}$ |

These values will be used for the detailed comparison with the equivalent data integrals in chapter 7.

## 6.2 Systematical Errors

Even more important than in the case of the data, the error estimates will again have to be discussed separately for the low-mass region <0.2 GeV/c$^2$ and the high-mass region >0.2 GeV/c$^2$.

The low-mass region is dominated by the $\pi^0$-Dalitz decay (with the $\eta$-Dalitz contributing $\sim$15%). Errors arise from the relative production cross section of the $\pi^0$ and from the parametrizations of the input rapidity- and transverse-momentum distributions. The normalization of the decay cocktail to the number of charged particles is, of course, extremely powerful to keep the error of the ratio of $N_{\pi^0}/N_{ch}$ small; it is estimated to be at most 5%. The $\eta$-distribution is uncritical, since it is taken directly from $\pi$-data; the error contribution should be <3%. The $p_t$-distribution is somewhat more critical, due to the strong single-electron $p_t$-cut ≥200 MeV/c. However, quite different assumptions on the shape of the $p_t$-spectrum above the cut (e.g. using $h^-$ from CERES rather than $\pi^-$ from NA49) lead to differences in the yield of only very few % [69]. The error is therefore estimated to be again at most 5%. Assuming statistical independence, a total systematical error of 8% is obtained for the Dalitz region.

In the high-mass region, the errors are dominated by those of the relative production cross section of the higher mass mesons and of the detailed properties of their electromagnetic decays. Since most of the particle yields relevant for the cocktail have not directly been measured (or, like the $\phi$, suffer from experimental controversy [73]), the uncertainties associated with the statistical model predictions enter instead; they are assumed to be of order 20%, judging the average fit quality of measured particle ratios. The uncertainties in the branching ratios and in the transition form factors have been discussed in detail in [15]. They contribute $\sim$15% for m<0.45 GeV/$c^2$, $\sim$30% in the mass range of 0.45-0.75 GeV/$c^2$, and 6% for m>0.75 GeV/$c^2$. Taking everything together and assuming again statistical independence, an overall systematical error of very roughly 30% is estimated for the high-mass region of the decay cocktail.

# Chapter 7

# Final Results and Comparison to Theory

## 7.1 Decays after Freezeout - Hadronic Cocktail versus Experiment

### 7.1.1 Inclusive Mass Spectra

The normalized and efficiency-corrected inclusive $e^+e^-$ mass spectrum, shown already as a base result in Fig. 5.1 of chapter 5, can now be compared to the expectations from hadronic decays, normalized in the very same way as the data. This is done in Fig. 7.1. Again, both variants of the background treatment are contained: the full-rejection background (upper part), and the rescaled partial-rejection ("high-statistics"-) background, leading to the improvements in the spectral significance of the individual data points by a factor of $\sqrt{2}$, but keeping the original significance of the spectral integral (see section 5.3). The systematical errors associated with the spectra are given in the subscript of Fig. 7.1. For the data, they are quadratically small compared to the statistical errors of the individual points. For the cocktail, they are small compared to the difference to the data.

For completeness, the total number of net electron pairs entering into the spectra is repeated here from section 5.2: 249±28 with a S/B ratio of 1/1 for m≤0.2 GeV/c$^2$, and 185±48 with a S/B ratio of 1/6 for m>0.2 GeV/c$^2$. Partial integration of the normalized mass spectra of Fig. 7.1 transforms these values into a normalized number of $e^+e^-$ pairs per event and per charged particle for the two mass intervals of interest:

| | | |
|---|---|---|
| low-mass region ≤0.2 GeV/c$^2$ | $7.55 \pm 0.8(stat) \pm 1.2(syst)$ | $*10^{-6}$ |
| high-mass region >0.2 GeV/c$^2$ | $5.61 \pm 1.4(stat) \pm 1.1(syst)$ | $*10^{-6}$ |

Comparing now data and hadronic decays in Fig. 7.1, the following conclusions can be drawn. In the low-mass region ≤0.2 GeV/c$^2$, dominated by the Dalitz decays of the $\pi^0$ and the $\eta$, excellent agreement is found within the errors. However, different from the proton-induced reactions pBe and pAu, but qualitatively similar to all previous

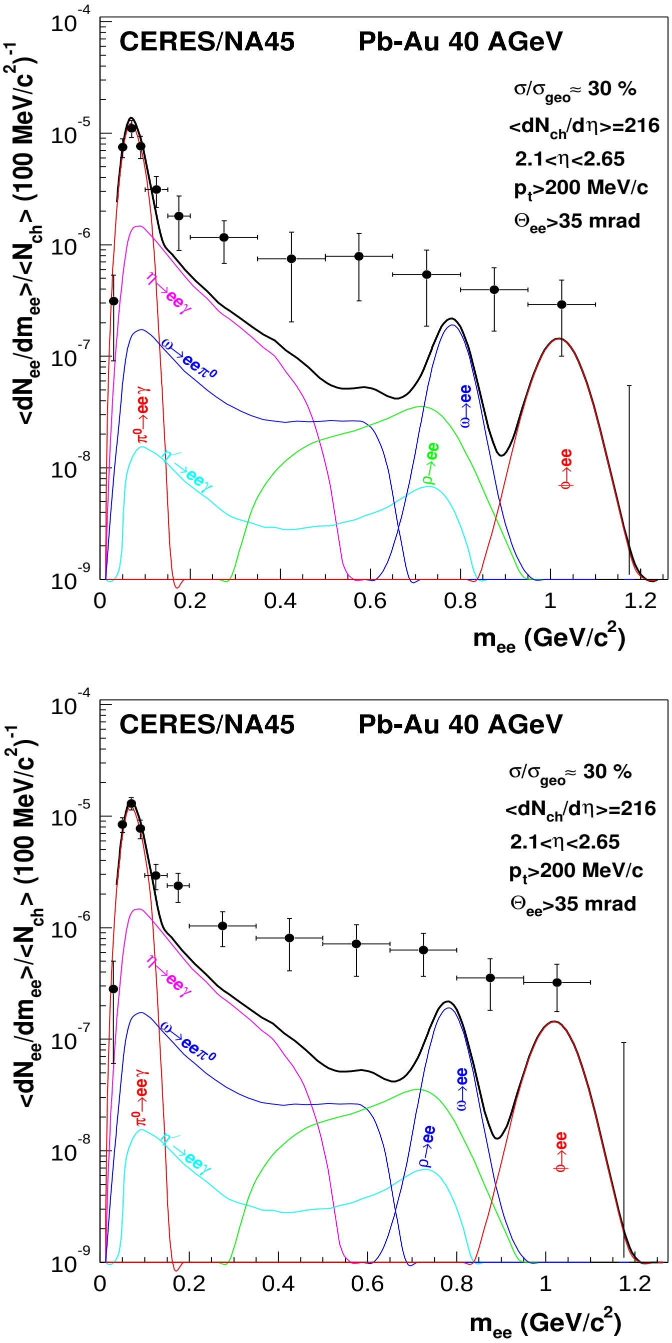


Figure 7.1: *Normalized and efficiency-corrected inclusive $e^+e^-$ mass spectrum compared to the hadronic decay cocktail, using the full-rejection background (upper panel) or the "high-statistics" background (lower panel, compare Fig. 5.1). The errors attached to the data points are purely statistical. The systematical errors of the data are 16% for $m \leq 0.2$ GeV/$c^2$, and 20% (upper panel) resp. 26% (lower panel) for $m > 0.2$ GeV/$c^2$, all quadratically small compared to the individual statistical errors. The systematical errors of the decay cocktail are 8% in the low-mass and 30% in the high-mass region.*

findings of CERES for nucleus-nucleus collisions at higher beam energies, *the hadronic decay cocktail is completely unable to describe the new data at 40 AGeV in the high-mass region*. Instead, a structureless continuum much above the hadronic-decay level is seen, extending all the way up to the $\phi$ without a trace of resonance structure in between, within the limits of the (large) errors. As at 160 AGeV, the data excess shows some threshold behaviour with a set-in around 0.2 GeV/c$^2$ (i.e. already *below* twice the $\pi$ rest mass), becomes maximal in the window 0.25-0.65 GeV/c$^2$ and then decreases again in the region of the vector mesons. In all probability, *the excess is again indicative for the emission of direct radiation, originating promptly from processes during the interaction phase of the collision* (see section 7.2 below).

### 7.1.2 Pair-p$_t$ Spectra

The explore the physics nature of the high-mass enhancement further, the differential spectra in pair transverse momentum $p_t^{ee}$, i.e. the total momentum of the pair perpendicular to the beam axis, has also been investigated. The kinematical acceptance of the CERES spectrometer in a $p_t^{ee}$ vs. $m_{ee}$ plane, including all analysis cuts mentioned before, is shown in the Fig. 7.2. One can clearly see a "hole" in the acceptance, equivalent

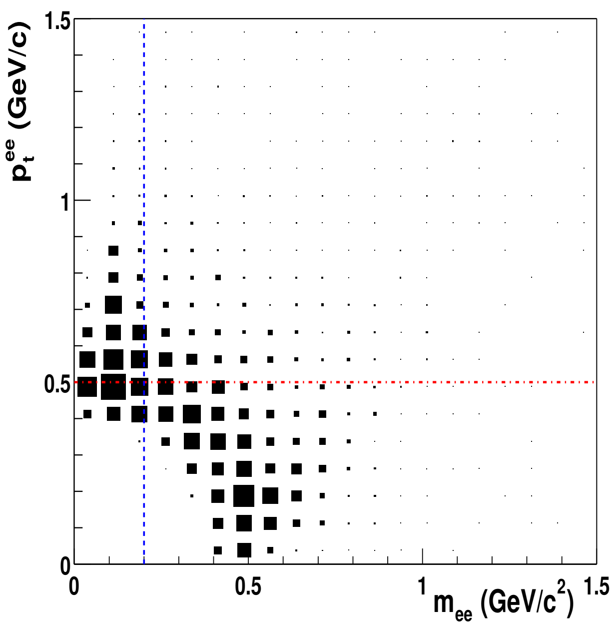


Figure 7.2: *Kinematical acceptance of the data after all analysis cuts, using the total $N_{+-}$ sample as an input. The blue vertical line defines the two mass regions for which the pair-$p_t^{ee}$ distribution is plotted (see Fig. 7.3), while the red horizontal line defines the two regions in pair-$p_t^{ee}$ for which the invariant mass spectra are plotted (see Fig. 7.4).*

effectively to an $m_t$-cut: the single-electron $p_t$-cut of $\geq$0.2 GeV/c applied in the analysis rejects low masses and/or small pair momenta. It strongly influences the shape of the

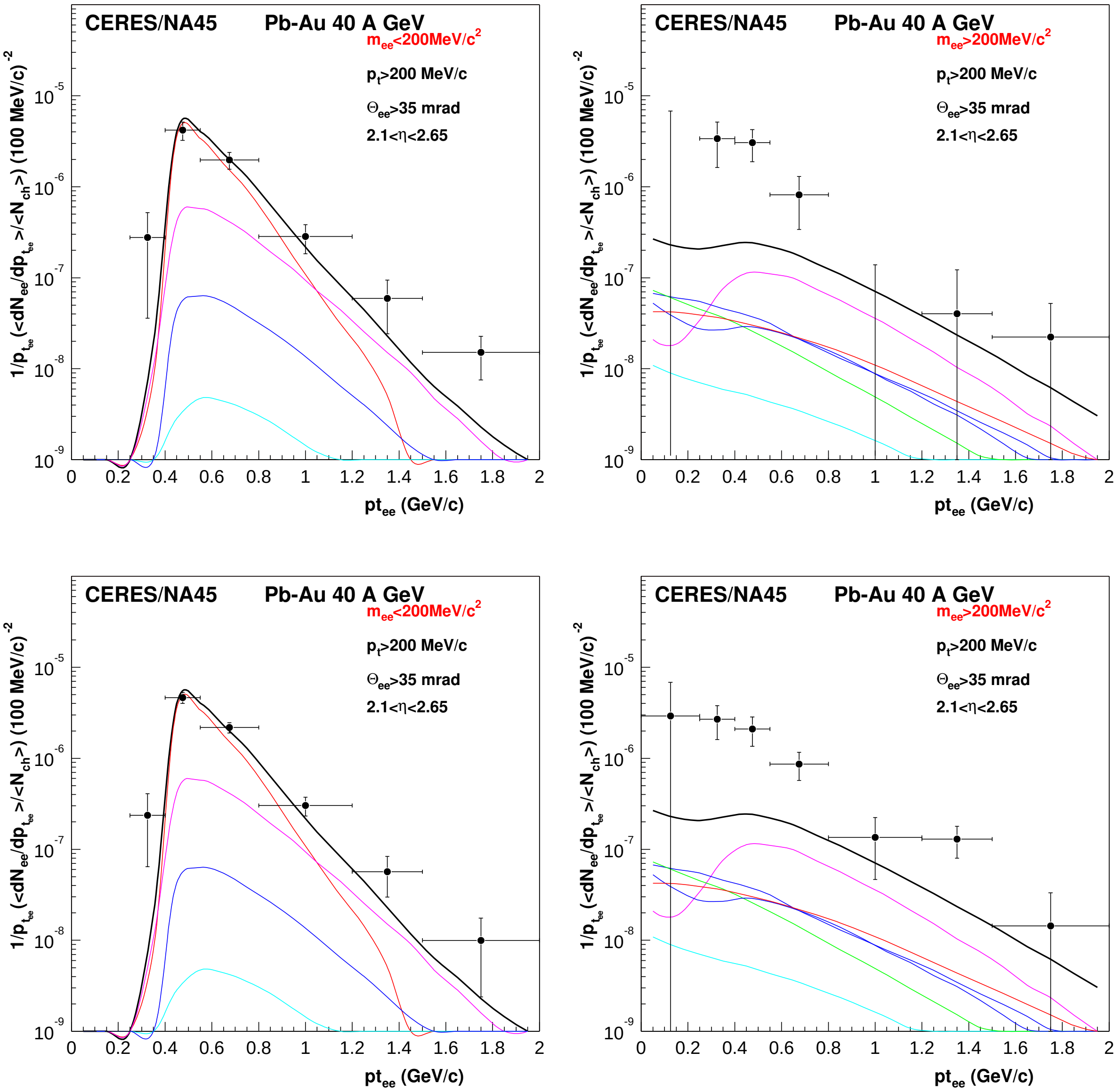


Figure 7.3: *Normalized and efficiency-corrected invariant pair-$p_t^{ee}$ spectra compared to the hadronic decay cocktail, showing separately low-mass pairs $m \leq 0.2$ GeV/$c^2$ (left panel) and high-mass pairs $m > 0.2$ GeV/$c^2$ (right panel) as well as the full-rejection background- (upper panel) and the "high-statistics" background case (lower panel). The errors attached to the data points are purely statistical. The systematical errors of the data are 16% for $m \leq 0.2$ GeV/$c^2$ and 20% (upper panel) resp. 26% (lower panel) for $m > 0.2$ GeV/$c^2$, all quadratically small compared to the individual statistical errors. The systematical errors of the decay cocktail are 8% in the low-mass and 30% in the high-mass region.*

spectra to be discussed in the following.

Fig. 7.3 presents a comparison of the normalized Lorentz-invariant $p_t^{ee}$-spectra with the normalized hadronic decay cocktail, where the normalization follows exactly the same procedure as discussed for the invariant mass spectra (eqs. 5.1 and 6.5, resp.). The spectra are shown separately for low-mass pairs m≤0.2 GeV/c$^2$ and high-mass pairs m>0.2 GeV/c$^2$, and again both variants of the background treatment are contained: the full-rejection- and the rescaled partial-rejection ("high statistics"-) background case, leading to the reduced errors of the net data points. The systematical errors are given

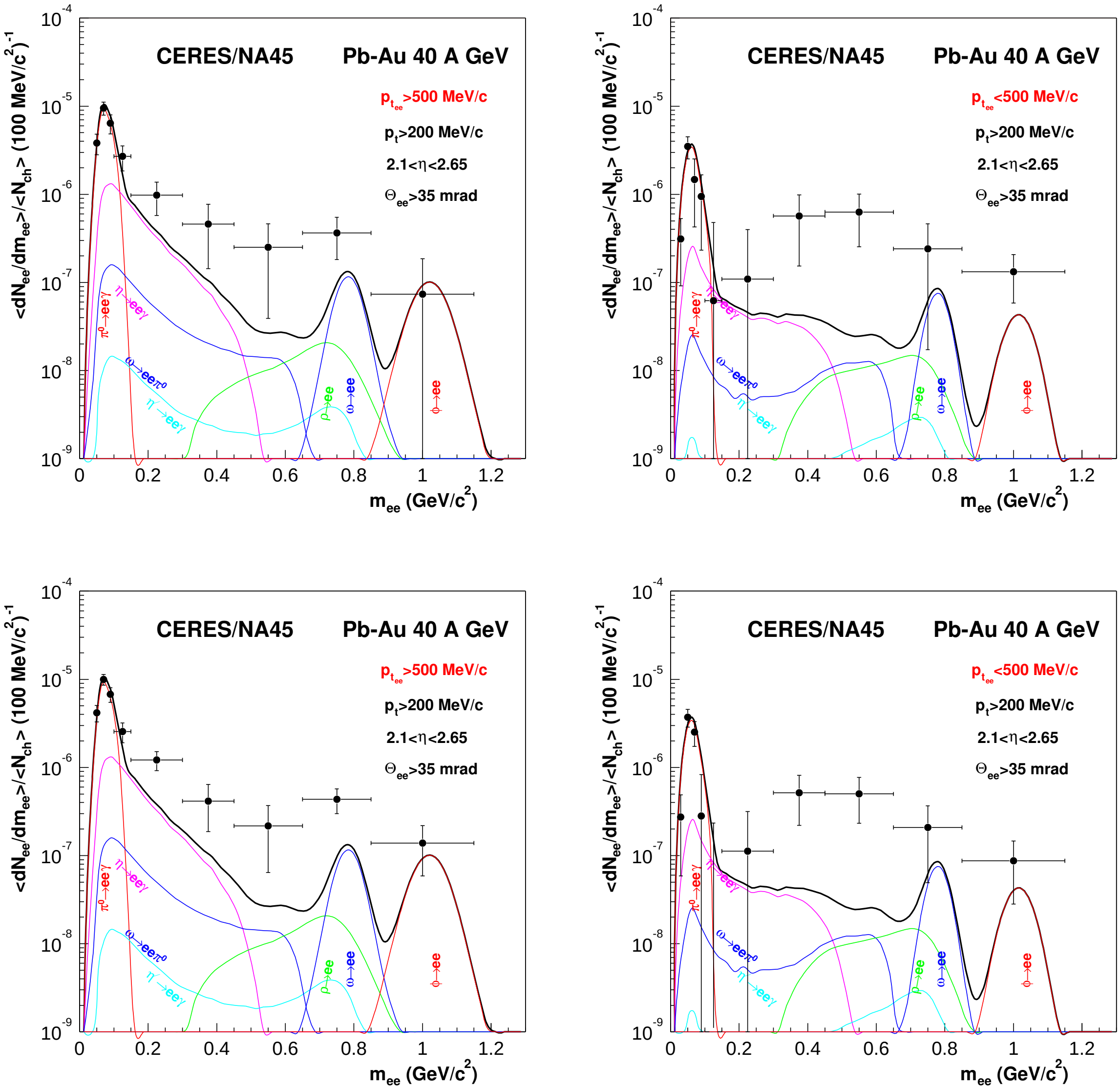


Figure 7.4: *Normalized and efficiency-corrected $e^+e^-$ mass spectra for the two transverse pair momentum bins $p_t^{ee}$>500 MeV (left panel) and $p_t^{ee}$<500 MeV/c (right panel) in comparison to the hadronic decay cocktail. Again, the full-rejection background- (upper panel) and the "high-statistics" background case are distinguished. The errors attached to the data points are purely statistical. For the systematical errors, see detailed description in the subscripts of Figs. 7.1 and 7.3.*

in the subscript of Fig. 7.3; the same conclusions as discussed for Fig. 7.1 hold.

In the mass bin m$\leq$0.2 GeV/c$^2$, complete agreement between the data and the hadronic decay cocktail is found; the experimental points both in magnitude and in slope vs. $p_t$ agree with the expectation from the cocktail. This confirms the expectation that the data in this region are indeed dominated by Dalitz decays. The steep cut-off in the distributions for pair-$p_t^{ee}\leq$0.4 GeV/c reflects, of course, the analysis cut of the single-electron $p_t$>0.2 GeV/c as mentioned above. Conversely, in the mass bin >0.2 GeV/c$^2$, the very strong excess above the cocktail expectation, visible already in Fig. 7.1, now reappears in the $p_t^{ee}$-distribution. It is seen here to be mostly localized at low p$_t^{ee}$<600 MeV/c, in complete agreement with the previous CERES findings at 160 AGeV [18, 19, 20, 21, 22, 23] (see also section 1.2.4).

An alternative way to present these results is to plot the invariant mass spectra for pair-p$_t^{ee}$ below and above 500 MeV/c. This is done in Fig. 7.4 containing again, as before, the two variants of the background treatment. Obviously, the two mass spectra are distinatly different. While complete agreement between data and the decay cocktail is seen for low masses, the excess of the data above the cocktail in the high-mass region is much more pronounced for the lower momentum bin than for the higher momentum one, although some fraction of it resides also there.

In summary, an excess production of low-mass $e^+e^-$ pairs compared to the expectation from hadronic decays is found also at 40 AGeV. In analogy to the findings at 160 AGeV, it is most pronounced in the mass region of 0.2<m<0.6 GeV/c$^2$ and at small pair-p$_t^{ee}$.

### 7.1.3 Multiplicity Dependence

Thermal radiation from parton- or pion- annihilation should show a non-linear, possibly quadratic dependence $\sim(dN_{ch}/d\eta)^2$ on charged particle rapidity density for a fixed interaction volume, reflecting the emission rate to be proportional to the product of particle and anti-particle densities in the reaction [74, 75]. Previous CERES results at 160 AGeV from both 1995([18, 19, 23]) and 1996([20, 21, 22, 23] data indeed show such a non-linear dependence in the mass window where the strongest excess is observed. This has not exactly been new - a $pp$ experiment on lepton-pair production at $\sqrt{s}$=63 GeV at the CERN ISR has, in fact, observed a similar behaviour before [76]. To illustrate non-linearities, it is common to plot the ratio between the normalized data and the normalized hadronic-decay contribution, named "enhancement factor" in the CERES jargon, as a function of charged multiplicity. Since hadron yields are synonymous with multiplicity, lepton pair production dominated by hadron decays would then just follow a horizontal line at 1, while a quadratic multiplicity dependence would appear as a linear rise. The results on the enhancement factor vs. charged multiplicity density for the 40 AGeV data are shown in Fig. 7.5, where the data sample is again separated into low-mass pairs with m$\leq$0.2 GeV/c$^2$ and high-mass pairs with m>0.2 GeV/c$^2$. It is satisfying to see that the low-mass pairs, supposedly dominated by the Dalitz decays of the $\pi^0$ and $\eta$, do follow a horizontal line around 1 within their errors, confirming (in passing) also the correctness of the *absolute* efficiency correction of the data (see also section 7.14 below). The high-mass pairs, on the other hand, show a strong global en-

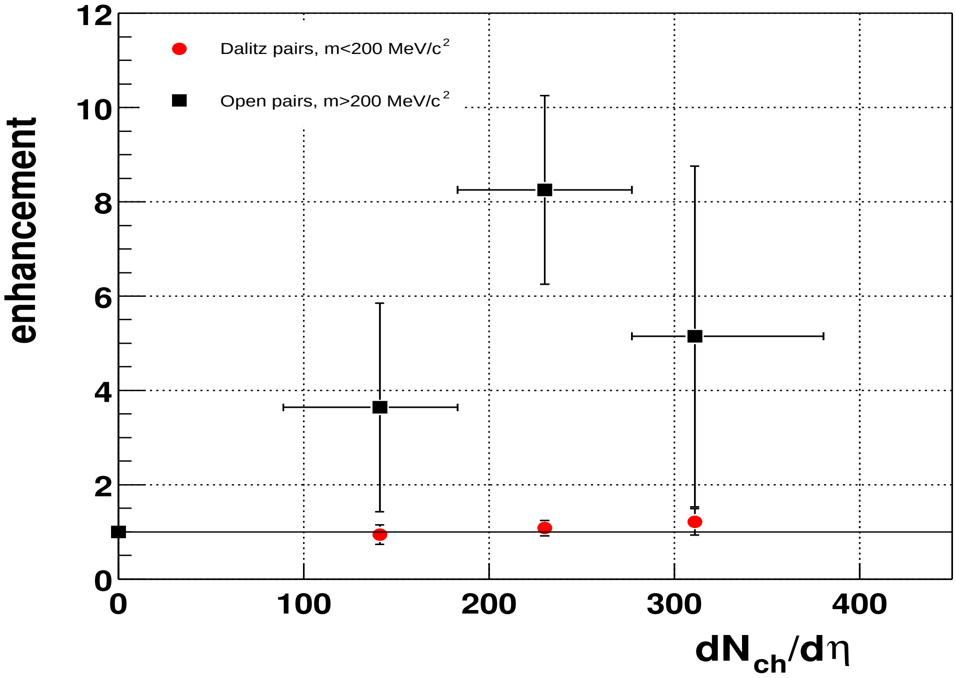


Figure 7.5: *Multiplicity dependence of the "enhancement factor", defined as the ratio between the normalized data and the normalized hadronic-decay contribution, for the two mass bins m≤0.2 GeV/c$^2$ (red circles) and m>0.2 GeV/c$^2$ (black squares). The horizontal solid line at 1 indicates the expectation from final-state hadron decays. The errors attached to the data points are purely statistical. The systematical errors are 16% (data) and 8% (cocktail) for m≤0.2 GeV/c$^2$, and 20% (data) and 30% (cocktail) for m>0.2 GeV/c$^2$.*

hancement $\gg$1, but the error bars are such that a functional dependence, in contrast to the much more favorable 1995/96 situation, cannot be deduced. This is also the reason why a higher-order efficiency correction for the high-mass pairs has not been applied for the 1999 data (see section 4.2.4).

### 7.1.4 High-Mass Enhancement and Comparison to 160 AGeV

The degree of agreement or disagreement between experimental data and the hadronic decay cocktail should finally be illustrated quantitatively, including all errors, by forming again the ratios between the normalized data and the normalized hadronic-decay contributions for the respective partial integrals of the mass spectra (values quoted in section 7.11 and section 6.1), integrating now over multiplicity. The following overall enhancement factors are then obtained for the two mass intervals of interest:

| | |
|---|---|
| low-mass region ≤0.2 GeV/c$^2$ | $0.98 \pm 0.11(stat) \pm 0.16(syst, data) \pm 0.08(syst, cockt)$ |
| high-mass region >0.2 GeV/c$^2$ | $5.1 \pm 1.3(stat) \pm 1.0(syst, data) \pm 1.5(syst, cockt)$ |

While, within the errors, no deviation from the expectation for hadronic decays is seen in the Dalitz region, the enhancement relative to the decay cocktail is found to be about *a factor of 5* in the high-mass region, with a statistical significance of about 4 standard deviations. In comparison, the enhancement factors at 160 AGeV for the same mass region $\geq$0.2 GeV/c$^2$ and a similar trigger selection have been determined as 3.5$\pm$0.4(stat)$\pm$0.9(syst,data) [18, 19, 23] and 2.5$\pm$0.4(stat)$\pm$0.5(syst,data) [20, 21, 22, 23] in the 1995 and 1996 data analysis, resp.. Since the large systematical error of 30% associated with the high-mass part of the hadronic decay cocktail is completely correlated for the 1999 and 1995/96 analysis, it does not need to be considered in the comparison. It is therefore safe to conclude, within the dominantly *statistical error* of the 1999 analysis, *that the enhancement factor at 40 AGeV is found to be significantly larger than at 160 AGeV*. This will be of great importance for the theoretical discussions and conclusions in section 7.2.

Given the enhancement factor, the quality of the combinatorial-background rejection can now be compared between the 1999 and the 1995/96 analysis in a fair way. The S/B ratio 1/6 in 1999 should loose by the difference in multiplicity ratio (216/250) and the difference in enhancement (3.5/5 and 2.5/5, resp.), resulting in extrapolated S/B ratios for 1995/96 of 1/10 and 1/14, resp. Comparing these to the measured ratios of 1/8 and 1/13, resp., implies essentially zero changes in 1999, neither to the better nor to the worse.

## 7.2 Comparison to Different Theoretical Models

This section is meant as a systematic overview over the different theoretical approaches developed to describe the CERES results. Its detail goes somewhat beyond the scope of an (experimental) doctoral thesis, but may nevertheless be useful to put the results into a wider perspective.

### 7.2.1 Fireball Model

The fireball model tries to describe the dynamics and, in particular, the expansion stage of heavy-ion collisions relevant for dilepton production. The interesting physics of chiral symmetry restoration and QGP formation can only be studied for a few fm/c during the early part of the expansion stage when both the density and temperature of the matter are high. As was mentioned before, electromagnetic signals from relativistic heavy-ion collisions directly probe this stage of the collision. However, the observed lepton pair distribution is a complicated integral over the full space-time history of the system. Therefore, to describe the measured data theoretically, the dilepton *rates* originating from all stages of the collision have to be integrated over the full space-time. The complete reaction dynamics with initial conditions is needed: the life time of the system, the equation of state, the speed of thermalization etc. There are basically three approaches to simulate the collisions: Transport simulations such as the Relativistic Quantum Molecular Dynamics (RQMD) [77, 91], Ultra Relativistic Quantum Molecular Dynamics (URQMD) [78, 79, 80], Hadron-String Dynamics (HSD) [81] etc, then Hydrodynamical approaches [82, 83, 84, 85], and finally simplified fireball models which provide parametrizations for temperature and volume [32, 125].

The fireball expansion model simulated by Rapp and Wambach [32], also that by Weise et al. [125], belong to the third group. The fireball undergoes isentropic expansion based on fixed entropy per baryon ($s/\rho_B$ = const) which defines a thermodynamic trajectory in the T-$\mu_B$ plane of the phase diagram including a phase transition from QGP to HG. The transition (QGP-HG) is modelled by a standard mixed phase, constructed from entropy balance. It is also consistent with a hadro-chemical analysis, i.e. with conservation of pion number and of the other observed particle multiplicities between chemical ($T_{ch}, \mu_{B_ch}$) and thermal freeze-out ($T_{th}, \mu_{B_th}$) [86]. The model describes the temperature- and baryon density evolution as well as the volume expansion.

To introduce the time scale, the volume expansion is approximated by cylindrical geometry with two fire-cylinders expanding in the $\pm$z direction, filling the experimentally observed rapidity region in the final state [28]:

$$V(t) = 2(z_0 + v_z t + \frac{1}{2}a_z t^2)\pi(r_0 + \frac{1}{2}a_\perp t^2)^2 \tag{7.1}$$

Assuming isentropic expansion, the temperature profile T(t) is determined as follows:

$$T(t) = (T^i - T^\infty)e^{-t/\tau} + T^\infty \tag{7.2}$$

The baryon density is determined by the number of participants, supplemented with an isotropic volume expansion which is described by an average baryon chemical potential $\mu_B$= 400 MeV:

$$\rho_B(t) = \frac{N_B}{V(t)} \tag{7.3}$$

All parameters are determined such as to properly generate the end point of the fireball evolution, i.e. the freeze-out stage, reproducing all hadronic observables like particle ratios, HBT radii, flow velocity, $m_t$-spectra and $dN/dy$ distributions.

Once the time evolution of the fireball is given in terms of the temperature T(t), baryon density $\rho_B(t)$ and volume V(t), the differential dilepton *spectrum* is calculated via different models for the dilepton *rate*, integrating over space-time and over momentum:

$$\frac{dN_{ee}}{dM} = \int_{\tau_i}^{\tau_{f_0}} d\tau V_{FB}(\tau) \int d^3q \frac{M}{q_0}\frac{dR_{ee}}{d^4q}(M, q; \mu_B T) \cdot A_{cc} \tag{7.4}$$

All cuts are applied as used in the data analysis: each electron/positron track is required to have a transverse momentum $p_t$>0.2 GeV/c, to fall into the rapidity interval 2.11<$\eta$<2.64 (lab frame), and to have a pair opening angle $\Theta_{ee}$>35 mrad (the function $Acc$ accounts for all these cuts). In addition, contributions from long-lived hadron decays after freeze-out, i.e. from the so called hadronic decay cocktail discussed extensively in chapter 6, have to be included. Only then, a fair comparison to the data can be done.

### 7.2.2 Free $\pi^+\pi^-$ Annihilation in a Hadronic Fireball

The observation of an enhancement of low-mass dilepton production by CERES/NA45 at 160 AGeV as well as at lower beam energy of 40 AGeV (presented in this thesis) has stimulated a large amount of theoretical activity. The superposition of the known hadronic decay sources can successfully account for the measured spectrum in proton-induced reactions, but it fails to reproduce the measured low-mass dilepton spectra in nucleus-nucleus collisions. This indicates the emission of further radiation, which is generally interpreted as direct radiation originating from processes during the interaction phase of the collision. Since vector mesons directly decay into dileptons, a change of their masses and widths can be seen directly in the dilepton invariant mass spectrum. Several theoretical approaches have studied medium effects in dilepton production rates from hot/dense matter:

1) the 'dropping $\rho$ mass' scenario (within a mean-field type treatment) [29, 30, 31, 87, 88]

2) the chiral reduction formalism (based on chiral Ward identities) [89, 90]

3) a chiral Lagrangian framework [91] or many-body-type calculations of in-medium vector meson spectral functions [32, 92, 93, 94].

Dileptons are produced by the annihilation of thermally excited particles: $q\bar{q}$ in the QGP phase and $\pi^+\pi^-$ in the hadronic phase. However, the dominant particles at SPS energies are pions, therefore the main source of dilepton radiation is two-body $\pi^+\pi^-$ annihilation . The dilepton production rate in a hadronic medium of given temperature T and baryon chemical potential $\mu_b$ can be calculated as

$$\frac{dR_{l^+l^-}}{dq^4} = L_{\mu\nu}(q)W^{\mu\nu}(q) \tag{7.5}$$

through contraction of the $L_{\mu\nu}$-leptonic and the $W^{\mu\nu}$-hadronic tensor. To lowest order in the electromagnetic coupling constant $\alpha = 1/137$, the leptonic tensor is determined as

$$L_{\mu\nu} = -\frac{\alpha^2}{6\pi^3 M^2}(g_{\mu\nu} - \frac{q_\mu q_\nu}{M^2}) \tag{7.6}$$

while the hadronic tensor, which contains all information on the hadronic medium of temperature T and baryon chemical potential $\mu_B$, is obtained from the thermally averaged electromagnetic iso-vector current-current correlation function (by using the grand canonical ensemble):

$$W^{\mu\nu}(q) = \int d^4x e^{-iqx} \langle\langle j_\mu^{em} j_\nu^{em} \rangle\rangle = \tag{7.7}$$

$$W^{\mu\nu}(q) = \sum_i \frac{e^{E_i/T}}{Z} \sum_f \langle i|j^\mu(0)|f\rangle\langle f|j^\nu(0)|i\rangle \cdot (2\pi)^4\delta^4(q + p_f - p_i) \tag{7.8}$$

To determine the contraction between the leptonic and the hadronic tensor, the correlation function has been connected to the one-particle irreducible photon self energy

$$-2Im\Pi^{\mu\nu}_{em} = (e^{q_0/t} - 1)W^{\mu\nu} \tag{7.9}$$

This means, to first order in the electromagnetic coupling constant $\alpha$, that the current-current correlation function is the same as the photon self energy [95]. Requiring gauge invariance

$$q_\mu \Pi^{\mu\nu}_{em} = 0 \tag{7.10}$$

and using the previous equation, the dilepton emission rate from the hot region populated by particles in thermal equilibrium is proportional to the imaginary part of the spin-averaged, time-like photon self energy [96].

This means that thermally excited particles annihilate to virtual photons which decay into lepton-antilepton pairs. The final result for the thermal rate is then

$$\frac{dR_{l^+l^-}}{dq^4} = -\frac{\alpha^2}{\pi^3 M^2} f^B(q_0;T) Im\Pi_{em}(q_0,\vec{q}), \tag{7.11}$$

($f^B = \frac{1}{e^{q_0/T}-1}$-Bose occupation.)

By using an effective Lagrangian compatible with gauge invariance and consistent with global chiral symmetry, the low-energy region of the correlator can very well be described. This model is called Vector-Meson-Dominance. In the spirit of VMD, the photons, decaying into $e^+e^-$ pairs, couple to hadronic $J^P = 1^-$ states: the $\rho$, $\omega$, $\phi$ and multi-pion states carrying the same quantum numbers. Applying this formalism and starting from an effective Lagrangian of the coupled system of pseudoscalar mesons (Goldstone bosons), vector mesons and photons, the hadronic part of the electromagnetic current can be identified with the field of neutral isovector mesons $V^\mu$ with the universal VMD coupling

$$j^\mu = \frac{(m_V^{bare})^2}{g} V_3^\mu, \tag{7.12}$$

and as a consequence the imaginary part of the irreducible photon self-energy $Im\Pi_{em}$ is expressed through the imaginary parts of the vector meson propagators (spectral functions)

$$Im\Pi_{em}(q) = \sum_V \frac{m_V^4}{g_V^2} \cdot ImD_V(q) \tag{7.13}$$

The modifications of the vector meson properties (mass, width) are described by the self energy $\Sigma_V$ which contains all interactions with the surrounding matter, i.e. the dilepton spectra will also be strongly modified and contain all information about medium modifications of the vector mesons:

$$D_V(M,q) = [M^2 - m_V^{(0)^2} - \Sigma_V]^{-1} \tag{7.14}$$

The most prominent is the $\rho$ meson, due to its very large width compared to the time scales involved in heavy-ion reactions. The main decay channel is two-body $\pi^+\pi^-$ decay. In the reverse time direction, $\pi^+\pi^-$ annihilation proceeds via an intermediate $\rho$-meson:

$$\pi^+\pi^- \to \rho^* \to \gamma^* \to e^+e^- \tag{7.15}$$

In vacuum, at zero temperature T=0 and at zero baryon density $\rho_B$=0, annihilation is mediated by a vacuum $\rho = \rho^0$

$$\pi^+\pi^- \to \rho^0 \to \gamma^* \to e^+e^- \tag{7.16}$$

with the well known width of $\Gamma_\rho^0 \sim Im\Sigma_{\rho\pi\pi}^0$ ~150 MeV, while the physical mass of the vacuum-$\rho^0$ M=770 MeV/c$^2$ is determined by solving for the real part of the $\rho$ dispersion relation. The $\rho$ self-energy can be determined by using a $\pi\rho$ interaction Lagrangian [97], and to order of $g^2$ ($\rho\pi\pi$ coupling) it is represented by the two loop diagrams:

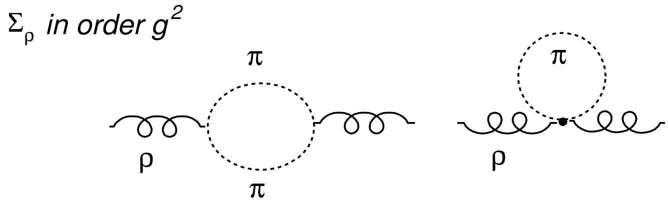


Figure 7.6: *One-loop contributions to the vacuum $\rho$-meson self energy: $\rho\pi\pi$ coupling (left panel) and a tadpole diagram $\rho\rho\pi\pi$ (right panel).*

One way to calculate these diagrams is to use the imaginary time (Matsubara) formalism [98], and divergences which appear in the vacuum terms are regularized by using the Pauli-Villars scheme [99].

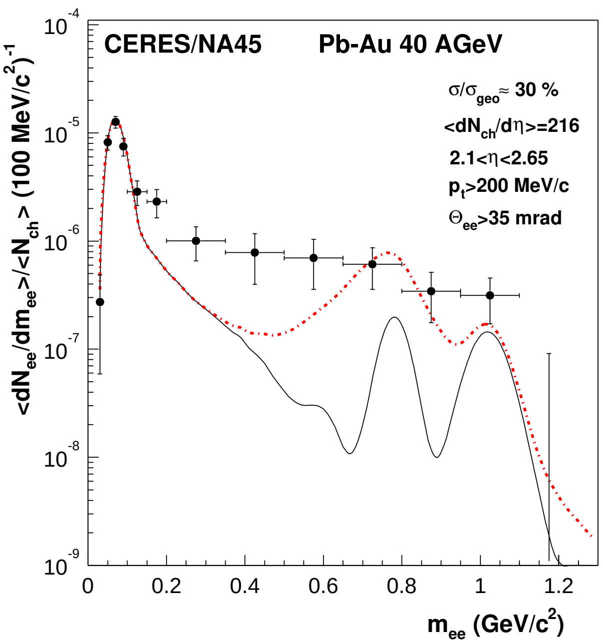


Figure 7.7: *Comparison of the 40 AGeV data to a model calculation [11, 86], based on $\pi^+\pi^-$ annihilation with an unmodified $\rho$ (red dashed-dotted line). The calculation includes the hadronic decay contribution which is also shown separately (thin solid line). It is taken from CERES (Fig. 6.2 in chapter 6), but excludes the contribution from the $\rho$ to avoid double counting. For a discussion of the experimental errors, see subsection of Fig. 7.9.*

Finally, to be able to compare the vacuum model to experimental data, the vacuum spectra have to be computed for the thermal fireball expansion with the realistic dynamics of a heavy-ion collision. The differential dilepton rate

$$\frac{dR_{\pi\pi\to ee}}{dq^4}(q_0,q) = -\frac{\alpha^2}{\pi^3 g^2_{\rho\pi\pi}} \frac{f^\rho(q_0;T)}{M^2} Im\Sigma^0_{\rho\pi\pi}(M)|F^0_\pi(M)|^2 \tag{7.17}$$

is integrated over the space-time history of the collision applying all experimental cuts (see previous subsection).

The comparison of the vacuum model with the data from Pb-Au collisions at 40 AGeV is shown in Fig. 7.7. Clearly, free $\pi^+\pi^-$ annihilation can not describe the data. The experimentally observed enhancement at invariant masses 0.2<$m_{ee}$<0.6 GeV/$c^2$ is much larger then the low-mass tail from free $\pi^+\pi^-$ annihilation. This also implies that the total yield is too large compared to the fact that the free pion electromagnetic form factor peaks at the $\rho$ resonance

$$|F^0_\pi(M)| = (m^{(0)}_\rho)^4 \cdot |D^0_\rho(M)|^2 \sim \left(M^2 - (m^{(0)}_\rho)^2 + \Sigma_{\rho\pi\pi}(M)\right)^{-1}, \tag{7.18}$$

There is possibly too much yield around the free $\rho$ mass, and definitely too little below.

The final conclusion is then that the assumption of free $\pi^+\pi^-$ annihilation is oversimplified. For a better description of the data, the inclusion of modifications of the vector meson properties in the hot and dense environment seems to be essential.

### 7.2.3 Medium Effects

Medium effects in dilepton production rates are studied by focusing on the role of the $\rho$-meson spectral function (in-medium $\rho$ propagator), considering the $\rho$ to be the most important of the vector mesons. As mentioned before, the isovector $\rho$(770) meson strongly couples to the $\pi\pi$ channel (branching ratio $\sim$100%), is short-lived and is a major constituent of the pion-dominated hot hadron gas. The binary reaction $\pi\pi \rightleftharpoons \rho$ proceeds both ways in chemical equilibrium. Most $\rho$ mesons decay inside the fireball into pions which interact many times, but only a tiny fraction of about $10^{-4}$ $\rho$'s decays electromagnetically into lepton pairs, $\rho^* \to \gamma^* \to e^+e^-$. The mass $m^*$ of the $\rho^*$ is transported into the 4-momenta $p_+$,$p_-$ of the electron pair without distortion; it can be measured in the CERES spectrometer as the invariant mass $m^2=(p_+ + p_-)^2$ of the pair. However, different from the vacuum case with a $\rho^0$ mass of 770 MeV/$c^2$, the embedment of the $\rho$ in the dense and hot medium acts as if it would have a significantly lower mass, or a significantly broader width. The extraction of the $\rho$'s effective mass, lifetime and rate of decay into lepton pairs is very model dependent.

In the following, the results from the 40 AGeV data will be compared to the different theoretical approaches developed to explain the low-mass dileptons by the inclusion of medium effects. Fig. 7.8 shows a comparison of the 40 AGeV invariant-mass spectra to the two main theoretical approaches which include a medium modification of the $\rho$ spectral function by a dynamical lowering of the effective $\rho$-meson mass to $\sim$ $m_\rho/2$ in a very different way:

- Brown-Rho scaling: the dynamical lowering is explained by a baryon-density dependent reduction of the $\rho$ mass .

- Rapp and Wambach : modification of the dispersion relation of mesons, baryons and their resonances in the hot and dense medium due to hadronic interactions; the effective dynamical lowering of the mass is due to a massive spreading of the width of the $\rho$.

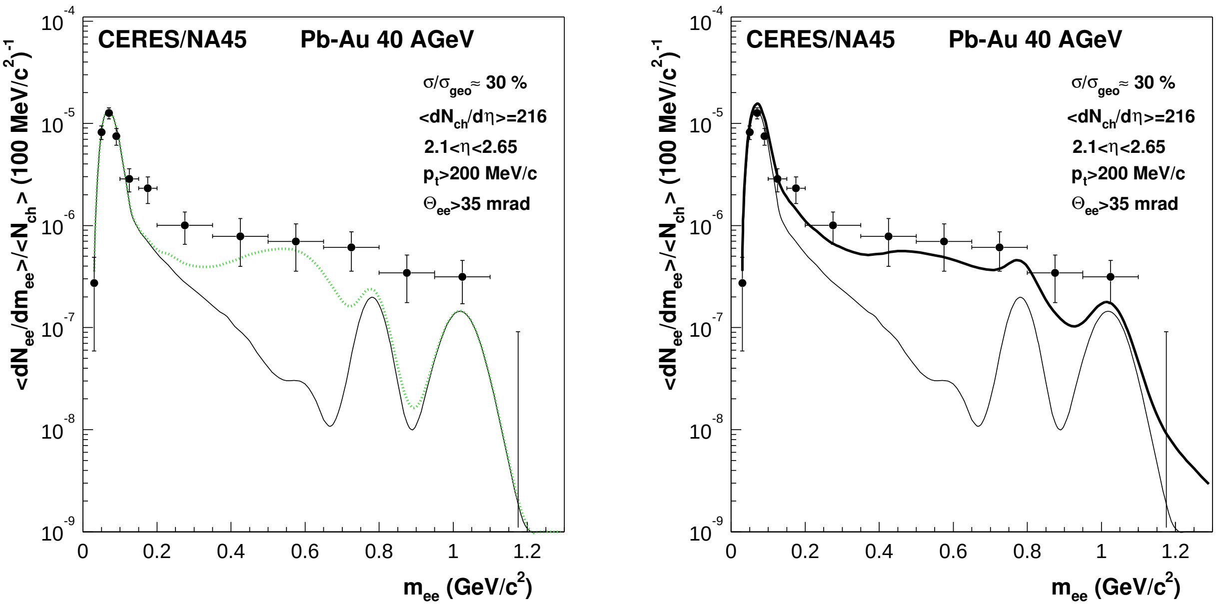


Figure 7.8: *Comparison of the 40 AGeV data to model calculations based on $\pi^+\pi^-$ annihilation with a dropping $\rho$ mass [100, 86] (left panel, green dotted line), and on $\pi^+\pi^-$ annihilation with an in-medium spreaded $\rho$ [86] (right panel, black thick solid line). Both calculations contain the sum of the hadronic decay sources. This sum is taken from the CERES cocktail (Fig. 6.2 in chapter 6) and shown also separately in both panels (thin solid line). It excludes the contribution of the $\rho$ to avoid double counting. For a discussion of the experimental errors, see subscript of Fig. 7.9.*

**Brown/Rho scaling**

The approach based on BR scaling [29, 87, 100, 103, 104, 110] is dictated by chiral and scale symmetry before reaching the chiral restoration transition. It starts from the known structure of the effective QCD Lagrangian at low energy and zero density which is governed by symmetries and other constraints of QCD like spontaneously broken chiral symmetry in the vacuum due to nonvanishing quark and gluon condensates, appearance of eight nearly (explicitely broken chiral symmetry) massless Goldstone bosons, appearance of anomalies like the anomaly of the chiral current and the trace anomaly ($\partial^\mu T_{\mu\nu} \neq 0$)).

In the B/R theory, embedding a hadron into hot and dense matter is equivalent to changing the vacuum, thereby modifying quark and gluon condensates in QCD variables. The assumption that the symmetry, i.e. the Lagrangian remains the same as T and density increase, implies that at each T and density masses and coupling constants are modified according to the symmetry of QCD.

Hadron masses, such as that of the $\rho$-meson, violate scale invariance. Scale invariance is a symmetry of the classical QCD Lagrangian. In QCD, scale invariance is broken on the quantum level by the so called trace anomaly, which is proportional to the gluon condensate. Therefore, with the disappearance of the gluon condensate, scale invariance would be restored implying that the hadron masses have to vanish [101]. The BR approach starts from the assumption that the gluon condensate can be separated into a hard and a soft part [102], where the soft part scales with the quark condensate and light hadron masses are proportional to $\langle q\overline{q}\rangle$. Therefore, a universal scaling is assumed, linking masses and the evolution of the chiral order parameters. Scaling hadron masses are then introduced into the chiral Lagrangian. All hadron masses (except of the Goldstone bosons) follow the universal scaling law, decreasing in dense matter together with the order parameters of chiral restoration ($f_\pi$ or quark condensate) as:

$$\frac{m_{\sigma^*}}{m_\sigma} \approx \frac{m_{\rho^*}}{m_\rho} \approx \frac{m_{N^*}}{m_N} \approx \frac{f_\pi^*}{f_\pi} \approx \frac{\langle\overline{q}q\rangle^*}{\langle\overline{q}q\rangle} \approx \frac{\chi^*}{\chi} \equiv \Phi \tag{7.19}$$

where the symbol $'*'$ refers to in-medium quantities and quantities without $'*'$ correspond to the free-space values.

With Brown-Rho scaling, the vector meson masses go to zero in sufficiently hot and/or dense matter together with the chiral order parameters, which is a direct consequence of chiral symmetry restoration [103]. Conversely, decreasing T and density through the phase transition in building up the scalar field energy, the hadrons are getting back there masses [104]. Lattice QCD simulations show that the quark condensate has a weak dependence on temperature up to about $0.9T_c$, while around the critical temperature the quark condensate decreases very rapidly indicating chiral symmetry restoration and thereby supporting Brown-Rho scaling [105, 106]. The Brown-Rho scaling hypothesis can also be linked to the result of [33] or to a QCD sum rule analysis [107, 108, 109], where the density- and temperature dependence of $m_\rho^*$ then follows as

$$\frac{m_\rho^*}{m_\rho} = \frac{\langle\overline{q}q\rangle^*}{\langle\overline{q}q\rangle} = (1 - C\rho_B/\rho_0)(1 - (T/T_c^\chi)^2)^\alpha \tag{7.20}$$

For the dilepton spectra, the most relevant feature is the decrease of the mass of the $\rho$ at finite temperature and density [110]. This leads to a strong excess of $e^+e^-$ pairs below the free $\rho$ mass through the $\pi\pi$ channel. To be able to directly compare the two different approaches Brown/Rho and Rapp/Wambach, both have to be computed in the same thermal fireball expansion with the same initial and freeze-out conditions.

A comparison then of the BR approach of the 'dropping mass' to the data (left panel of Fig. 7.8) shows that this model indeed leads to a strongly enhanced dilepton yield below the free $\rho$ mass, implying that the lepton pairs are predominantly emitted in a temperature/density region which shifts the $\rho$ mass to $\leq$2/3 of its vacuum value. A more quantitative conclusion, also distinguishing between broadening (right panel) and movement towards chiral restoration is hardly possible, considering the large error bars of the data.

**In-medium effects due to hadronic interactions (Rapp/Wambach)**

As emphasized in subsection 7.22, the dilepton production rate is related to the electromagnetic vector current-current correlation function, and in the low-mass region this current-current correlator in the vector channel is largely saturated by the vector mesons $\rho, \phi, \omega$, most important the $\rho$. The Rapp/Wambach approach [11, 28, 86, 92, 112, 114] to cope with medium effects is based on an effective hadronic theory described by a chiral Lagrangian combined with Vector Meson Dominance, including now the coupling of the $\rho$ to hadronic many-body excitations. Within VMD, the $\rho$ meson couples dominantly to two-pion states, but the vacuum two-pion loop $\Sigma^0_{\rho\pi\pi}$ (see 7.22) has to be replaced by dressed in-medium ones $\Sigma_{\rho\pi\pi}$. Also, the $\rho$-meson can interact resonantly with nucleons at finite baryon density, as described by self-energy contributions $\Sigma_{\rho B}$, and with thermal mesons at finite temperature, as described by an additional self-energy contribution $\Sigma_{\rho M}$.

Based on nuclear and finite-temperature many-body techniques, the $\rho$-meson self-energy $\Sigma_{tot} = \Sigma_{\rho\pi\pi} + \Sigma_{\rho B} + \Sigma_{\rho M}$ is evaluated, containing the medium modifications of the $\rho$-meson properties (like mass, width). The medium modifications of these properties are again directly reflected in the dilepton spectrum.

The form of the in-medium $\rho$ propagator in hot baryon rich matter is

$$D_\rho(M, q; T) = [M^2 - m_\rho^{(0)^2} - \Sigma_{\rho\pi\pi} - \Sigma_{\rho B} - \Sigma_{\rho M}]^{-1} \tag{7.21}$$

and the $\rho$ properties mass and width are calculated from the real and imaginary part of that propagator.

Temperature effects on the $\rho$ spectral function are determined from the imaginary and real part of $\Sigma_{\rho\pi\pi} + \Sigma_{\rho M}$. The temperature effect on $\Sigma_{\rho\pi\pi}$ leads to a medium modification of the $\rho$ meson generated by dressing the intermediate two-pion states in hot matter [113, 114]. $\Sigma_{\rho M}$ describes the direct interaction with thermal mesons saturated with s-channel resonances : $\rho\pi \to a_1$(1260), $\rho K/\rho\overline{K} \to K_1(1270)/\overline{K_1}(1270)$ [114, 115]. The results of these temperature effects are a negligible broadening of the $\rho$ spectral function, and an only small mass shift compared to the mass pole in vacuum.

Baryonic-density effects arise from pions interacting with the surrounding nucleons, creating an additional increase of $|Im\Sigma_{\rho\pi\pi}|$. This leads to a mixture of pions with nucleon-hole (Nh) and delta-hole ($\Delta h$) excitations. The pion cloud is modified due to a strong coupling to $\pi N N^{-1}$ and $\pi\Delta N^{-1}$, the so called '$\pi$-sobars'. The results are additional medium modifications of the $\rho$ meson, generated by additional dressing of the intermediate two-pion states in baryonic matter; this causes further broadening of the $\rho$ spectral function. In baryon-rich matter, the $\rho$ also interacts resonantly ( $\Sigma_{\rho B}$), creating the so called '$\rho$-sobar' [93] excitations of S-wave (N(1520)N$^{-1}$, $\Delta$(1700)N$^{-1}$, ..) or P-wave type ($\Delta N^{-1}$, N(1720)N$^{-1}$,..). Adding the contributions $\Sigma_{\rho B}$ results in a still stronger broadening of the spectral function, without producing a further mass shift [116].

The numerical results, setting T to zero and keeping finite baryon density, or setting baryon density to zero and keeping finite T, clearly confirm that the *broadening* of the $\rho$ spectral function depends predominantly on *baryon density*, while the (anyway small) total mass shift is due to temperature effects [113]. The *baryonic effects prevail over mesonic ones*, due to the stronger nature of the meson-nucleon interaction.

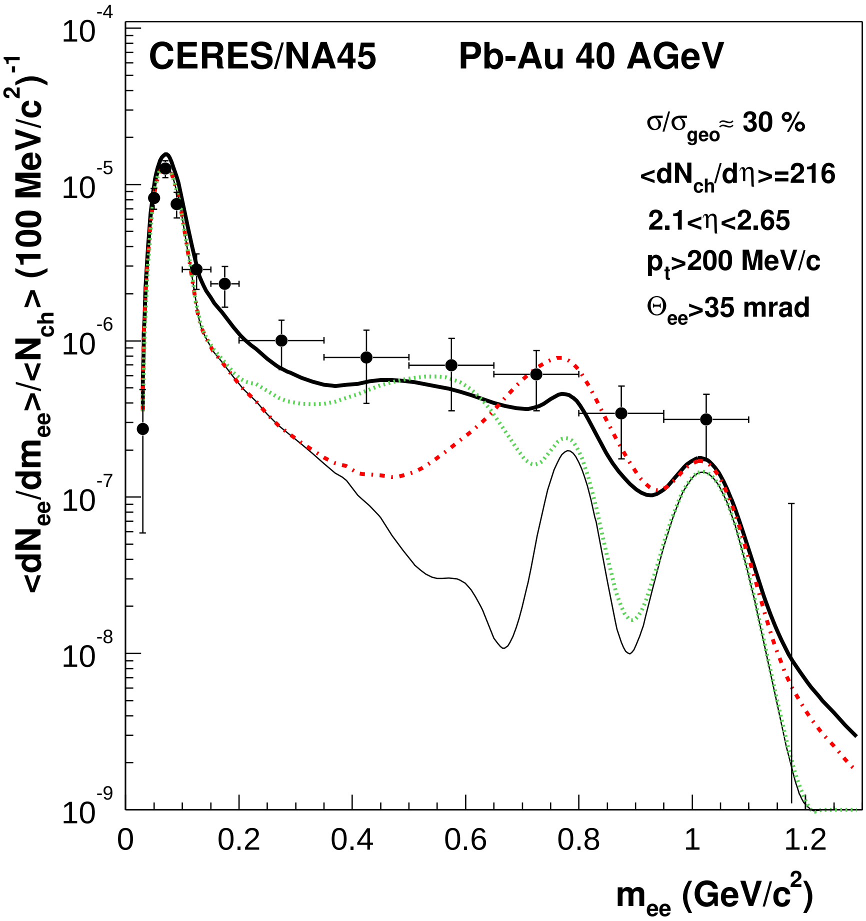


Figure 7.9: *Comparison of the 40 AGeV data to model calculations based on $\pi^+\pi^-$ annihilation with an unmodified $\rho$ (red dashed-dotted), an in-medium dropping $\rho$ mass (green dotted) and an in-medium spreaded $\rho$ (black thick solid) [86]. All three calculations contain the sum of the hadronic decay sources. This sum is taken from the CERES cocktail (Fig. 6.2 in chapter 6) and shown also separately (black thin solid line). It excludes the contribution of the $\rho$ to avoid double counting. The errors attached to the data points are purely statistical. The systematical errors are 16% for m$\leq$0.2 GeV/c$^2$ and 26% for m$>$0.2 GeV/c$^2$, quadratically small compared to the individual statistical errors.*

The theoretical results from the Rapp/Wambach approach contained in Fig. 7.8 (right panel) directly reflect the consequences of the broadened spectral function of the $\rho$: a strong enhancement of the dilepton production rate for invariant masses below 0.65 GeV/c$^2$, while the peak at 0.77 GeV/c$^2$ disappears, becoming broad and structureless (the small remaining peak is due to the $\omega$). The combined medium effects in the $\rho$ propagation lead to good agreement with the data points both in absolute yield and in spectral shape.

A comparison of the data to the three theoretical predictions for $\pi^+\pi^-$ annihilation, all computed by using the same fireball simulation with the same initial and freezeout conditions, is shown in Fig. 7.9. The data quality is sufficient to rule out an unmodified $\rho$ (vacuum-) spectral function. The spectra with medium modifications are consistent with the experimental data points, but a more detailed differentiation between the different medium scenarios is, within the present errors, hardly possible.

A careful inspection of the mass region $\leq$0.2 GeV/c$^2$ shows the sum of the Rapp/ Wambach model and the Dalitz part of the hadronic decay cocktail to be higher by nearly 30% than the data points, while the agreement with the cocktail part alone is to within 2% (see section 7.1.4). The theoretical yield in this region is dominated by bremsstrahlung and by baryon Dalitz decays. Unfortunately, the combined error of 11%(stat, data) + 16%(syst,data) + 8%(syst, cockt), i.e. a total of 21% (see again 7.1.4) does nor allow to draw any firm conclusions on this "theoretical excess" of 30%.

The dependence of the enhanced dilepton yield on the pair transverse momentum $p_t^{ee}$ has also been theoretically investigated. The measured invariant mass spectra in two different pair-$p_t^{ee}$ bins show the enhancement in the low-$p_t^{ee}$ region to be much larger than in the high-$p_t^{ee}$ region. The comparison between the data and the three theoretical predictions is shown in Fig. 7.10. Again, quantitative agreement of the

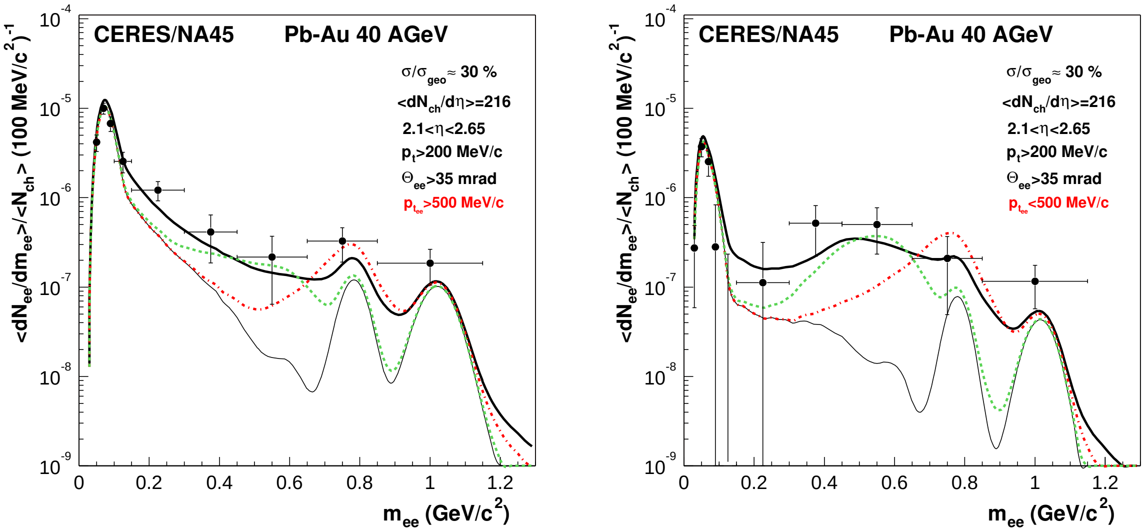


Figure 7.10: *Invariant mass spectra for two pair transverse momentum bins $p_t^{ee}$>500 MeV (left panel) and $p_t^{ee}$<500 MeV/c (right panel) in comparison to model calculations based on $\pi^+\pi^-$ annihilation with an unmodified $\rho$ (red dashed-dotted), an in-medium dropping $\rho$ mass (green dotted) and an in-medium spreaded $\rho$ (black thick solid). All three calculations contain the sum of the hadronic decay sources. This sum is taken from the CERES cocktail (Fig. 6.2 in chapter 6) and shown also separately (black thin solid line). It excludes the contribution from the $\rho$ to avoid double counting. For a discussion of the experimental errors, see subscript of Fig. 7.9.*

data with the model calculations is seen for the two in-medium scenarios, including now the distinct difference between the two pair-$p_t^{ee}$ bins, while the predictions for the vacuum spectral function are clearly off. The peculiar low-$p_t^{ee}$ enhancement has been theoretically linked to the possibility that the lepton pair yield may be associated with the total energy of a pair as $m_t^{ee} \approx ((m_\rho^*)^2 + (p_t)^2)^{1/2} = ((m_{ee})^2 + (p_t^{ee})^2)^{1/2}$ [111].

The 40 AGeV run was motivated in section 1.2.5 of the theoretical introduction to this thesis by its key role in differentiating between baryon density and temperature. With the larger baryon density and smaller temperature expected at 40 compared to 160 AGeV, the larger enhancement factor of 5 together with the good agreement between the data and the model calculations for 40 AGeV (which are dominated by baryon density effects) give strong support to the following conclusion: the enhancement of the CERES dilepton yield is due to the in-medium effects of the intermediate $\rho^*$ in $\pi^+\pi^-$ annihilation, and *the in-medium effects are basically baryon-driven.*

### Chiral symmetry and baryons

In BR-scaling, the *$\rho$-mass shift* is directly connected to chiral symmetry restoration. In the RW scenario, the connection between the baryons driving the *$\rho$-broadening* and chiral symmetry restoration is much less clear. As has been pointed out recently [117, 118], the absence of parity doublets in the low-lying hadronic spectrum may not continue at higher excitation energies. On the contrary, high-lying baryonic states, at 2 GeV or above, seem to appear in the form of close parity doublets, possibly indicating smooth chiral symmetry restoration with increasing excitation energy. This in itself is, of course, not linked to a phase transition [117]. However, as has been discussed recently by Rapp [86], the explicit consideration of *dynamical* processes may create such a link. A possible scheme is illustrated in Fig. 7.11, comparing the mesonic (left panel)

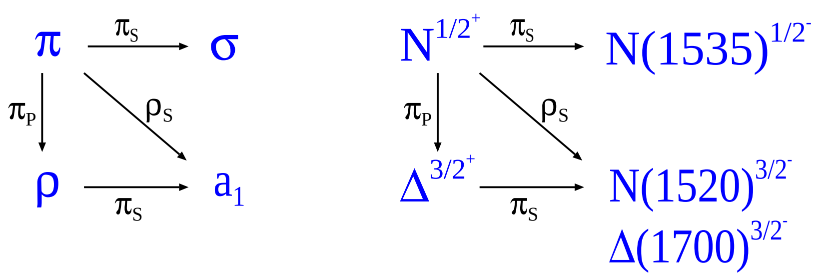


Figure 7.11: *Interaction scheme combining chiral and resonance excitations [86].*

with the baryonic (right panel) sector. Pionic s-wave excitations connect chiral partners like $\rho \rightarrow a_1$ or $\Delta^{3/2} \rightarrow N(1520)^{3/2}$, while pionic p-wave excitations create hadronic resonances like $\pi \rightarrow \rho$ or $N^{1/2} \rightarrow \Delta^{3/2}$. The s-wave resonances $N(1520)$ and $\Delta(1700)$ appearing in this scheme are indeed among the most important baryons responsible for the $\rho$-broadening (see previous subsection). It remains to be seen, whether a more quantitative scheme of this type will completely clarify the link to chiral restoration [119]. It should be added for completeness that a possible connection between BR-scaling and the RW scenario has also been discussed [111].

**QGP-phase plus in-medium effects based on VDM and chiral dynamics (Renk-Schneider-Weise)**

At SPS energies and surely at 40 AGeV, only a small space-time volume is occupied by the QGP, and the dilepton yield produced in this phase from $q\overline{q}$ annihilation, especially in the low mass region m< 1 GeV/c$^2$, is inevitably small. The evolution continues after the phase transition, and any information from the QGP phase is thus mixed with signals from the hadronic phase where the space-time volume is much larger. In the two approaches discussed previously, the small plasma contribution was originally ignored and only added recently in a very simplified pQCD calculation.

In the approach taken by Weise et al. [122], dilepton radiation from the QGP at the early stages of the collision is explicitly included. In view of the fact that all phenomena connected with the phase transition close to $T_c$ address nonperturbative QCD, their approach treats quarks and gluons as non-interacting massive thermal quasiparticles [120], with properties such as to reproduce the lattice-QCD equation-of-state. Passing through the phase transition, active partonic degrees of freedom are suppressed due to the confinement process and the creation of the hadronic phase. Direct dilepton radiation from the hot and dense hadronic phase is calculated using Vector Meson Dominance combined with Chiral Dynamics where the thermally excited particles annihilate through the time-like virtual photon which decays into a lepton-antilepton pair (see section 7.22). To calculate the differential pair rate, the photon-self energy is needed both from the early quark-gluon phase and from the longer-lived hadronic phase [121].

1) In the QGP phase, dileptons are produced from $q\overline{q}$ annihilation into virtual photons decaying into $e^+e^-$ pairs. The production mechanism actually used is the annihilation of $q\overline{q}$ pairs with thermal masses m(T) into virtual photons. The quark lines are multiplied with a distribution $C(T) \cdot f_D(T)$, describing the reduced (by C(T)) probability $f_D(T)$ of finding a quark or antiquark in the hot medium; this means changing the free particle distribution function $f_D(T) \to C(T) \cdot f_D(T)$. The thermal masses $m_q$(T) drop as $T_c$ is approached from above. Using the approximately universal function C(T), the physical EoS from lattice results is reproduced [123, 124].

2) As the phase transition proceeds due to confinement, the new effective degrees of freedom, color singlets, are formed. In the VMD model combined with chiral dynamics, the photon couples to the lowest-lying dipole excitations of the vacuum, and hadronic states with the same quantum numbers as the electromagnetic current can be connected to the currents of these mesons (see 7.2.2).

The most prominent changes of the spectral function arise also here from the broadening of the $\rho$ due to the combined effects of baryon density and temperature. By studying temperature effects (using thermal Feyman rules [122]) and baryon effects [94], this approach confirms the previous findings that the baryonic effects prevail over mesonic ones, due to the strong meson-nucleon interaction (see above). The strong broadening of the $\rho$ spectral function down to the one-pion threshold is mostly due to finite baryon density effects. To be able to compare the model results to the data, the dilepton rate has again to be integrated over the space-time of the fireball. In this approach, a different simplified fireball has been simulated, using a temperature and volume parametrization based on isentropic expansion through the quark-gluon and the hadronic phase with a realistic equation-of-state in both phases [125].

The results from the model calculations are shown in Fig. 7.12 in comparison to the 40 AGeV data. The mass region below 1 GeV/c$^2$ is mainly filled by the contribution from the hadronic phase, while the high-mass region above 2 GeV/c$^2$, not included here, is mainly populated by dileptons from the QGP phase. For very low masses, the QGP phase contributes only about 1%. The hadronic part of the calculation explicitly includes in-medium effects on the $\omega$ and the $\phi$, beyond those on the $\rho$. Due to the long

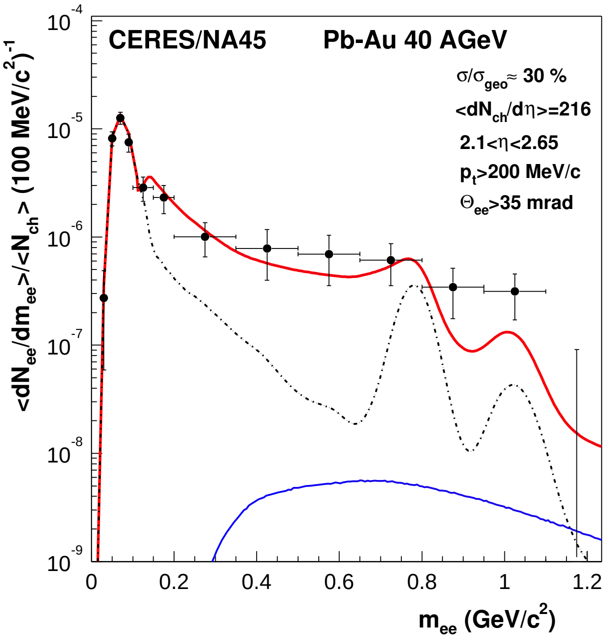


Figure 7.12: *Comparison of the 40 AGeV data to model calculations [121] (red thick solid) which include dilepton radiation both from the QGP phase (in terms of thermal quasiparticles) and from the hadronic phase (in terms of VDM combined with chiral dynamics). The calculations contain the contributions from all three vector mesons $\rho$, $\omega$ and $\phi$. The contributions from Dalitz decays are taken from the CERES cocktail (fig. 6.2 in chapter 6). They are shown separately, extending up to ~0.6 GeV/c$^2$; beyond, they smoothly link to the post-freezeout fraction of the $\omega$ and $\phi$ decays, projected out of the model calculations (black thin dashed-dotted). The QGP part is also shown separately (blue thin solid). For a discussion of the experimental errors, see subscript of Fig. 7.9.*

life time, a sizable fraction of their decays still occurs after freezeout, uninfluenced by the environment. That fraction is shown separately in Fig. 7.12 (not taken from the CERES cocktail!). For the particularly long-lived $\phi$, the vacuum fraction is surprisingly small. The total relative yield of the $\omega$ and $\phi$, visible as the two peaks in the sum of all contributions (red line), also seems to deviate somewhat from the expectations based on the CERES cocktail (comparing e.g. Fig. 7.9). Still, the overall agreement of the model calculations with the data is on a level comparable to BR-scaling and the approach taken by Rapp/Wambach.

### Quark-Hadron duality

In the vicinity of the phase transition, the dilepton radiation from the hot and dense fireball is not very sensitive to whether it is emitted from a chirally broken hadronic phase or from a chirally restored QGP phase. The calculated dilepton rates using either hadronic or quark-gluon degrees of freedom merge together: *the two descriptions become dual* [11, 126]. Duality is known from $e^+e^-$ annihilation in particle physics: the vacuum $q\overline{q}$ rates coincide with the hadronic description for invariant masses M$\geq$1.5 GeV/c$^2$ up to additional resonance structure in the vicinity of the next heavy-quark threshold (such as $c\overline{c}$). In our case of a hot and dense fireball, due to the strong medium modification of the $\rho$ in particular, both the time-averaged mass reduction and the spread of the width are sufficiently large for the whole spectrum to be described as if it were due to $q\overline{q}$ annihilation, in the spirit of hadron-parton duality. There is approximate agreement between the two rates down to the rather low mass scale of $\sim$0.5 GeV/c$^2$. In this sense, the medium effects have been interpreted as a "lowering of the quark-hadron duality threshold" [11, 126].

Using QG degrees of freedom only, the dilepton rates have been calculated from lowest order $\mathcal{O}(\alpha\alpha_S^0)$ $q\overline{q}$ annihilation, i.e. in perturbative QCD. The results [11, 126] show a rather continuous enhancement below the $\rho$, quite close to the "spreaded-$\rho$" case in Fig. 7.9 both in magnitude and in slope.

### Quark-hadron duality modeling (Kämpfer et al.)

Lowest-order $q\overline{q}$ annihilation in the spirit of parton-hadron duality has been consistently used by Kämpfer et al. for the full invariant mass range and for the full time evolution of the collision [127, 128]. Therefore, the approach is called the "extended duality" hypothesis. It should be emphasized once again that this is a *parametrization* in parton language, irrespective of the true (mostly hadronic) nature of the hot and dense medium. The Lorentz invariant dilepton rate from matter in local thermal equilibrium is characterised by temperature T, chemical potentials $\mu_i$ and four-velocity $u^\nu$ of the flow. Based on lowest order $q\overline{q}$ annihilation, the rate is expressed by a Boltzmann approximation [129] as

$$\frac{dN}{d^4xd^4Q} \sim exp(-\frac{Q\cdot u}{T}) \tag{7.22}$$

where the term related to the chemical potential is suppressed. The quantity $Q^\mu = (M_\perp coshY, M_\perp sinhY, \vec{Q_\perp})$ is the lepton-pair four-momentum, and the invariant mass is calculated as $\sqrt{M_\perp^2 - Q_\perp^2}$.) A further strong approximation which makes the model so simple is to replace all state variables by averages: $T(t,\vec{x}) \to \langle T\rangle \equiv T_{eff}$, $u(t,\vec{x}) \to \langle u\rangle$ and $\int dtd^3x \to \int dtV(t) \to N_{eff}$ . Thus, the thermal source is parametrized by a Boltzmann-like exponential function with effective temperature T$_{eff}$ and normalization factor N$_{eff}$, reflecting the space-time volume occupation of a thermal source (in the sense of the usual parametrization of transverse momentum spectra of hadrons,

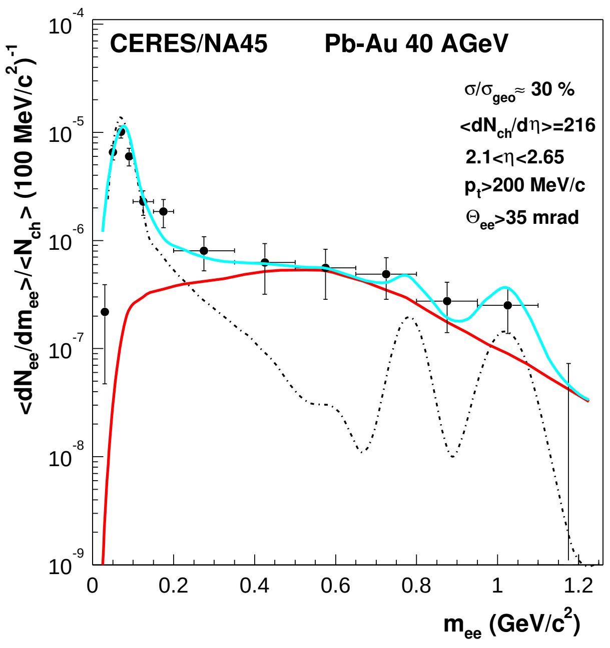


Figure 7.13: *Comparison of the 40 AGeV data to a model calculation by Kämpfer et al. [127, 128], based on extended parton-hadron duality. Separately shown are the thermal yield (red solid line), the hadronic decay contribution (thin dashed-dotted line) and the sum of the two (thick blue solid line). The hadronic decay contribution is taken from the CERES cocktail (Fig. 6.2 in chapter 6). It excludes the contribution of the $\rho$ to avoid double counting. For a discussion of the experimental errors, see subscript of Fig. 7.9.*

i.e. of exponential distributions with slope parameters and normalization factors):

$$\frac{dN}{d^4Q} \sim N_{eff} \cdot exp(-\frac{Q \cdot \langle u \rangle}{T_{eff}}) \tag{7.23}$$

The thermal dilepton rate is then integrated, including detector acceptances and other experimental cuts. Finally, other physical "background" like a hadronic decay contribution is added. The resulting thermal distributions are characterized by a minimal unique set of parameters T$_{eff}$ and N$_{eff}$. With one such unique set at a given beam energy, the CERES/NA45 $e^+e^-$ data for low pair masses <1 GeV/c$^2$, the NA50 $\mu^+\mu^-$ data for high pair masses >1 GeV/c$^2$ and the WA98 data on real photons with transverse momenta >2 GeV/c can be quantitatively described at the same time [129].

The $e^+e^-$-pair results for a beam energy of 40 AGeV are compared in Fig. 7.13 to the CERES data of this work. Once again, perfect agreement within the errors is seen between the model calculation and experiment. The effective temperature required to describe the data is $T_{eff}$≈145 MeV, significantly lower than the value of ≈170 MeV needed at 160 AGeV [129].

# Chapter 8

# Concluding remarks

The study of the critical behaviour of strongly interacting matter and the dynamics of the associated phase transitions - deconfinement, chiral, $U_A(1)$ - is the central goal of the heavy ion program. Since these questions address the difficult nonperturbative regime of QCD, experimental efforts are vital to drive further progress. This is particularly true for the region of finite baryon density, where numerical solutions of QCD using lattice techniques still meet enormous technical difficulties. The experimental results reported in this thesis have to be considered in that context. The emission of dileptons directly probes the fireball evolution in the early stage, when both temperature and baryon density are high. Through the dependence on the in-medium spectral function of the vector mesons (the $\rho$ in particular), the yield and the shape of the dilepton spectrum are sensitive to one of the central issues of the field, chiral symmetry restoration.

The main experimental result for Pb+Au collisions at 40 AGeV reported in this thesis is an enhancement of the dilepton yield compared to the expectation from hadronic decay sources by about a factor of 5 in the invariant mass region >0.2 GeV/c$^2$, much larger than what has been observed before at 160 AGeV. The enhancement is mostly localized at low pair-transverse-momenta of <0.5 GeV/c, just as at the higher energy. As shown in the very detailed discussions in section 7.2, both results are quantitatively described by theoretical model calculations. General agreement exists on that the excess dilepton yield beyond hadronic decays is due to direct radiation from the fireball, dominated by pion annihilation $\pi^+\pi^- \rightarrow \rho^* \rightarrow e^+e^-$. However, both the amount of the excess yield and its specific spectral shape require the intermediate $\rho^*$ appearing in the annihilation graph to be substantially modified in the hot and dense environment, compared to its vacuum properties. The theoretical models differ largely in the way, in which these modifications are treated. In the basically partonic language of Brown/Rho scaling, the *mass of the* $\rho^*$ decreases at high temperatures and baryon densities as a direct consequence of chiral symmetry restoration. In the basically hadronic language of Rapp/Wambach, the *width of the* $\rho^*$ increases, mostly due to high baryon density rather than to high temperature, while its mass remains roughly constant. The connection to chiral symmetry restoration also exists there, but it is at present not worked out in quantitative detail. The dominant role of baryon density in the theoretical treatment (which may, somewhat hidden, also exist in the Brown/Rho approach) finds its support in the beam-energy dependence of the observed dilepton yield: the larger enhancement found at 40 compared to 160 AGeV together with the good agreement between theory and experiment is consistent with the larger baryon density and smaller temperature expected at 40 AGeV. This is, besides the sole existence of a dilepton excess also at the lower beam energy, *the crucial new physics result* of this thesis.

Unfortunately, the data quality is limited, due to the problems of the TPC and its readout during the 1999 data taking period. With only 185$\pm$48 net pairs in the high-mass sample $>$0.2 GeV/$c^2$, the error bars on the spectral shape do not allow to distinguish in detail between the different theoretical scenarios, and even the global value of the enhancement is only established to within 4 standard deviations. Beyond the high-statistics data taken by CERES in the year 2000, where the full power of the new TPC including its improved mass resolution of $\leq$2% should materialize, a further run with a comparably high statistics at a lower beam energy seems mandatory. Such a run at 20 and 30 AGeV is under consideration for late 2002, but as of the time of this write-up not yet approved. If approval would not be given, the issue may never be clarified cleanly. A new project at GSI could, of course, enter here.

# Bibliography


[1] J.F. Donoghue, E. Golowich, and B.R. Holstein, "Dynamics of the Standard Model," Cambridge University Press, Cambridge, 1992

[2] F. Karsch, "Lattice results on QCD thermodynamics," Nucl. Phys. A **698** (2002) 199, hep-ph/0103314.

[3] H. Satz, "Colour deconfinement in nuclear collisions," Rept. Prog. Phys. **63** (2000) 1511, hep-ph/0007069.

[4] R. D. Pisarski, "Quark-gluon plasma as a condensate of SU(3) Wilson lines," Phys. Rev. D **62** (2000) 111501, hep-ph/0006205.

[5] F. Karsch, "Lattice QCD at high temperature and density," hep-lat/0106019.

[6] A. V. Smilga, "Physics of thermal QCD," Phys. Rept. **291** (1997) 1, hep-ph/9612347.

[7] W. Weise, "Hadrons in Dense Baryonic Matter," Nucl. Phys. A **610** (1996) 35C.

[8] F. Karsch, "Lattice QCD at Finite Temperature," Lectures on "QCD Perspectives on hot and Dense Matter", given at NATO Advanced Study Institute, Cargese, 2001

[9] F. Karsch, E. Laermann, P. Petreczky, S. Stickan and I. Wetzorke, "A lattice calculation of thermal dilepton rates," Phys. Lett. B **530** (2002) 147, hep-lat/0110208.

[10] F. Zantow, O. Kaczmarek, F. Karsch and P. Petreczky, "Short distance physics with heavy quark potentials," Nucl. Phys. Proc. Suppl. **106**, 519 (2002),hep-lat/0110103.

[11] R. Rapp and J. Wambach, "Chiral symmetry restoration and dileptons in relativistic heavy-ion collisions," Adv. Nucl. Phys. **25** (2000) 1, hep-ph/9909229

[12] R. D. Pisarski, "Phenomenology of the Chiral Phase Transition," Phys. Lett. B **110** (1982) 155.

[13] E. V. Shuryak, "Quark - Gluon Plasma and Hadronic Production of Leptons, Photons and Psions," Phys. Lett. B **78** (1978) 150 [Sov. J. Nucl. Phys. **28** (1978 YAFIA,28,796-808.1978) 408.1978 YAFIA,28,796].

[14] G. Agakishiev *et al.* [CERES/NA45 Collaboration], "Neutral Meson Production in p-Be and p-Au Collisions at 450 GeV Beam Energy," Eur. Phys. J. C **4** (1998) 249.

[15] G. Agakishiev *et al.* [CERES/NA45 Collaboration], "Systematic Study of Low-Mass Electron Pair Production in p-Be and p-Au Collisions at 450 GeV," Eur. Phys. J. C **4**, 231 (1998).

[16] G. Agakishiev *et al.* [CERES/NA45 Collaboration], "Enhanced production of low mass electron pairs in 200 GeV/u S-Au collisions at the CERN SPS," Phys. Rev. Lett. **75** (1995) 1272.

[17] T. Ullrich, "Produktion von $e^+e^-$ -Paaren in ultrarelativistischen S-Au-Kollisionen bei 200 GeV/u," PhD thesis, Ruprecht-Karls-Universität Heidelberg, 1994

[18] G. Agakishiev *et al.* [CERES/NA45 Collaboration], "Low-mass $e^+e^-$ pair production in 158 A GeV Pb-Au collisions at the CERN SPS, its dependence on multiplicity and transverse momentum," Phys. Lett. B **422**, 405 (1998), nucl-ex/9712008.

[19] C. Voigt, "Produktion von $e^+e^-$ - Paaren in ultrarelativisischen Pb-Au Kollisionen bei 160 A GeV," PhD thesis, Ruprecht-Karls-Universität Heidelberg, 1998.

[20] G. Agakishiev *et al.* [CERES/NA45 Collaboration], "CERES Results on Low-Mass Electron Pair Production in Pb-Au Collisions," Nucl. Phys. A **638** (1998) 159.

[21] B. Lenkeit, "Electon-Positron-Paar Emission in Pb-Au Kollisionen bei 158 A GeV," PhD thesis, Ruprecht-Karls-Universität Heidelberg, 1998.

[22] B. Lenkeit *et al.* [CERES/NA45 Collaboration], "Recent results from Pb-Au collisions at 158 GeV/c per nucleon obtained with the CERES spectrometer," Nucl. Phys. A **661** (1999) 23, nucl-ex/9910015

[23] G. Agakishiev *et al.* [CERES/NA45 Collaboration], "$e^+e^-$-pair production in Pb-Au collisions at 158 GeV per nucleon," in preparation (2002) .

[24] P. Braun-Munzinger *et al.*, "Dynamics of ultra-relativistic nuclear collisions with heavy beams: An experimental overview," Nucl. Phys. A **638** (1998) 3, nucl-ex/9803015.

[25] P. Braun-Munzinger, I. Heppe and J. Stachel, "Chemical equilibration in Pb + Pb collisions at the SPS," Phys. Lett. B **465** (1999) 15, nucl-th/9903010.

[26] E. V. Shuryak, "Correlation Functions in the QCD Vacuum," Rev. Mod. Phys. **65** (1993) 1.

[27] V. Koch, M. Bleicher, A. K. Dutt-Mazumder, C. Gale and C. M. Ko, "Dilepton production and chiral symmetry," nucl-th/0002044.

[28] R. Rapp and J. Wambach, "Low mass dileptons at the CERN-SPS: Evidence for chiral restoration?," Eur. Phys. J. A **6**, 415 (1999), hep-ph/9907502.

[29] G. E. Brown and M. Rho, "Chiral restoration in hot and/or dense matter," Phys. Rept. **269**, 333 (1996), hep-ph/9504250.

[30] G. Q. Li, C. M. Ko, G. E. Brown and H. Sorge, "Dilepton production in proton nucleus and nucleus nucleus collisions at SPS energies," Nucl. Phys. A **611** (1996) 539, nucl-th/9611037.

[31] G. Q. Li, C. M. Ko and G. E. Brown, "Enhancement of low mass dileptons in heavy ion collisions," Phys. Rev. Lett. **75** (1995) 4007, nucl-th/9504025.

[32] R. Rapp, G. Chanfray and J. Wambach, "Rho meson propagation and dilepton enhancement in hot hadronic matter," Nucl. Phys. A **617** (1997) 472, hep-ph/9702210.

[33] M. Lutz, S. Klimt and W. Weise, "Meson Properties at Finite Temperature and Baryon Density," Nucl. Phys. A **542** (1992) 521.

[34] Y. Nambu and G. Jona-Lasinio, "Dynamical Model of Elementary Particles Based on an Analogy with Superconductivity. I," Phys. Rev. **122** (1961) 345.

[35] G. Agakishiev *et al.* [CERES/NA45 Collaboration], "Performance of the CERES Electron Spectrometer in the CERN SPS Lead Beam," Nucl. Instrum. Meth. A **371** (1996) 16.

[36] G. Agakishiev *et al.* [CERES/NA45 Collaboration], "First Results from the CERES Radial TPC," Nucl. Phys. A **661** (1999) 673.

[37] D. Miskowiec, "Trigger control software for CERES/NA45," GSI Annual Report, 1999

[38] D. Miskowiec, Darmstadt, private communication, 2002

[39] W. Schmitz, "Lambda-Produktion in Pb-Au-Kollisionen bei 40 A GeV," PhD thesis, Ruprecht-Karls-Universität Heidelberg, 2001

[40] J. Slivova, "Azimuthal Correlations of High-$p_t$ Pions in 158 AGeV/c Pb-Au Collisions from the CERES/NA45 Experiment", PhD thesis, Charles University, Prague, in preparation

[41] J. Slivova, Heidelberg, private communication, 2000

[42] V. Petracek, Heidelberg, private communication, 2001

[43] G. Agakishiev *et al.*, "A new robust fitting algorithm for vertex reconstruction in the CERES experiment," Nucl. Instrum. Meth. A **394** (1997) 225.

[44] H. Appelshäuser, Heidelberg, private comunication, 2000

[45] S. V. Afanasiev *et al.* [The NA49 Collaboration], "Energy dependence of pion and kaon production in central Pb + Pb collisions," nucl-ex/0205002

[46] V. Friese [NA49 Collaboration], "New results from NA49," hep-ph/0111423, and private communication with NA49, 2001

[47] A. Cherlin, Rehovot, private communication, 2000

[48] S. Iourevich, Heidelberg, private communication, 2000

[49] B. Lenkeit, "Produktion von geladenen Pionen mit hohem Transversalimpuls in 200 GeV/u S+Au Kollisionen", Diploma thesis, Ruprecht-Karls-Universität Heidelberg, 1995

[50] G. Agakishiev *et al.*, "Cerenkov Ring Fitting Techniques for the CERES RICH Detectors," Nucl. Instrum. Meth. A **371** (1996) 243.

[51] A. Marín, "Design and performance of the CERES-TPC gas system," Internal Note, CERES collaboration, 2001

[52] A. Marín, "Electric field correction from lead data," Internal Note, CERES collaboration, 2000

[53] G. Agakishiev, "Technical Note on the NA45/CERES Upgrade", Report to the CERN SPSLC 96-50/R110 (1996)

[54] S.I. Esumi, Heidelberg, private comunication, 1999

[55] C. Roland, "Flavor Fluctuations in central Pb+Pb Collisions at 158 GeV/Nucleon", PhD thesis, Frankfurt am Main 1999

[56] G. Hering, "Dielectron production in heavy-ion collisions at 158 GeV/c per nucleon," PhD thesis, Technische Universität Darmstadt, 2001

[57] R. Brun, CERN DD/EE/84-1.

[58] W.W.M. Allison and J.H.Cobb, Ann. Rev. Nucl. Part. Sci. 30 (1980) 253

[59] T. Wienold, Heidelberg, private communication, 1999

[60] K. Filimonov, Heidelberg, private communication, 2000

[61] K. Filimonov, "CERES TPC Simulation," Internal Note, CERES collaboration, 2000

[62] G. Agakishiev, Heidelberg, private communication, 2000

[63] T. Ullrich and D. Irmscher, "The code GENESIS", Internal Note, CERES collaboration

[64] H. Sako, "Development of New GENESIS," Technical Report 03-24, CERES collaboration, 2000; http://www.gsi.de/sako.

[65] D. H. Rischke, "Remarks on the extraction of freeze-out parameters," Nucl. Phys. A **698** (2002) 153, nucl-th/0104071.

[66] T. Csorgo and B. Lorstad, "Bose-Einstein Correlations for Three-Dimensionally Expanding, Cylindrically Symmetric, Finite Systems," Phys. Rev. C **54** (1996) 1390, hep-ph/9509213.

[67] R. Scheibl and U. W. Heinz, "Coalescence and flow in ultra-relativistic heavy ion collisions," Phys. Rev. C **59** (1999) 1585, nucl-th/9809092.

[68] J. Schaffner-Bielich, D. Kharzeev, L. D. McLerran and R. Venugopalan, "Generalized scaling of the transverse mass spectrum at the Relativistic Heavy-Ion Collider," nucl-th/0108048.

[69] H. Sako, Darmstadt, private communication, 2001

[70] N. M. Kroll and W. Wada, "Internal Pair Production Associated with the Emission of High-Energy Gamma Rays," Phys. Rev. **98** (1955) 1355.

[71] R. I. Dzhelyadin *et al.*, "Investigation of $\eta$ meson electromagnetic structure in $\eta \to \mu^+\mu^-\gamma$ decay" Phys. Lett. B **94** (1980) 548

[72] L. G. Landsberg, "Electromagnetic Decays of Light Mesons," Phys. Rept. **128** (1985) 301.

[73] E. V. Shuryak, "What have we learned and want to learn from heavy ion collisions at CERN SPS?," Nucl. Phys. A **661** (1999) 119, hep-ph/9906443].

[74] K. Kajantie, J. Kapusta, L. D. McLerran and A. Mekjian, "Dilepton Emission and the QCD Phase Transition in Ultrarelativistic Nuclear Collisions," Phys. Rev. D **34** (1986) 2746.

[75] V. Cerny, P. Lichard and J. Pisut, "A Clear Cut Test of Low Mass Dilepton Production Mechanism in Hadronic Collisions," Z. Phys. C **31** (1986) 163.

[76] T. Akesson *et al.* [AXIAL FIELD SPECTROMETER COLLABORATION], "The Production of Prompt Positrons at Low Transverse Momentum Increases with the Square of yhe Associated Charged Multiplicity," Phys. Lett. B **192** (1987) 463.

[77] H. Sorge, H. Stocker and W. Greiner, "Poincare Invariant Hamiltonian Dynamics: Modeling Multi - Hadronic Interactions In A Phase Space Approach," Annals Phys. **192** (1989) 266.

[78] S. A. Bass *et al.*, "Microscopic models for ultrarelativistic heavy ion collisions," Prog. Part. Nucl. Phys. **41** (1998) 225, nucl-th/9803035.

[79] M. Bleicher *et al.*, "Relativistic hadron hadron collisions in the ultra-relativistic quantum molecular dynamics model," J. Phys. G **25**, 1859 (1999), hep-ph/9909407.

[80] P. Huovinen, M. Belkacem, P. J. Ellis and J. I. Kapusta, "Dileptons and photons from coarse-grained microscopic dynamics and hydrodynamics compared to experimental data,", nucl-th/0203023.

[81] W. Ehehalt and W. Cassing, "Relativistic Transport Approach for Nucleus Nucleus Collisions from SIS to SPS Energies," Nucl. Phys. A **602** (1996) 449.

[82] J. Sollfrank, P. Huovinen, M. Kataja, P. V. Ruuskanen, M. Prakash and R. Venugopalan, "Hydrodynamical description of 200 A GeV S+Au collisions: Hadron and electromagnetic spectra," Phys. Rev. C **55** (1997) 392, nucl-th/9607029.

[83] H. Von Gersdorff, L. D. McLerran, M. Kataja and P. V. Ruuskanen, "Studies of the Hydrodynamic Evolution of Matter Produced in Fluctuations in $\overline{p} - p$ Collisions and in Ultrarelativistic Nuclear Collisions," Phys. Rev. D **34**, 794 (1986).

[84] C. M. Hung and E. V. Shuryak, "Hydrodynamics near the QCD phase transition: Looking for the longest lived fireball," Phys. Rev. Lett. **75** (1995) 4003, hep-ph/9412360.

[85] U. Mayer, E. Schnedermann and U. W. Heinz, "Transverse radii from pion interferometry for an expanding fireball," Phys. Lett. B **294** (1992) 69.

[86] R. Rapp, "Dileptons in high-energy heavy-ion collisions," hep-ph/0201101.

[87] G. E. Brown and M. Rho, "Scaling Effective Lagrangians in a Dense Medium," Phys. Rev. Lett. **66** (1991) 2720.

[88] W. Cassing, W. Ehehalt and C. M. Ko, "Dilepton production at SPS energies," Phys. Lett. B **363** (1995) 35, hep-ph/9508233.

[89] J. V. Steele, H. Yamagishi and I. Zahed, "Dilepton and Photon Emission Rates from a Hadronic Gas," Phys. Lett. B **384** (1996) 255, hep-ph/9603290.

[90] J. V. Steele, H. Yamagishi and I. Zahed, "Dilepton and photon emission rates from a hadronic gas. II," Phys. Rev. D **56** (1997) 5605, hep-ph/9704414.

[91] V. Koch and C. Song, "Dilepton production at SPS-energy heavy ion collisions," Phys. Rev. C **54** (1996) 1903, nucl-th/9606028.

[92] R. Rapp, G. Chanfray and J. Wambach, "Medium modifications of the rho meson at CERN SPS energies," Phys. Rev. Lett. **76** (1996) 368, hep-ph/9508353.

[93] B. Friman and H. J. Pirner, "P-wave polarization of the rho meson and the dilepton spectrum in dense matter," Nucl. Phys. A **617** (1997) 496, nucl-th/9701016.

[94] F. Klingl, N. Kaiser and W. Weise, "Current correlation functions, QCD sum rules and vector mesons in baryonic matter," Nucl. Phys. A **624** (1997) 527, arXiv:hep-ph/9704398.

[95] M. Le Bellac, "Thermal Field Theory," Cambridge University Press, Cambridge, 1996

[96] R.A. Schneider, "Thermal field theory and dilepton production in heavy-ion collisions," Diploma thesis, Technische Universität München, 2000

[97] M. Herrmann, B. L. Friman and W. Norenberg, "Properties of rho mesons in nuclear matter," Nucl. Phys. A **560** (1993) 411.

[98] A. L Fetter and J. D Walecka, "Quantum Theory of many-particle systems," (McCrraw-Hill, NewYork, 1971)

[99] M. E. Peskin, D. V. Schroeder, "Quantum Field Theory" (Addison-Wesly, 1995)

[100] G. E. Brown and M. Rho, "Chiral Restoration in Hot Matter," Nucl. Phys. A **590** (1995) 527C.

[101] C. M. Ko, V. Koch and G. Q. Li, "Properties of hadrons in the nuclear medium," Ann. Rev. Nucl. Part. Sci. **47** (1997) 505, nucl-th/9702016.

[102] T. Schafer and E. V. Shuryak, "The instanton liquid in QCD at zero and finite temperature," Phys. Rev. D **53** (1996) 6522, hep-ph/9509337.

[103] C. M. Ko, G. Q. Li, G. E. Brown and H. Sorge, "Enhancement of low-mass dileptons in SPS heavy-ion collisions: Possible evidence for dropping rho meson mass in medium," Nucl. Phys. A **610**, 342C (1996), nucl-th/9609008.

[104] G. E. Brown and M. Rho, "On the manifestation of chiral symmetry in nuclei and dense nuclear matter," Phys. Rept. **363** (2002) 85, hep-ph/0103102.

[105] F. Karsch, "The Phase transition to the quark gluon plasma: Recent results from lattice calculations," Nucl. Phys. A **590** (1995) 367C, hep-lat/9503010.

[106] E. Laermann, "Recent Results from Lattice QCD Simulations," Nucl. Phys. A **610** (1996) 1C.

[107] C. Adami and G. E. Brown, "Order of the QCD Transition and QCD Sum Rules," Phys.Rev. D **46** (1992) 478.

[108] T. Hatsuda, "Theoretical overview: Hot and dense QCD in equilibrium," Nucl. Phys. A **544** (1992) 27.

[109] X. m. Jin and D. B. Leinweber, "Valid QCD sum rules for vector mesons in nuclear matter," Phys. Rev. C **52**, 3344 (1995), nucl-th/9510064.

[110] M. Rho, Y. Kim, R. Rapp and G. E. Brown, "A schematic model for density dependent vector meson masses," nucl-th/9902009

[111] G. E. Brown, G. Q. Li, R. Rapp, M. Rho and J. Wambach, "Medium dependence of the vector-meson mass: Dynamical and/or Brown-Rho scaling?," Acta Phys. Polon. B **29** (1998) 2309, nucl-th/9806026.

[112] J. Wambach and R. Rapp, "Theoretical interpretations of low-mass dileptons," Nucl. Phys. A **638** (1998) 171C, nucl-th/9802001.

[113] M. Urban, M. Buballa and J. Wambach, “Modifications of the rho meson from the virtual pion cloud in hot and dense matter,” Nucl. Phys. A **673** (2000) 357, nucl-th/9910004.

[114] R. Rapp and C. Gale, “Rho properties in a hot meson gas,” Phys. Rev. C **60** (1999) 024903, hep-ph/9902268.

[115] L. Xiong, E. V. Shuryak and G. E. Brown, “Photon production through a1 resonance in high-energy heavy ion collisions,” Phys. Rev. D **46** (1992) 3798, hep-ph/9208206.

[116] M. Urban, M. Buballa, R. Rapp and J. Wambach, “Momentum dependence of the pion cloud for rho mesons in nuclear matter,” Nucl. Phys. A **641**, 433 (1998), nucl-th/9806030.

[117] T. D. Cohen and L. Y. Glozman, “Does one observe chiral symmetry restoration in baryon spectrum?,” Int. J. Mod. Phys. A **17** (2002) 1327, hep-ph/0201242.

[118] L. Y. Glozman and D. O. Riska, “The spectrum of the nucleons and the strange hyperons and chiral dynamics,” Phys. Rept. **268** (1996) 263, hep-ph/9505422

[119] R. Rapp, in preparation (2002)

[120] R. A. Schneider and W. Weise, “On the quasiparticle description of lattice QCD thermodynamics,” Phys. Rev. C **64** (2001) 055201, hep-ph/0105242.

[121] R. A. Schneider, T. Renk and W. Weise, “Model for dilepton rates from a fireball,” Nucl. Phys. A **698** (2002) 428, hep-ph/0105243.

[122] R. A. Schneider and W. Weise, “Thermal dileptons from quark and hadron phases of an expanding fireball,” Eur. Phys. J. A **9** (2000) 357, hep-ph/0008083.

[123] F. Karsch, E. Laermann and A. Peikert, “Quark mass and flavor dependence of the QCD phase transition,” Nucl. Phys. B **605** (2001) 579, hep-lat/0012023.

[124] F. Karsch, E. Laermann and A. Peikert, “The pressure in 2, 2+1 and 3 flavour QCD,” Phys. Lett. B **478** (2000) 447, hep-lat/0002003.

[125] T. Renk, R. A. Schneider and W. Weise, “QCD thermodynamics and fireball evolution in URHICs,”,hep-ph/0202079.

[126] R. Rapp, “Duality and chiral restoration from low-mass dileptons at the CERN SPS,” Nucl. Phys. A **661** (1999) 33, hep-ph/9907342.

[127] K. Gallmeister, B. Kampfer and O. P. Pavlenko, “Is there a unique thermal source of dileptons in Pb(158 A GeV)+Au, Pb reactions?,” Phys. Lett. B **473** (2000) 20, hep-ph/9908269.

[128] B. Kampfer, O. P. Pavlenko, A. Peshier and G. Soff, “Dilepton Production in a Chemically Equilibrating, Expanding, and Hadronizing Quark - Gluon Plasma,” Phys. Rev. C **52** (1995) 2704.

[129] B. Kampfer, K. Gallmeister, O. P. Pavlenko and C. Gale, "Dileptons and photons from central heavy-ion collisions at CERN-SPS," Nucl. Phys. A **698** (2002) 424, hep-ph/0102192.

# Acknowledgements

My deepest thanks go to Prof. Hans J. Specht for his constant support and professional guidance in supervising this work. I could not have appreciated more his continous encouragement and moral-boosting throughout the work, never giving up, never showing even doubts (different from many others), always arguing “it still can be, and it will be better”. There can hardly be happier or more confident students, undergraduate or graduate, than those in his care. I greatly benefitted also from his detailed comments on the draft version of this thesis, and in particular from the considerable time and effort spent to bring my English up to standards.

Next, I wish to thank Prof. Dirk Schwalm for his willingness to be the co-referee.

I also wish to thank Prof. Johanna Stachel for inviting me to work in CERES, and for reinviting me even after I had returned home instantly.

Great thanks I owe to Kirill Filimonov for his excellent computer support in a decisive phase of this work. More than that, he continuously encouraged me in my permanent fight with software and computers, bringing down my barriers against them, always arguing “try again, try again.”

Further thanks go to Ana Marín for many useful discussions and for her helpful comments on a preliminary draft of this work.

Numerous other members of the CERES collaboration have contributed in many ways: Peter Glässel, Hannes Wessels, Harald Appelshäuser, Hejdar Agakichiev, ShinIchi Esumi, Thomas Wienold, Sergei Iourevich, Hiroyuki Sako, Heinz Tilsner and others. Without their contributions, this thesis would not have been possible. Thanks to all of them.

My interest in the theoretical relevance of the work was greatly helped by numerous discussions with Torsten Renk and Roland Schneider on some beautiful beach. I am grateful for that, and I also wish to thank them and, in particular, Ralf Rapp for sending me always their newest results and allowing me to use them at will, even before publication.

Finally, from my deepest heart, I wish to thank my wonderful parents, my sister, my brother and my little nephew Peter for love, home, understanding, patience, and for all the other really important things in life.

# The CERES Collaboration

P. Rehak
Brookhaven National Laboratory, Upton, USA

B. Lenkeit, A. Pfeiffer, J. Schukraft
CERN, Geneva, Switzerland

G. Agakichiev, P. Braun-Munzinger, C. Garabatos, G. Hering, J. Holeczek, A. Maas,
A. Marin, D. Miskowiec, J. Rak, H. Sako, S. Sedykh
GSI, Darmstadt, Germany

V. Belaga, K. Fomenko, Y. Panebrattsev, O. Petchenova, S. Shimansky, V. Yurevich
JINR, Dubna, Russia

J. P. Wurm
Max-Planck-Institut für Kernphysik, Heidelberg, Germany

H. Appelshäuser, S. Damjanovic, T. Dietel, L. Dietrich, S. I. Esumi, K. Filimonov,
P. Glässel, W. Ludolphs, J. Milosevic, V. Petracek, M. Richter, W. Schmitz, W. Seipp,
J. Slivova, H. J. Specht, J. Stachel, H. Tilsner, J. P. Wessels, T. Wienold,
B. Windelband, S. Yurevich
Universität Heidelberg, Germany

D. Adamova, V. Kushpil, M. Sumbera
NPI/ASCR, Rez, Czech Republic

A. Drees, F. Ceretto
Department for Physics and Astronomy, SUNY Stony Brook, USA

A. Cherlin, Z. Fraenkel, A. Gnaenski, A. Milov, I. Ravinovich, I. Tserruya, W. Xie
Weizmann Institute, Rehovot, Israel